

**UNIVERSIDADE FEDERAL DE SÃO CARLOS**  
**CENRO DE CIÊNCIAS EXATAS E DE TECNOLOGIA**  
**DEPARTAMENTO DE QUÍMICA**  
**PROGRAMA DE PÓS-GRADUAÇÃO EM QUÍMICA**

**MODULATION OF SEMICONDUCTORS WITH  
TRANSITION METALS: MORPHOLOGICAL,  
OPTICAL, AND ELECTRONIC PROPERTIES**

Katiana Lima do Patrocinio\*

Tese apresentada como parte dos  
requisitos para obtenção do título de  
DOUTORA EM CIÊNCIAS, área de  
concentração: QUÍMICA  
INORGÂNICA

Orientador: Elson Longo

\*bolsista CAPES

São Carlos - SP

2024



**UNIVERSIDADE FEDERAL DE SÃO CARLOS**

Centro de Ciências Exatas e de Tecnologia  
Programa de Pós-Graduação em Química

---

**Folha de Aprovação**

---

Defesa de Tese de Doutorado da candidata Katiana Lima do Patrocinio, realizada em 25/06/2024.

**Comissão Julgadora:**

Prof. Dr. Elson Longo da Silva (UFSCar)

Profa. Dra. Yara Galvão Gobato (UFSCar)

Prof. Dr. Ivo Mateus Pinatti (UFMA)

Prof. Dr. Mauricio Roberto Bomio Delmonte (UFRN)

Profa. Dra. Greici Gubert (UFSCar)

O Relatório de Defesa assinado pelos membros da Comissão Julgadora encontra-se arquivado junto ao Programa de Pós-Graduação em Química.

Faustino do Patrocínio

*In memoriam*

## AGRADECIMENTOS

A minha família, mesmo distante, sempre me apoiou nesta jornada que tracei para mim. Em particular, quero agradecer à minha mãe, Luzia, e aos meus irmãos, Ulisses, Kassandra e Uriebert, bem como honrar a memória do meu falecido pai, Faustino. Tenho certeza de que todos estão orgulhosos do quanto avancei, especialmente ele, que talvez não imaginasse que eu chegaria tão longe.

Ao Prof. Dr. Elson Longo por me receber em seu laboratório e orientar os meus primeiros passos como cientista. Ele sempre enfatizou que todo resultado, mesmo que não fosse o esperado, é significativo.

Ao pós-doc Marcelo de Assis, por sempre me ajudar e incentivar a acreditar que eu iria conseguir, além de orientar-me nas sínteses dos materiais e na correção da escrita, o que foi de extrema importância para a pesquisa e para o meu amadurecimento acadêmico.

Ao Prof. Dr. Juan Andrés, por supervisionar o estudo teórico dos materiais e por suas contribuições com correções, que foram extremamente significativas para esta pesquisa. A pós-doc Amanda e ao doutorando Jeziel, por suas valiosas contribuições ao estudo teórico. À Profa. Dra. Rosa Luser, por ceder o laboratório e os equipamentos para testar aplicação de um dos materiais.

Aos demais colaboradores: Prof. Dr. Miguel Adolfo Ponce, Prof. Dr. Marcio Daldin Teodoro, Profa. Dra. Maria Sandra Churio, pós-doc Ignacio Granone, Profa. Lúcia H. Mascaro e Profa. Maria I. B. Bernardi, por todas as contribuições significativas para esta pesquisa.

Aos meus colegas de laboratório, Laura, Kibe, Nayara, Lara, Giovanna e Mayra, por estarem sempre disponíveis para discussões

científicas, esclarecimento de dúvidas, auxílio em experimentos, e também para um café e boas risadas, mesmo em momentos de desespero.

Agradeço aos meus amigos, Priscila, Naiane, Caio, Gleison, Yara e Getúlio por tornarem esta jornada mais leve, apoiando-me e incentivando-me a não desistir. Saibam que vocês foram essenciais nessa caminhada. Sem vocês, teria sido muito mais difícil.

Agradecemos à Fundação de Amparo à Pesquisa do Estado de São Paulo – FAPESP (FAPESP CEPID-código de financiamento 2013/07296-2, 2021/06128-5) pelo seu generoso apoio.

Um agradecimento especial à Financiadora de Estudos e Projetos – FINEP, ao Conselho Nacional de Desenvolvimento Científico e Tecnológico – CNPq e à Coordenação de Aperfeiçoamento de Pessoal de Nível Superior – CAPES (código de financiamento 001) pelas suas inestimáveis contribuições.

Expressamos nossa apreciação à *Universitat Jaume I* (código de financiamento UJI-B2019-30) e à *Generalitat Valenciana* (código de financiamento CIAICO2021/122) pelo seu suporte financeiro.

Agradecemos também ao *Consejo Nacional de Investigaciones Científicas y Técnicas* (Argentina) pelas suas contribuições financeiras através de PUE 22920200100016CO-IFIMAR.

## LIST OF TABLES

<b>Table 1</b> - Comparison of the amount in mol of V (%) added to the nominal and real a AW crystal lattice.....	23
<b>Table 2</b> - Lattice parameters and unit cell volumes obtained by Rietveld refinement for the samples. ....	25
<b>Table 3</b> - Comparison between experimental and active theoretical Raman modes of this study and the literature. ....	29
<b>Table 4</b> - Comparison between the values of Surface energy ( $E_{\text{surf}}$ , eV), contribution of surface area by total area ( $C_i$ , %) and Polyhedron energy ( $E_{\text{polyhedron}}$ , eV) for each AW and AWV morphology.....	42
<b>Table 5</b> - Structural results obtained from Rietveld refinements and theoretical simulations.....	55
<b>Table 6</b> - Structural results obtained from Rietveld refinements.....	56
<b>Table 7</b> - Comparison between the theoretical lattice parameters obtained in this work with previous data reported in the literature. ....	57
<b>Table 8</b> - Bond lengths and angles at $[\text{ZnO}_4]$ , $[\text{GeO}_4]$ , and $[\text{NiO}_4]$ clusters in the ZGO and Ni-ZGO models.....	57
<b>Table 9</b> - Comparison between the experimental and theoretical Raman modes obtained in this work with previous reported experimental values. ....	59
<b>Table 10</b> - Calculated Mulliken charges of Zn, O, Ge, and Ni atoms and $[\text{ZnO}_4]$ neighbor, $[\text{GeO}_4]$ neighbor, $[\text{ZnO}_4]$ that was replaced by $\text{Ni}^{2+}$ cation, and $[\text{NiO}_4]$ clusters. ....	71
<b>Table 11</b> - The samples' colorimetric parameters ( $L^*$ , $a^*$ , $b^*$ , color).....	75
<b>Table 12</b> - Colorimetric parameters ( $L^*$ , $a^*$ , $b^*$ , color) of the samples (2, 4 e 8 % Ni) untreated and thermally treated. ....	77

## LIST OF FIGURES

<b>Figure 1</b> - (a) XRD patterns of the AW samples; (b) inset view of the main peak (231).....	22
<b>Figure 2</b> - Rietveld refinement plot for (a) AW, (b) AW1V, (c) AW2V, and (d) AW4V, microcrystals obtained by the CP method at 70 °C for 20 min.	24
<b>Figure 3</b> - Schematic representation of the crystalline unit cell of AWV with (x = 0.125 mol%) in the coordinates a (a), b (b), and c (c).....	26
<b>Figure 4</b> - Raman spectra of the samples: (a) AW, (b) AW1V, (c) AW2V, and (d) AW4V.....	27
<b>Figure 5</b> - Comparison between the relative positions of theoretical and experimental Raman active modes: Raman spectra of the (a) AW pure and (b) doped with vanadium. ....	28
<b>Figure 6</b> - Core level XPS spectra of Ag 3d (a-d) and W 4f for the samples (e-h). ....	32
<b>Figure 7</b> - (a-d) Core-level XPS spectra of O 1s and (e) V 2p for the samples. ....	33
<b>Figure 8</b> - Survey XPS of the samples. ....	34
<b>Figure 9</b> - Diffuse Reflectance Spectroscopy of the pure and V-doped sample.....	35
<b>Figure 10</b> - PL spectrum of the pure and V-doped sample.....	36
<b>Figure 11</b> - FE-SEM images for (a) AW, (b) AW1V, (c) AW2V, and (d) AW4V. ....	38
<b>Figure 12</b> - Average height (a-d) and width (e-h) distribution of AW and AWV samples.....	39
<b>Figure 13</b> - Schematic representation of the energy profile to obtain the as synthesized morphologies. The experimental morphologies are inserted for comparison purpose.....	41

<b>Figure 14</b> - X-band EPR spectra of the undoped (AW) and V-doped (AW1V, AW2V, and AW4V) samples recorded at 120 K. (a) Magnetic field swept from 225 to 435 mT. (b) Magnetic field swept from 320 to 365 mT. The background spectrum (BKGD) was obtained by measuring na empty samples tube. ....	44
<b>Figure 15</b> - (a) Thionisole oxidation reaction scheme; (b) conversion and selectivity of different catalysts to thioanisole oxidation; (c) thionisole oxidation kinetics for AW and AW1V samples; (d) catalytic scope using AW1V catalyst; (e) 10-fold scaled catalytic recycle for the oxidation reaction using AW1V catalyst; (f) scavenger tests in the oxidation reaction using AW1V catalyst.....	50
<b>Figure 16</b> - XRD and Rietveld refinements of the samples. (a) ZGO; (b) ZGO1; (c) ZGO16; (d) ZGO-1000; (e) ZGO1-1000, and (f) ZGO16-1000. ....	53
<b>Figure 17</b> - XRD and Rietveld refinements of the samples. (a) ZGO2; (b) ZGO2-1000; (c) ZGO 4; (d) ZGO4-1000; (e) ZGO8; and ZGO8-1000.....	55
<b>Figure 18</b> - (a) Raman spectra and (b) FTIR spectra of the samples. ....	58
<b>Figure 19</b> - Raman spectroscopy (a) and FTIR (b) spectra for samples with intermediate concentrations (2, 4, and 8% Ni).....	60
<b>Figure 20</b> - FE-SEM images of the samples (a) ZGO, (b) ZGO1, (c) ZGO16, (d) ZGO-1000, (e) ZGO1-1000, and ZGO16-1000. ....	61
<b>Figure 21</b> - FE-SEM images of the samples with intermediate concentrations: (g) ZGO2, (h) ZGO4, (i) ZGO8, (j) ZGO2-1000, (k) ZGO4-1000, and (l) ZGO8-1000.....	62
<b>Figure 22</b> - Ge 3d XPS spectra of the ZGO samples (a) Zn 2p XPS spectra of the ZGO samples (b) O 1s XPS spectra of the ZGO samples (c) Ni 2p XPS spectra of Ni <sup>2+</sup> -doped ZGO samples. ....	64
<b>Figure 23</b> - Energy of band gap (E <sub>gap</sub> ) of the samples. (a) ZGO; (b) ZGO1; (c) ZGO16; (d) ZGO-1000; (e) ZGO1-1000, and (f) ZGO16-1000.....	67



<b>Figure 24</b> - Energy of band gap ( $E_{\text{gap}}$ ) of the samples with intermediate concentrations (2, 4, and 8% Ni).....	67
<b>Figure 25</b> - (a) DOS projected onto the atoms within the $[\text{ZnO}_4]$ neighbor, $[\text{ZnO}_4]$ that was replaced by $\text{Ni}^{2+}$ cation, and $[\text{GeO}_4]$ neighbor clusters at the ZGO model. (b) DOS projected onto the atoms within the $[\text{ZnO}_4]$ neighbor, $[\text{NiO}_4]$ , and $[\text{GeO}_4]$ neighbor clusters at the Ni-ZGO model.....	69
<b>Figure 26</b> - DOS projected to 3d orbitals from Ni atom at Ni-ZGO model. ....	70
<b>Figure 27</b> - Schematic representation of the $[\text{NO}_4]$ , neighbor $[\text{ZnO}_4]$ (at the six-membered rings composed only by $\text{Zn}_2$ sites) and $[\text{GeO}_4]$ (at the six-membered rings composed by $\text{Z}_1$ sites and Ge). Values of the Mulliken charges and the respective metal electronic configuration induced by the $\text{Ni}^{2+}$ -doping process.....	71
<b>Figure 28</b> - Spectra of absorption in the UV-Vis and NIR regions for the samples (a) untreated and (b) thermally treated.....	73
<b>Figure 29</b> - Spectra of absorption in the UV-Vis and NIR regions for the samples with intermediate concentrations (2, 4, and 8% Ni). ....	73
<b>Figure 30</b> - (a) $a^*$ (green and red), $b^*$ (yellow and blue) and (b) and $L^*$ (lightness, with 100 representing white and 0 representing black) CIELab coordinates for the samples.....	75
<b>Figure 31</b> - (a) $a^*$ (green and red), $b^*$ (yellow and blue), and (b) and $L^*$ (lightness, with 100 representing white and 0 representing black) CIELab coordinates for the samples with intermediate concentrations (2, 4, and 8% Ni).....	76
<b>Figure 32</b> - Images of pure and Ni-doped powders at various concentrations (0 to 16% Ni).....	78

## RESUMO

MODULAÇÃO DE SEMICONDUTORES COM METAIS DE TRANSIÇÃO: PROPRIEDADES MORFOLÓGICAS, ÓPTICAS E ELETRÔNICAS. A pesquisa sobre semicondutores tem sido de grande interesse devido às suas inúmeras aplicações. Esses materiais são versáteis, e a dopagem, que introduz impurezas na estrutura cristalina, é uma estratégia comum que pode melhorar suas propriedades. Esse processo influencia diretamente as propriedades eletrônicas, ópticas e morfológicas, permitindo ajustes para otimizar a eficácia dos semicondutores em aplicações específicas. Nesse contexto, este estudo introduz duas matrizes: o tungstato de prata ( $\alpha$ -Ag<sub>2</sub>WO<sub>4</sub> ou AW) e o germanato de zinco (Zn<sub>2</sub>GeO<sub>4</sub> ou ZGO), cada uma dedicada a investigar a influência da dopagem com metais de transição. No caso do AW dopado com vanádio em diferentes concentrações ( $x = 0,0; 0,01; 0,02; e 0,04$  mol%), foi demonstrado como um catalisador altamente eficiente para a oxidação de sulfetos a sulfonas em condições brandas, apresentando altos rendimentos e seletividade. Experimentos com sequestradores identificaram o envolvimento direto de pares de elétron-buraco (e<sup>-</sup>/h<sup>+</sup>), radical hidroxila (•OH) e oxigênio singlete (<sup>1</sup>O<sub>2</sub>) no processo de oxidação. Análises de ressonância paramagnética eletrônica (RPE) e espectroscopia de fotoelétrons excitados por raios-X (XPS) confirmaram a presença de cátions V<sup>4+</sup> nas amostras dopadas. Resultados teóricos sugeriram que a maior atividade catalítica das amostras dopadas com vanádio está associada à predominância da presença da superfície (100) na morfologia do material, indicando potenciais aplicações em reações de oxidação de sulfetos a sulfonas na ausência de luz. Já para o ZGO dopado com níquel em diferentes concentrações ( $x = 0, 0,01 e 0,16$  mol%), a dopagem foi utilizada para ajustar suas propriedades estruturais e eletrônicas, visando a criação de pigmentos azuis eficientes para cerâmica. Cálculos de teoria do funcional da densidade (DFT) revelaram que os orbitais 3d do Ni<sup>2+</sup> geram novos níveis de energia, alterando a estrutura eletrônica local e resultando em transferência de elétrons que produzem a cor azul. Análises confirmaram que essa modificação é responsável pela tonalidade azul, além de destacar a baixa toxicidade e excelente durabilidade química e térmica dos pigmentos. Este trabalho estabelece uma base sólida para o design de pigmentos cerâmicos ajustáveis e de alto desempenho. Por fim, esses materiais demonstram o potencial da pesquisa científica para impulsionar inovações e melhorias significativas em tecnologias e produtos do mundo real.

## ABSTRACT

MODULATION OF SEMICONDUCTORS WITH TRANSITION METALS: MORPHOLOGICAL, OPTICAL, AND ELECTRONIC PROPERTIES. Research on semiconductors has been of great interest due to their numerous applications. These materials are versatile, and doping, which introduces impurities into the crystal structure, is a common strategy that can enhance their properties. This process directly influences the electronic, optical, and morphological properties, allowing for adjustments to optimize the effectiveness of semiconductors in specific applications. This process directly influences the electronic, optical, and morphological properties of semiconductors, enabling adjustments to optimize their effectiveness for specific applications. Within this context, this study introduces two matrices: silver tungstate ( $\alpha$ -Ag<sub>2</sub>WO<sub>4</sub> or AW) and zinc germanate (Zn<sub>2</sub>GeO<sub>4</sub> or ZGO), each dedicated to investigating the influence of doping with transition metals. For AW doped with vanadium at different concentrations ( $x = 0.0$ ; 0.01; 0.02; and 0.04 mol%), it was demonstrated as a highly efficient catalyst for the oxidation of sulfides to sulfones under mild conditions, exhibiting high yields and selectivity. Sequestration experiments identified the direct involvement of electron-hole (e<sup>-</sup>/h<sup>+</sup>) pairs, hydroxyl radical ( $\bullet$ OH), and singlet oxygen (<sup>1</sup>O<sub>2</sub>) in the oxidation process. Electron paramagnetic resonance (EPR) and X-ray photoelectron spectroscopy (XPS) analyses confirmed the presence of V<sup>4+</sup> cations in the doped samples. Theoretical results suggested that the enhanced catalytic activity of vanadium-doped samples is associated with the predominant presence of the (100) surface morphology, indicating potential applications in sulfide oxidation reactions in the absence of light. For ZGO doped with nickel at different concentrations ( $x = 0$ , 0.01, and 0.16 mol%), doping was utilized to tailor its structural and electronic properties towards creating efficient blue pigments for ceramics. Density functional theory (DFT) calculations revealed that the 3d orbitals of Ni<sup>2+</sup> generate new energy levels, altering the local electronic structure and resulting in electron transfer that produces the blue color. Analyses confirmed that this modification is responsible for the blue hue, while also highlighting the low toxicity and excellent chemical and thermal durability of the pigments. This work establishes a robust foundation for the design of adjustable and high-performance ceramic pigments. Ultimately, these materials demonstrate the potential of scientific research to drive significant innovations and improvements in real-world technologies and products.

## SUMÁRIO

<b>1 - INTRODUCTION.....</b>	<b>1</b>
<b>1.1 - SILVER TUNGSTATE .....</b>	<b>1</b>
<i>1.1.1 - V-doped materials.....</i>	<i>4</i>
<b>1.2 - ZINC GERMANATE .....</b>	<b>5</b>
<i>1.2.1 - Ni-doped materials .....</i>	<i>9</i>
<b>2 - OBJECTIVES .....</b>	<b>10</b>
<b>2.1 - V-DOPED AW SAMPLES .....</b>	<b>10</b>
<b>2.2 - NI-DOPED ZGO SAMPLES.....</b>	<b>10</b>
<b>3 - METHODOLOGY .....</b>	<b>12</b>
<b>3.1 - SYNTHESIS OF THE MATERIALS.....</b>	<b>12</b>
<i>3.1.1 - V-doped AW samples .....</i>	<i>12</i>
<i>3.1.2 - Ni-doped ZGO .....</i>	<i>14</i>
<b>3.2 - CHARACTERIZATION METHOD .....</b>	<b>15</b>
<i>3.2.1 - X-ray diffraction .....</i>	<i>16</i>
<i>3.2.2 - Refinement of Rietveld.....</i>	<i>16</i>
<i>3.2.3 - Raman spectroscopy.....</i>	<i>17</i>
<i>3.2.4 - Diffuse Reflectance Spectroscopy.....</i>	<i>17</i>
<i>3.2.5 - Fiel emission scanning electron microscopy.....</i>	<i>18</i>
<i>3.2.6 - X-ray Photoelectron Spectroscopy .....</i>	<i>18</i>
<i>3.2.7 - Photoluminescence .....</i>	<i>18</i>
<i>3.2.8 - Electron Paramagnetic Resonance .....</i>	<i>19</i>
<i>3.2.9 - Inductively coupled plasma optical emission spectrometry .....</i>	<i>19</i>
<i>3.2.10 - Fourier-transform infrared spectroscopy.....</i>	<i>20</i>
<i>3.2.11 - Energy-Dispersive Spectroscopy .....</i>	<i>20</i>
<i>3.2.12 - Colorimetric.....</i>	<i>20</i>

<b>4 - RESULTS</b> .....	<b>22</b>
<b>4.1 - V-DOPED AW</b> .....	<b>22</b>
4.1.1 - <i>DRX and Refinement of Rietveld</i> .....	22
4.1.2 - <i>Raman spectroscopy</i> .....	26
4.1.3 - <i>X-ray Photoelectron Spectroscopy</i> .....	30
4.1.4 - <i>DRS</i> .....	34
4.1.5 - <i>PL</i> .....	35
4.1.6 - <i>FE-SEM</i> .....	37
4.1.7 - <i>Theoretical Morphology</i> .....	40
4.1.8 - <i>EPR</i> .....	42
4.1.9 - <i>Catalytic</i> .....	48
<b>4.2 - NI-DOPED ZGO</b> .....	<b>53</b>
4.2.1 - <i>XRD and Rietveld</i> .....	53
4.2.2 - <i>Raman and FTIR</i> .....	58
4.2.3 - <i>FE-SEM</i> .....	60
4.2.4 - <i>EDS</i> .....	62
4.2.5 - <i>XPS</i> .....	63
4.2.6 - <i>Energy of band gap</i> .....	65
4.2.7 - <i>DOS</i> .....	68
4.2.8 - <i>DRS</i> .....	72
4.2.9 - <i>Colorimetric</i> .....	74
<b>5 - CONCLUSIONS</b> .....	<b>79</b>
<b>5.1 - V-DOPED AW</b> .....	<b>79</b>
<b>5.2 - NI-DOPED ZGO</b> .....	<b>80</b>
<b>6 – REFERENCES</b> .....	<b>82</b>
<b>6.1 – V-DOPED AW (1-83)</b> .....	<b>82</b>
<b>6.2 - NI-DOPED ZGO (84-145)</b> .....	<b>88</b>

## 1 - Introduction

Scientific investigation into semiconductors has been the subject of interest for several decades due to their wide range of applications. These materials exhibit remarkable versatility, including antimicrobial properties, photocatalytic activity, gas sensing, pigments, among others.

The ability to modify the intrinsic properties of semiconductors emerges as a central focus of research, offering significant opportunities to enhance their efficiency. One common approach to altering such properties is doping, which involves the controlled introduction of impurities into the crystalline lattice of the host material. This strategy directly influences the electrical, optical, and morphological characteristics, allowing adjustments that can optimize their effectiveness for a specific application.

### 1.1 - Silver tungstate

In recent years,  $\alpha$ -silver tungstate ( $\alpha$ -Ag<sub>2</sub>WO<sub>4</sub> or AW) have been extensively studied due to their multifunctionality in areas such as photocatalysis [1,2], catalysis [3-5], antifungal and bactericidal behavior [6-8], tumor identification and uptake [9], and gas detection [10,11]. Recently, GOUVEIA et al. [12] reviewed AW as a multifunctional semiconductor. The authors highlighted its effectiveness as a photocatalyst in pollutant degradation, its application in catalytic processes, and its potential in biomedical and gas detection applications. The study provides an overview of the key properties and applications of AW-based materials.

The properties of AW as a semiconductor depend heavily on the synthesis method and reaction conditions, such as pH, temperature, and so

on. For example, NETO et al. [13] investigated the effect of temperature on the morphology and optical properties of AW prepared by the co-precipitation method, focusing on the material's photocatalytic activity. During synthesis, different temperatures were explored, showing a significant effect on the morphology of AW crystals, resulting in varying shapes and sizes of particles. Additionally, the study examined the relationship between morphology and photocatalytic activity, particularly in the degradation of organic dyes under UV irradiation. The results indicate a correlation between the material's morphology and its effectiveness in pollutant degradation, highlighting the importance of morphology control for optimizing the photocatalytic properties of AW.

MACEDO et al. [14] investigated the influence of the anionic surfactant sodium dodecyl sulfate (SDS) during the synthesis of AW and analyzed how this agent affects the morphology and photocatalytic activity of the material. Using controlled precipitation methods, they were able to manipulate the morphology of AW, resulting in different crystal forms, such as the cuboid shape. These variations in material morphology had a direct impact on its photocatalytic activity, especially in the degradation of dyes under UV light. The cuboid morphology provides a larger contact area and exposure of active surfaces, promoting interaction with reactants and enhancing the efficiency of photocatalytic processes. These findings underscore the importance of morphology control in optimizing the photocatalytic properties of AW for environmental and technological applications.

FOGGI et al. [8] investigated how the choice of solvent affects the morphology, optical properties, and antimicrobial activity of AW. During the study, microcrystals were prepared in different solvents using a controlled co-precipitation method, resulting in distinct forms: flower-like structures when using water and ammoniacal solution, and nanorods when

using ethanol. Notably, the nanorods demonstrated higher effectiveness in antimicrobial activity, attributed to their ability to generate oxidizing radicals such as hydroxyl radical and hydrogen peroxide. This study highlights how the synthesis process can directly influence the properties of AW, showcasing its adaptability and potential for antimicrobial applications. Very recently, we reported that the presence of carboxylic acids, as surfactants, in the reaction medium also directly influences the final morphology of the as-synthesized AW microcrystals [15].

The use of AW as catalyst has been much explored recently. SONG et al. [16] reported that AW is a highly efficient catalyst for the chemical fixation of carbon dioxide (CO<sub>2</sub>). GUO et al. [5] used AW as a bifunctional catalyst to simultaneously activate CO<sub>2</sub> and catalyze the direct carboxylation of terminal alkenes at room temperature. The catalytic synthesis of sulfoxides and sulfones is of recurring interest due to the importance of these compounds as intermediate reagents in the synthetic routes of numerous chemical and bioactive substances, [17-26] as well as for the desulfurization of fuels to eliminate contamination without producing any harmful and/or toxic by-products [27,28]. However, most existing procedures have drawbacks, such as high temperatures, extended reaction times, the use of large amounts of promoters and organic solvents, and difficulties in both the separation and the recycling of the catalyst.

Thus, the development of new technologies based on new and efficient catalysts that can minimize these impacts by using cleaner oxidants under mild conditions to achieve high selectivity and stability becomes crucial. To address this daunting challenge, new methods are needed for the controllable synthesis of high-efficiency catalysts. Recently, our research group demonstrated that semiconductors, including AW, are efficient and selective catalysts for the oxidation of sulfides to sulfones in the dark. [29, 30]



There are multiple factors that influence the catalytic activity of a catalyst, with the exposed surfaces at the morphology being a key factor. Doping the catalyst with transition metal cations provokes lattice strain and affect the charge distribution to effectively enhance the catalytic activity by modulating the d-band electronic structure. [31] To design and synthesize catalysts with desired active sites, it is necessary to understand and regulate the structure and electronic properties of the exposed surfaces at the atomic and molecular levels. Doping with Zn and Ni has been shown to change the morphology of as-synthesized AW samples to cobblestones. [32, 33] These morphological changes influence the number of active sites on the surface, and consequently, affect their performance in applications.

A promising transition metal cation for doping AW to enhance its catalytic properties is vanadium. Studies indicate that the addition of vanadium significantly activated the catalyst, resulting in high conversion of diphenyl sulfide to diphenyl sulfoxide. The amount of vanadium deposited on  $\text{TiO}_2$  influenced both the conversion and selectivity, with a gradual decrease observed as the vanadium content increased. [31]

### *1.1.1 - V-doped materials*

Vanadium (V) has an electronic configuration of  $[\text{Ar}] 4s^2 3d^3$  and can exhibit a variety of oxidation states ranging from -3 to +5. In its higher oxidation states, vanadium behaves as a Lewis acid and displays high oxophilicity. These properties make vanadium highly versatile: in metal alloys, it imparts lightness, tensile strength, and protection against rust and corrosion. Additionally, vanadium is utilized in redox flow batteries. In the biological sphere, it is essential for living organisms, participating in important redox reactions. [34]

The versatility of vanadium also extends to its use in catalysts, which has garnered significant attention from the scientific community. Abogabal et al. [35] demonstrated that vanadium-doped  $\text{MgFe}_2\text{O}_4$  showed greater efficiency in the photodegradation of methyl orange compared to the pure sample, while also exhibiting magnetic properties and high recyclability. Moreover, Weidner et al. showed that zinc oxide, used in selective catalytic reduction processes and as an electrode component in electrochemical applications, achieved a high nitrogen oxide conversion rate with a 3:1 ratio of ZnO to V. In cyclic voltammetry tests, the results indicated its potential as a feed material for lithium-ion cells. [36]

Studies conducted by our research group explored the doping of V-doped  $\text{TiO}_2$ , observing enhanced optical properties and morphological modifications. [37] Other researchers [31] used the same matrix as a catalyst in the oxidation of diphenyl sulfide to sulfoxides/sulfones, finding that a lower concentration of vanadium improved catalytic activity, leading to a high conversion of sulfides to sulfoxides/sulfones. These examples illustrate how the incorporation of vanadium into catalytic materials can significantly enhance their properties and performance.

## **1.2 - Zinc germanate**

Blue pigments have garnered substantial attention due to their potential applications in visual arts and various industrial uses, primarily owing to their photo-absorption characteristics in the lower visible region. For instance, LLUSAR et al. analyzed the incorporation of cobalt into various ceramic glazes for the production of blue pigments. The study revealed that the matrix with a low cobalt content exhibited the most intense blue hue across different types of glazes. These results highlight the

importance of selecting the appropriate concentration of the dopant material to achieve the desired coloration effects in ceramic applications.[84]

Transition metals and rare earth elements doping processes have a longstanding history in the ceramic industry, offering a promising avenue for blue pigment development. Examples include  $\text{YBO}_3$  doped with Mn cations for bluish-gray pigments used in building coatings to mitigate solar radiation absorption. [85] JING et al. [86] presented a study on the synthesis and characterization of environmentally friendly cold blue pigments derived from copper and strontium silicates doped with rare earth cations (Pr, Nd, and Sm), aiming for high near-infrared reflectance. After calcination at 900 °C, the pigments exhibited a near-infrared solar reflectance of approximately 63% and an intense blue color. However, despite the potential of these pigments, it is important to consider economic issues and access to these materials for large-scale production.

Despite the wide variety of currently available blue pigments, some have been developed using complex synthesis methods and require many hours in the heat treatment stage, eventually impacting the product's final price. SMITH et al. [87], for example, produced a blue pigment using the  $\text{YIn}_{1-x}\text{Mn}_x\text{O}_3$  matrix via a mixed oxide process ( $\text{Y}_2\text{O}_3$ ,  $\text{Mn}_2\text{O}_3$ , and  $\text{In}_2\text{O}_3$ ), which required an initial heat treatment of 12 hours at 1200 °C, followed by two cycles at 1300 °C, with grinding between the steps.

A similar synthesis method was employed by WANG et al. [88] to produce different shades of blue pigments from vanadium-zirconium silicate ( $\text{V-ZrSiO}_4$ ) after 5 hours at a temperature ranging from 500 to 900 °C. This prolonged heating process may increase energy consumption and extend the total manufacturing time of the ceramic pigment.

Other matrices, such as  $\text{Zn}_2\text{SiO}_4$ , also face challenges during high-temperature synthesis, as studied by EMEL et al. [89] Additionally, the calcination time can extend up to 12 hours. Despite this, studies sought

methods to produce blue pigments from the  $\text{Zn}_2\text{SiO}_4$  matrix doped with cobalt using wet reactions, which again led to the need for long hours of heat treatment. These studies observed that varying the concentration of cobalt generated different shades of blue and resulted in the formation of powders with mixed crystallographic phases. [90] The optimization of reaction time is a critical consideration in the production of pigments, not only concerning energy efficiency and material accessibility, but also in achieving the desired properties in the pigments.

$\text{Zn}_2\text{GeO}_4$  (ZGO), or zinc germanate, is a promising matrix for pigment production due to its properties as an inherently n-type semiconductor attributed to intrinsic donor defect states and direct band gap excitation (around 4.4 eV). Its straightforward synthesis across different scales and non-toxic properties have garnered attention from the scientific community. ZGO has various applications documented in the literature, including photocatalysis for water splitting, pollutant degradation, photocatalytic hydrogen generation, luminescent thermometers, UV detectors, among others. [91–95]

At room temperature, ZGO adopts a rhombohedral structure and can transform into different structures when exposed to high pressures and temperatures. Its well-established optical properties, coupled with native defects and solid ionic bonds (Zn–O and Ge–O), induce local lattice distortions, resulting in the creation of electronic levels within the band gap. [96-101]

Furthermore, the doping of this matrix with transition metal cations has been a subject of study, as demonstrated by SRIVASTAVA et al. [102] in their research. They observed that the ZGO matrix doped with  $\text{Mn}^{2+}$  exhibited variations in optical properties at different temperatures, revealing notable sensitivities for temperature detection. This characteristic endows the material with potential as a highly sensitive luminescent thermometer, in

addition to promising applications in optoelectronics. In another study, the ZGO doped with the same metal emerged as a potential phosphor for LEDs, security, and bioimaging due to its bright and persistent green luminescence, high quantum efficiency (~52%), and water dispersion capability. [103]

THAN et al. [104] observed in their research that the addition of chromium to ZGO, synthesized using hydrothermal methods, expands the crystalline structure, resulting in the emission of white-blue light when excited by ultraviolet light. This indicates the feasibility of tailoring the optical properties of ZGO through controlled doping, opening avenues for diverse applications in optoelectronics and beyond.

Recent studies suggest a possible application in producing blue pigments using  $\text{Co}^{2+}$ -doped ZGO through the solid-state ceramic route. [105]. However, the use of  $\text{Co}^{2+}$  faces notable challenges, such as its toxicity to humans and the environmental impacts associated with its mining [106, 107].  $\text{Ni}^{2+}$  doping at ZGO is expected to confer a rich color to ceramic pigments via the  $4s^23d^8$  configuration [105], depending on the concentration of  $\text{Ni}^{2+}$  cations and other elements in the host lattice [106, 108–110]. Some ceramic matrices were doped with  $\text{Ni}^{2+}$  and showed excellent viability in terms of forming blue pigments.

Costa et al. synthesized a turquoise-blue pigment based on  $\text{Ni}^{2+}$ -doped hibonite in a solid-state reaction, with potential applications in glazes and porcelain [111] Subsequently, IANOS et al. [108] synthesized cold blue pigments based on  $\text{Ni}^{2+}$  and  $\text{La}^{3+}$ -doped hibonite through combustion. KHAIRYA et al. [112] doped ZnO with  $\text{Ni}^{2+}$  cations using the coprecipitation method. They performed heat treatment at different temperatures, observing the attainment of various shades of blue and highlighting the direct influence of temperature.

### *1.2.1 - Ni-doped materials*

Nickel, with an electronic configuration of  $[\text{Ar}] 3d^8 4s^2$ , is widely applied across various fields. For instance, in semiconductors, doping materials like zinc oxide with nickel has induced morphological changes and increased structural defects. These modifications have resulted in a reduced band gap, enhancing visible light absorption, which is advantageous for applications such as solar cells and photocatalysts. [113]

In electrochemistry, studies indicate that nickel-based electrocatalytic materials show promise for hydrogen production via water electrolysis. The morphology and structure of these catalysts play a crucial role in their electrocatalytic performance, making it essential to control these characteristics. [114] In catalysis, Lillo et al. [115] investigated a metal complex known as dinuclear nickel peroxocarbonate, where nickel acts as the active site in oxidation reactions. This complex interacts with hydrogen peroxide and carbon dioxide, facilitating peroxide release and promoting oxidation. Additionally, in the production of blue pigments, nickel emerges as a less toxic alternative to cobalt.

Costa et al. [111] discuss the development of a new turquoise blue pigment made from nickel-doped hibonite, which not only influences the material's coloration but also contributes to its structural stability.

## 2 - Objectives

The objectives are divided into two parts, one for V-doped AW and the other for Ni-doped ZGO.

### 2.1 - V-doped AW samples

- Synthesize the pure material (AW) and the V-doped material (AWV) with controlled addition of the precursor ( $x = 0, 0.01, 0.02, 0.04$  mol%) using the coprecipitation method.
- Investigate the influence of V on the structural, optical, photoluminescent, and morphological properties of AW.
- Analyze the catalytic activity, which was evaluated and optimized for the oxidation of methyl phenyl sulfide (thioanisole) as a model reaction.
- To gain a deeper understanding of the relationship between morphology and catalysis at the atomic level, density functional theory (DFT) calculations were conducted.

### 2.2 - Ni-doped ZGO samples

- Synthesis of ZGO doped with  $\text{Ni}^{2+}$  at different concentrations ( $x = 0, 0.01, \text{ and } 0.16$  mol%) was carried out via coprecipitation followed by microwave-assisted hydrothermal treatment at  $140\text{ }^\circ\text{C}$  for 10 minutes.
- Characterization was performed using various techniques for both the pure and doped samples.

- Density functional theory (DFT) calculations were employed to understand the local geometry and density of states (DOS) of Ni<sup>2+</sup>-doped ZGO.



## 3 - Methodology

### 3.1 - Synthesis of the materials

#### 3.1.1 - V-doped AW samples

The synthesis of the V-doped AW samples was performed using the coprecipitation method (CP) in an aqueous medium. For the pure sample, two separate aqueous solutions were prepared, one containing  $\text{Na}_2\text{WO}_4 \cdot 2\text{H}_2\text{O}$  (0.001 M, Sigma-Aldrich, 99.5%) and the other containing  $\text{AgNO}_3$  (0.002 M, Sigma-Aldrich, 99.8%). They were then mixed under constant agitation and heated to 70 °C, and the  $\text{AgNO}_3$  solution was added to the  $\text{Na}_2\text{WO}_4 \cdot 2\text{H}_2\text{O}$  solution. This resulted in the formation of a suspension, which was kept under stirring and constant temperature for 20 minutes, resulting in the formation of a white precipitate. The precipitate was washed several times with deionized  $\text{H}_2\text{O}$  and centrifuged to remove any residual ions.

For the V-doped samples, the synthesis process was similar, except that the two aqueous solutions used were  $\text{NH}_4\text{VO}_3$  (0.002 M, Sigma-Aldrich, 99%) and  $\text{AgNO}_3$  (0.002M, Sigma-Aldrich, 99.8%), which were mixed under agitation and heated to 70 °C. In the  $\text{NH}_4\text{VO}_3$  solution,  $\text{Na}_2\text{WO}_4 \cdot 2\text{H}_2\text{O}$  (0.001 M) was added under agitation, followed by the addition of the  $\text{AgNO}_3$  solution. After the addition, a yellow precipitate was obtained.

After the complete characterization of the samples (pure and doped), the material was tested for the catalytic oxidation of sulfides. The catalytic tests were conducted in 4 mL round-bottom flasks with magnetic stirring at 700 rpm/min. The experimental procedure involved dispersing AW (10 mg) in a mixture of 0.1 mmol of sulfide, 2 mL of solvent, and 15

$\mu\text{L}$  of hexadecane as an internal standard. Then,  $\text{H}_2\text{O}_2$  (30% (w/v)) was added as the oxidant. The reaction conditions such as time, temperature,  $\text{H}_2\text{O}_2$  amount, solvent, and catalyst loading were varied to optimize the yield and selectivity for the transformation to sulfoxide and sulfone. The reaction solutions were diluted in 2 mL of ethyl acetate and analyzed by gas chromatography (GC, Agilent 8860) with flame-ionization detection (FID), using a non-polar (5%-phenyl)-methylpolysiloxane column (Agilent J&W HP-5). For catalytic recycles (up to 5 recycles), the experiment was scaled up by a factor of 10 in the best condition.

The experiments with ionic species were carried out using equimolar amounts of  $\text{AgNO}_3$ ,  $(\text{NH}_4)_3\text{VO}_4$ , and  $\text{Na}_2\text{WO}_4 \cdot 2\text{H}_2\text{O}$ . For experiments using scavengers, equimolar amounts of reagents and catalyst were used. The scavengers used were  $\text{AgNO}_3$  to capture electrons ( $e^-$ ), [34] ammonium oxalate ( $(\text{NH}_4)_2\text{C}_2\text{O}_4$ ) for holes ( $h^+$ ), [35] potassium hydrogen phthalate (PHP) for hydroxyl radicals ( $\bullet\text{OH}$ ), [36] and sodium azide ( $\text{NaN}_3$ ) for singlet oxygen ( $^1\text{O}_2$ ). [37]

To gain a deeper understanding of the relationship between morphology and catalysis at the atomic level, density functional theory (DFT) calculations were conducted. The good match between the exposed surfaces at the morphology, derived from electron microscopy images, and our predicted morphologies obtained theoretically, allows us to be confident in our results. Based on the results, we propose a mechanism to explain the changes in catalytic activity after the V-doping process based on the presence of (100) surface at the morphology. To the best of our knowledge, no study has reported on this topic, in which vanadium is doped into AW microcrystals to further increase their efficiency as catalysts in the dark.

### 3.1.2 - Ni-doped ZGO

The ZGO samples were synthesized using the coprecipitation method followed by microwave-assisted hydrothermal treatment at 140 °C for 10 minutes. Two aqueous solutions of metal precursors were prepared separately for the pure sample. The first solution contained zinc nitrate hexahydrate ( $\text{Zn}(\text{NO}_3)_2 \cdot 6\text{H}_2\text{O}$  - Chem Impex Inc, 99.84%), while the second was prepared from the dissolution of germanium oxide ( $\text{GeO}_2$  - Sigma Aldrich, 99.99%). Subsequently, these solutions were mixed under constant stirring and heated to 70 °C. This process resulted in a homogeneous solution kept under continuous stirring and temperature for 5 minutes. Then, the pH was adjusted to 10 with the addition of NaOH, with constant stirring until the formation of a suspension, which took approximately 15 minutes. The mixture was then transferred to a Teflon reactor and subjected to microwave irradiation at 140 °C for 10 minutes, using 2.45 GHz and power of 800 W, resulting in the formation of a white precipitate. After this step, the residue was subjected to several washes with deionized water and centrifuged to remove residual ions.

In the synthesis of Ni-doped ZGO, the synthesis process was similar, with the difference that nickel nitrate hexahydrate ( $\text{Ni}(\text{NO}_3)_2 \cdot 6\text{H}_2\text{O}$  - Sigma Aldrich, 99%) was also added to the zinc nitrate solution in the proportions of 1 and 16%. After adding  $\text{Ni}^{2+}$  cations, a color modification was observed, initially changing from white to a greenish hue. These samples underwent heat treatment at 1000 °C for 2 hours to investigate the thermal-colorimetric stability of the produced powders. The samples of pure, doped with 1%, and doped with 16% Ni were named ZGO,  $\text{Zn}_{1.98}\text{Ni}_{0.02}\text{GeO}_4$  (ZGO1), and  $\text{Zn}_{1.68}\text{Ni}_{0.32}\text{GeO}_4$  (ZGO16), respectively, while the samples subjected to thermal treatment were referred to as ZGO-1000, ZGO1-1000, and ZGO16-1000, respectively.

To complement the experimental findings and systematically explore the structural evolution of Ni<sup>2+</sup> in ZGO, density functional theory (DFT) calculations were undertaken to understand the local geometry and density of states (DOS) of Ni<sup>2+</sup>-doped ZGO, particularly [NiO<sub>4</sub>] and the tetrahedral [ZnO<sub>4</sub>] and [GeO<sub>4</sub>] neighbor clusters. Our theoretical and experimental results provide deep insights into the colorimetric properties of Ni<sup>2+</sup>-doped ZGO. This opens an exciting way to develop ZGO-based materials as blue pigments. First-principles calculations for ZGO and Ni-doped ZGO (Ni-ZGO) models were performed using the CRYSTAL17 software package.[30,31] The computational methods are based on the DFT calculations at the B3LYP hybrid functional level were performed.[32,33] The diagonalization of the Fock matrix was performed using an adequate number of k-point grids in the reciprocal space. The thresholds controlling the accuracy of the Coulomb and exchange integrals calculations were set to  $1 \times 10^{-8}$  and  $1 \times 10^{-16}$ , respectively, and the percentage of Fock/Kohn-Sham matrix mixing was set to 30.

The Zn, Ge, Ni, and O atomic centers were described by 86-411d31G, DURAND-21G\*, 86-411(41d)G, and 6-31d1 basis sets, respectively. These were obtained from the CRYSTAL website [34]. The lattice parameters and internal atomic coordinates of the ZGO were fully optimized until all force components were less than  $10^{-6}$  eV Å<sup>-2</sup>.

### **3.2 - Characterization method**

Both materials in this study, (A) V-doped AW and (B) Ni-doped ZGO, are characterized using the same general technique, with specific methods applied to each material as needed.

- Part (A) and (B)

### 3.2.1 - X-ray diffraction

Among the material characterization methods, X-ray diffraction (XRD) stands out as a fundamental tool for identifying the crystalline phases present in materials, enabling the monitoring of phase evolution and the determination of their crystalline structure. X-ray diffraction analyses were conducted using a Max2500PC diffractometer (Rigaku-Japan), operated under conditions of 40kV and 150mA. The radiation utilized was  $\text{CuK}\alpha$  ( $\lambda = 1.5406 \text{ \AA}$ ), with a scanning rate of  $0.02^\circ/\text{min}$  in the  $2\theta$  range from  $5$  to  $110^\circ$ . The obtained diffractograms were compared with the patterns from the Joint Committee on Powder Diffraction Standards (JCPDS) relevant to the material under study.

### 3.2.2 - Refinement of Rietveld

Through the refinement, the average crystallite size was obtained through the Scherrer equation (Eq. 1), using the FWHM of the most intense peak. The Scherrer equation is described by:

$$D = \frac{0.89\lambda}{(\beta \cos\theta)} \quad (\text{Eq. 1})$$

$$\beta = \sqrt{(\beta_{\text{obs}}^2 + \beta_{\text{st}}^2)} \quad (\text{Eq. 2})$$

where  $D$  is the average crystallite size,  $\lambda$  is the X-ray wavelength ( $0.15406 \text{ nm}$ ),  $\beta_{\text{obs}}$  is FWHM,  $\beta_{\text{st}}$  is FWHM of  $\text{LaB}_6$  standard and,  $\theta$  is the Bragg angle. The lattice strain parameter can be obtained by equation 3:

$$\varepsilon = \frac{\beta}{(4 \tan\theta)} \quad (\text{Eq. 3})$$

### 3.2.3 - Raman spectroscopy

Raman spectroscopy is a material analysis technique that involves the inelastic scattering of visible light by molecules. This physical phenomenon results in a modification of the frequencies of scattered light compared to the incident light, allowing for the identification of molecular structures through their vibrational modes. [3] To conduct Raman spectroscopy in this study, a T64000 spectrometer (Horiba Jobin-Yvon, Japan) equipped with a CCD Synapse and an argon-ion laser detector operating at 514 nm was used.

### 3.2.4 - Diffuse Reflectance Spectroscopy

Diffuse Reflectance Spectroscopy (DRS) was carried out using a Varian Cary 5G spectrophotometer (Agilent, USA), covering a wavelength range from 200 to 800 nm and programmed for diffuse reflectance mode. Magnesium oxide (MgO) was employed as the reference material.

The band gap ( $E_{\text{gap}}$ ) was calculated using the Wood and Tauc method. [4] In this method,  $E_{\text{gap}}$  is related to absorbance and photon energy and has been widely employed in the study of new compounds. The equations used for the calculation are described below.

$$h\nu\alpha \propto (h\nu - E_g)^{\frac{1}{2}} \quad (\text{Eq. 4})$$

ou

$$(E\alpha)^2 \propto (E - E_g) \quad (\text{Eq. 5})$$

### *3.2.5 - Field emission scanning electron microscopy*

Field emission scanning electron microscopy (FE-SEM) is an advanced method utilized for visualizing the microstructure of materials. Typically, FE-SEM operations are conducted under high vacuum conditions to mitigate the interference caused by gas molecules on the electron beam and the emitted secondary and backscattered electrons used for Imaging. The morphologies and textures of the semiconductor were observed by FE-SEM using a Supra 35-VP operated at 10 kV (Carl Zeiss, Germany).

### *3.2.6 - X-ray Photoelectron Spectroscopy*

It is a surface analytical technique used to investigate the chemical composition, chemical structure, and oxidation state of elements on the surface of materials. XPS analyses were performed using an ESCA spectrometer (Scientia Omicron, Germany) with a monochromatic X-ray source of Al K $\alpha$  (1486.7 eV), and the binding energies of all elements were calibrated with reference to the C 1s peak at 284.8 eV.

- part (A)

### *3.2.7 - Photoluminescence*

Photoluminescence (PL) is a technique that employs a laser beam to record the light emitted by a material as it transitions from the excited state to the ground state when exposed to a laser beam. Analysis of the luminescence spectrum enables the identification of imperfections and impurities in the material. PL spectra were measured using a laser

(Cobolt/Zouk;  $\lambda = 355$  nm) with 50  $\mu$ W of incident potency focused on the 20  $\mu$ m position.

### *3.2.8 - Electron Paramagnetic Resonance*

EPR, known as Electron Paramagnetic Resonance, is a spectroscopic technique utilized to investigate paramagnetic systems, characterized by the presence of one or more unpaired electrons. It is frequently employed for the examination of molecular structures and the magnetic properties of materials. EPR spectra were acquired using a spectrometer model ELEXSYS E500T (Bruker, Germany) operating in the X-band (9-10 GHz) with a variable temperature accessory. The data acquisition parameters used for the measurements were 100.00 kHz modulation frequency, 1.00 mT modulation amplitude, 20.4 mW microwave power, 330 mT central field, 210 mT sweep width, and 20.48 ms conversion time. A total of 4096 data points were collected per scan, and the resulting spectra were the average of 5 scans.

### *3.2.9 - Inductively coupled plasma optical emission spectrometry*

Inductively coupled plasma optical emission spectrometry (ICP-OES) was used to estimate the chemical composition of the solutions during catalytic cycles, using an iCAP 7000 (Thermo Fisher Scientific, USA). EPR spectra were acquired using a spectrometer model ELEXSYS E500T (Bruker, Germany) operating in the X-band (9-10 GHz) with a variable temperature accessory. The data acquisition parameters used for the measurements were 100.00 kHz modulation frequency, 1.00 mT modulation amplitude, 20.4 mW microwave power, 330 mT central field, 210 mT sweep



width, and 20.48 ms conversion time. A total of 4096 data points were collected per scan, and the resulting spectra were the average of 5 scans.

- part B

### *3.2.10 - Fourier-transform infrared spectroscopy*

Fourier-transform infrared spectroscopy (FTIR) relies on identifying functional groups within molecules, which exhibit vibrational modes (either through stretching or bending in various ways) when exposed to specific wavelengths of light. Fourier-transform infrared spectroscopy (FTIR) analysis was performed on a Bomem-Michelson spectrophotometer, using the transmittance mode (model MB102) in the range of 250 to 1000  $\text{cm}^{-1}$ , employing KBr pellets as a reference.

### *3.2.11 - Energy-Dispersive Spectroscopy*

Elemental composition distributions of the samples were assessed using energy-dispersive spectroscopy (EDS), operating at 20 kV in BSE mode, coupled to a scanning electron microscope (Hitachi, TM4000 Plus).

### *3.2.12 - Colorimetric*

For the analysis of colorimetric coordinates of the acquired powders, a Minolta spectrophotometer, model CM2600d, was used with a wavelength range between 400 and 700 nm. The equipment was equipped with a standard D65-type light source (daylight), following CIELab

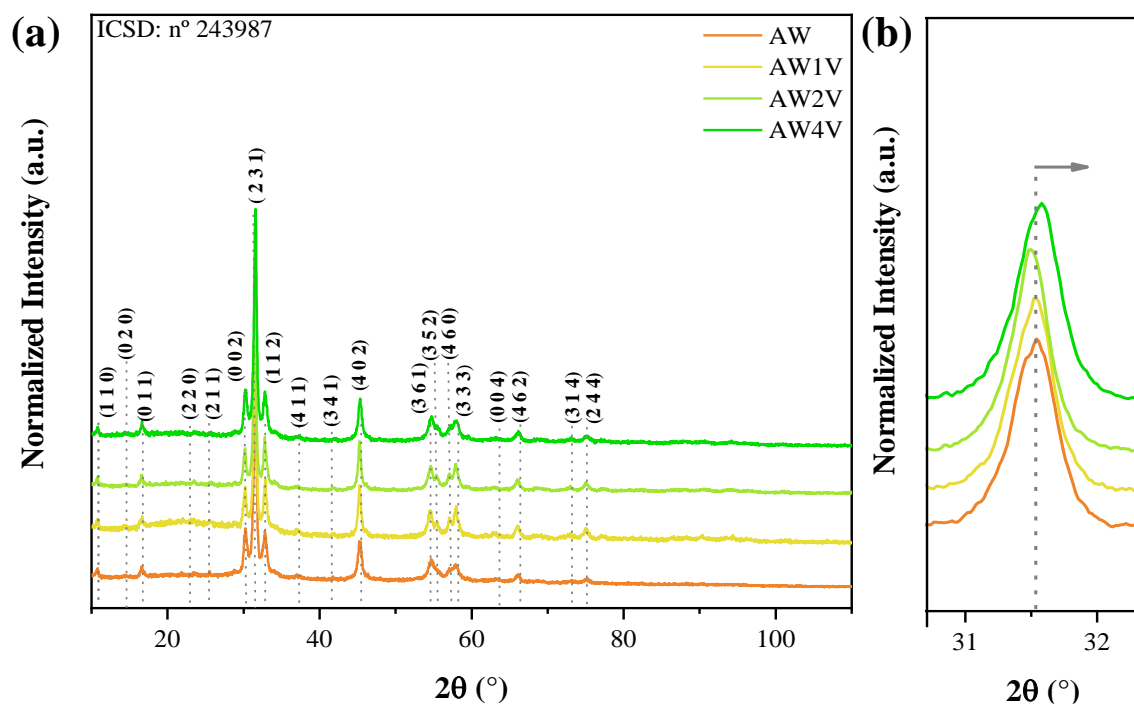
(International Commission of l'Eclairage - CIE) standards. The color difference between the powders was determined using Equation (2), considering the values of the colorimetric coordinates. These coordinates include Luminosity (L, ranging from 0 for black to 100 for white),  $a^*$  (positive values indicate red, negative values indicate green), and  $b^*$  (positive values indicate blue, negative values indicate yellow).

## 4 - Results

### 4.1 - V-doped AW

#### 4.1.1 - DRX and Refinement of Rietveld

Figure 1 presents the X-ray diffraction (XRD) patterns of V-doped AW samples [0.01% (AW1V), 0.02% (AW2V), and 0.04% (AW4V)], obtained using the coprecipitation (CP) method at room temperature. According to crystallographic card no. 243987 from the Inorganic Crystal Structure Database (ICSD), the samples have an orthorhombic structure with space group Pn2n and lattice parameters  $a = 10.8869 \text{ \AA}$ ,  $b = 12.0400 \text{ \AA}$ ,  $c = 5.90711 \text{ \AA}$ , and angles  $\alpha = \beta = \gamma = 90^\circ$ , with no presence of secondary phases. [43] All samples exhibit well-defined diffraction peaks, indicating a significant degree of structural order and long-range crystallinity.



**Figure 1** - (a) XRD patterns of the AW samples; (b) inset view of the main peak (231).

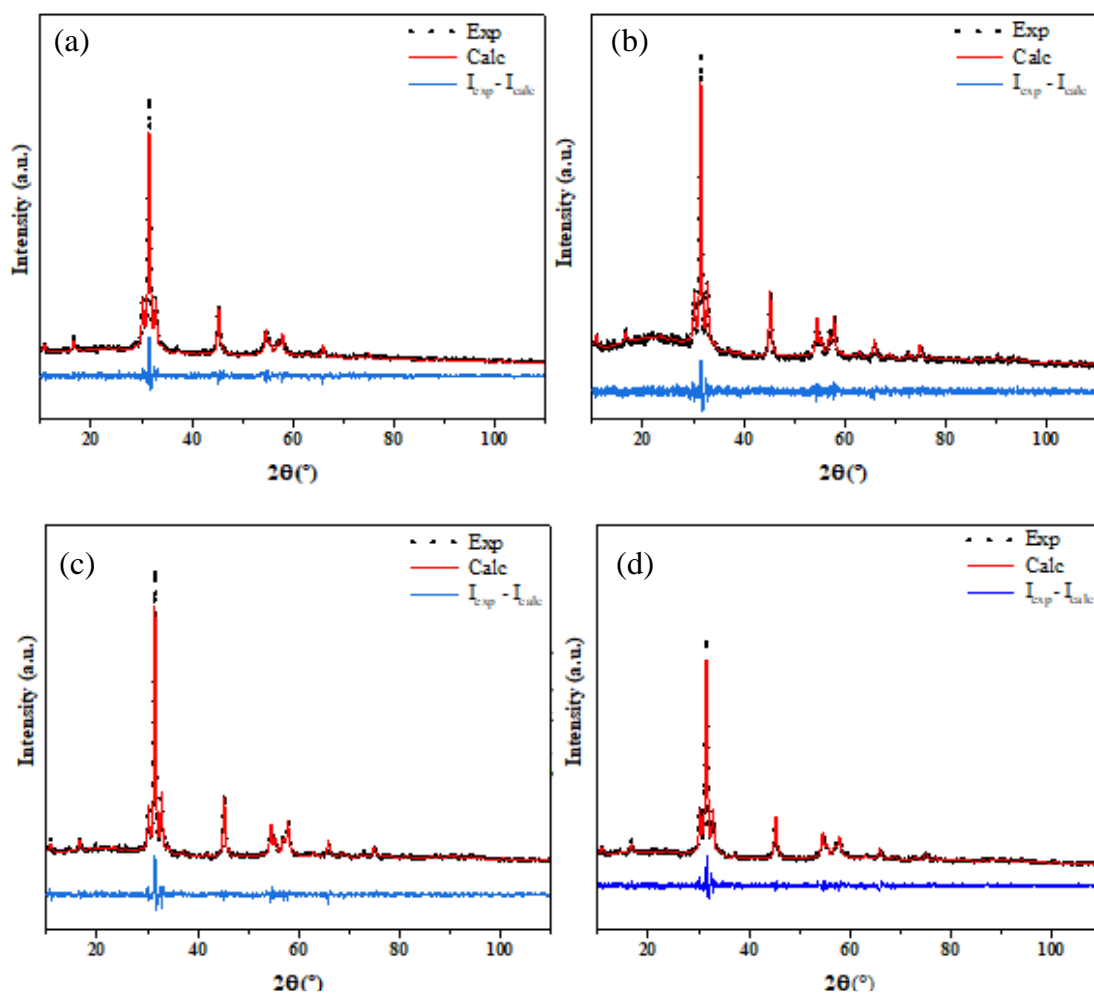
However, the comparison of the most intense diffraction peak (231) reveals a shift to higher  $2\theta$  values as the concentration of vanadium clusters (V-clusters) in the crystal structure increases. This behavior can be understood by analyzing the full width at half maximum (FWHM) values of the peak (231) [51]. The FWHM values for the samples are  $0.465^\circ$ ,  $0.379^\circ$ ,  $0.323^\circ$ , and  $0.389^\circ$  for AW, AW1V, AW2V, and AW4V, respectively (**Table 2**). The reduction in FWHM values observed in the samples (AW, AW1V, AW2V) may be associated with an increase in long-range structural order. On the other hand, the AW4V sample exhibits the highest FWHM value among the doped samples, which can be attributed to a higher concentration of V-clusters in the lattice, causing structural reorganization resulting in increased disorder. However, when comparing AW with AW4V, the doped sample still demonstrates superior structural order. Thus, the displacement observed in the main peak suggests distortions and polarization of dipoles/quadrupoles in the crystal lattice due to the successful substitution of  $[\text{WO}_6]$  clusters by V-clusters.

To confirm the amount of vanadium (V) incorporated into the AW crystal lattice in moles, analyses by ICP-OES were performed with the sample digested in concentrated nitric acid ( $\text{HNO}_3$ ). The results, presented in **Table 1**, show that the actual V concentrations are very close to the expected nominal values, indicating that the doping was effective.

**Table 1** - Comparison of the amount in mol of V (%) added to the nominal and real a AW crystal lattice.

Sample	[V] nominal (%)	[V] real (%)
AW	0.0000	0.0000
AW1V	0.0100	0.0092
AW2V	0.0200	0.0210
AW4V	0.0400	0.0438

The Rietveld refinement plots of the samples are presented in **Figure 2**. The results demonstrated good agreement between the experimental XRD patterns and the theoretical outcomes, based on ICSD card n°. 24398. Since the ionic radius of  $V^{4+}$  is slightly larger ( $0.62 \text{ \AA}$ ) than that of the replaced  $W^{6+}$  ion ( $0.60 \text{ \AA}$ ), a lattice expansion occurs to accommodate the cation substitution, which is reflected in the lattice parameter presented in **Table 2**.



**Figure 2** - Rietveld refinement plot for (a) AW, (b) AW1V, (c) AW2V, and (d) AW4V, microcrystals obtained by the CP method at  $70 \text{ }^{\circ}\text{C}$  for 20 min.

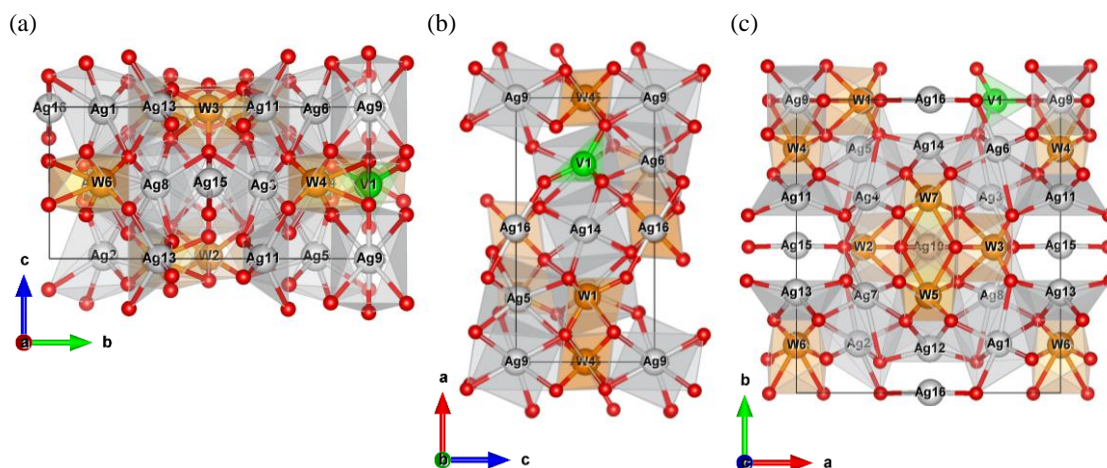
The formation of V-clusters results in a higher electronic density in the lattice, leading to an increase in lattice parameters and the

volume of the crystal cell (see **Table 2**). An increase in the value of D is observed in the V-doped samples due to local distortions and the redistribution of charge density caused by the V-doping process in the microcrystalline lattice of AW. In contrast, the  $\epsilon$  values of the samples show a general increase compared to the AW sample, suggesting that the substitution of  $[\text{WO}_6]$  clusters by V-clusters results in structural and electronic changes in the crystal lattice of AW.[60]

**Table 2** - Lattice parameters and unit cell volumes obtained by Rietveld refinement for the samples.

Sample	R <sub>wp</sub> (%)	R <sub>p</sub> (%)	$\chi^2$	a (Å)	b (Å)	c (Å)	V (Å <sup>3</sup> )	FWHM (°)	$\epsilon$	D (nm)
AW	11.26	8.60	1.369	10.81(2)	11.95(1)	5.85(5)	756.53(8)	0.465	0.651	18.559
AW1V	9.91	7.73	1.128	10.88(2)	12.04(4)	5.90(8)	774.43(8)	0.379	1.542	22.758
AW2V	10.18	7.98	1.437	10.88(5)	12.04(2)	5.90(6)	774.12(3)	0.323	1.919	26.723
AW4V	9.94	7.82	1.305	10.89(1)	12.04(3)	5.90(1)	774.10(1)	0.389	1.233	22.163
CIF	-	-	-	10.887	12.040	5.907	774.290	-	-	-
Calc.	-	-	-	11.127	12.335	5.825	799.518	-	-	-

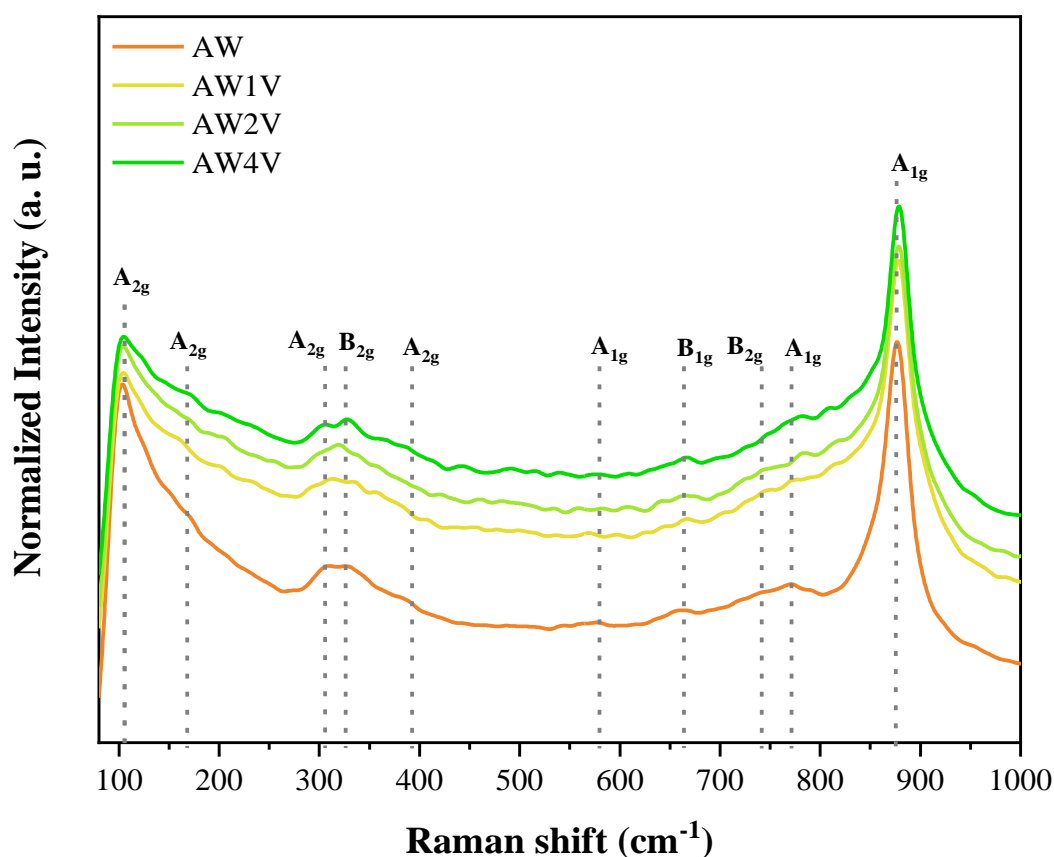
These alterations arise from the structural defects and polarization generated by the formation of V-clusters, in contrast to the octahedral clusters  $[\text{WO}_6]$ , and the local variation in electronic density in the lattice after the formation of new V-O bonds in the V-clusters. Furthermore, an increase in the size of the crystallites in the V-doped samples can be observed. According to the theoretical model, **Figure 3** illustrates that the V-cluster is surrounded by 4 oxygen atoms, constituting a distorted tetrahedral cluster  $[\text{VO}_4]$ .



**Figure 3** - Schematic representation of the crystalline unit cell of AWW with ( $x = 0.125$  mol%) in the coordinates a (a), b (b), and c (c).

#### 4.1.2 - Raman spectroscopy

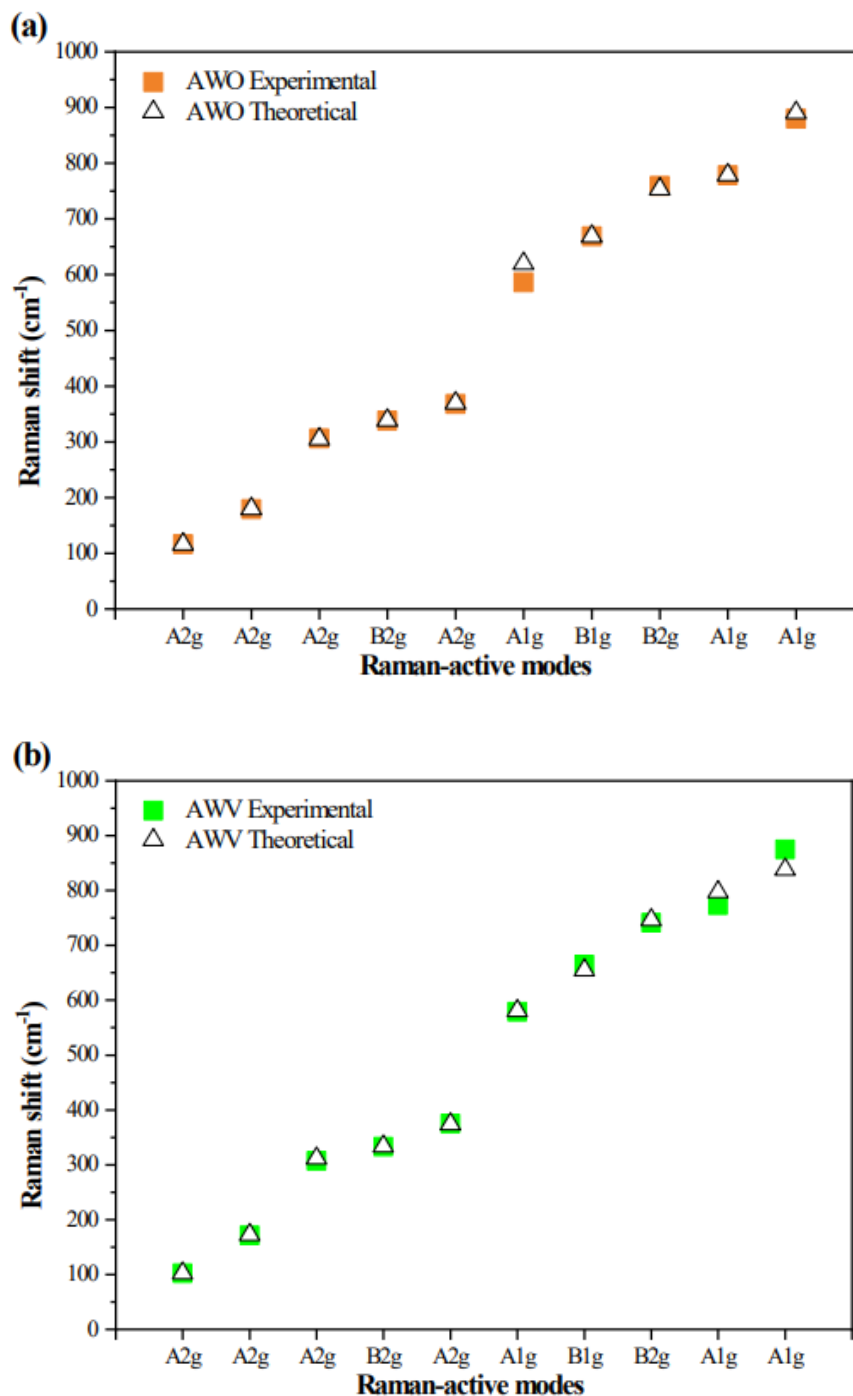
Raman spectroscopy plays a fundamental role in understanding the effects of short-range structural order/disorder in crystalline solids. As mentioned earlier in the XRD results, the samples exhibit an orthorhombic structure, suggesting the presence of 21 characteristic vibrational modes. These modes can be categorized into two groups: internal (related to the molecular vibration of the  $[\text{WO}_6]$  complex) and external (associated with the movement of the  $\text{Ag}^+$  ion). [61-63] However, in the Raman spectra, only 10 active modes are observed in the range between  $50$  and  $1000\text{ cm}^{-1}$  (**Figure 4**).



**Figure 4** - Raman spectra of the samples: (a) AW, (b) AW1V, (c) AW2V, and (d) AW4V.

In **Figure 4**, the most intense peak, at  $875\text{ cm}^{-1}$  ( $A_{1g}$ ), is attributed to the asymmetric stretching of the O–W bonds in  $[WO_6]$ . The modes at  $773\text{ cm}^{-1}$  ( $A_{1g}$ ) and  $741\text{ cm}^{-1}$  ( $B_{2g}$ ) correspond to the symmetric stretching of WOOW and W–O, while the mode at  $665\text{ cm}^{-1}$  ( $B_{1g}$ ) is related to the symmetric stretching of WOOW. The modes at  $579\text{ cm}^{-1}$  ( $A_{1g}$ ),  $385\text{ cm}^{-1}$  ( $A_{2g}$ ), and  $333\text{ cm}^{-1}$  ( $B_{2g}$ ) are associated with the bending vibrations of the W–O–W bond angle and the W–O–O–W dihedral angle. In turn, the mode at  $308\text{ cm}^{-1}$  ( $A_{2g}$ ) is linked to the out-of-plane bending of WOOW. Finally, the modes below  $251\text{ cm}^{-1}$  are pertinent to the external vibrational modes between the  $Ag^+$  and  $WO_4^{2-}$  groups.[64] These results are in agreement with the theoretically obtained frequencies presented in **Figure 5**.





**Figure 5** - Comparison between the relative positions of theoretical and experimental Raman active modes: Raman spectra of the (a) AW pure and (b) doped with vanadium.

In **Figure 4**, it is evident that the increase in the concentration of [VO<sub>4</sub>] clusters in the crystal structure of AW results in a reduction in the intensity and definition of the modes. The substitution of [WO<sub>6</sub>] clusters with

[VO<sub>4</sub>] clusters likely induces short-range disorder due to the presence of imperfections in the crystal structure of AW. In contrast, the study by PINATTI et al. [65] showed that the addition of europium to AW created vacancies in the host matrix, which reduced material stress and resulted in better-defined vibrational modes.

**Table 3** presents a comparison between the experimental Raman modes of this study, theoretical values, and literature data, showing satisfactory agreement.

**Table 3** - Comparison between experimental and active theoretical Raman modes of this study and the literature.

Mode	This work		Literature			
	Experimental	Theoretical	Sreedevi et al. <sup>58</sup>	Pereira et al. <sup>59</sup>	Pinatti et al. <sup>57</sup>	Longo et al. <sup>60</sup> (theoretical)
A <sub>1g</sub>	-		44	-	-	40.4
A <sub>1g</sub>	-		60	60	59	54.1
B <sub>1g</sub>	-		92	82	81	87
A <sub>2g</sub>	102		116	116	114	112.2
A <sub>2g</sub>	171		182	179	179	152.4
A <sub>1g</sub>	-		208	206	204	212.4
B <sub>1g</sub>	-		248	249	249	246.2
A <sub>2g</sub>	307		306	306	301	308.6
B <sub>2g</sub>	333		336	338	-	329.6
A <sub>2g</sub>	375		366	368	365	369.5
B <sub>2g</sub>	-		488	486	-	450.8
B <sub>2g</sub>	-		510	508	-	523.4
B <sub>2g</sub>	-		546	-	-	564.2
A <sub>1g</sub>	579		590	586	584	599.4
B <sub>1g</sub>	-		629	-	-	628.6
B <sub>1g</sub>	665		667	669	662	662.8
B <sub>1g</sub>	-		730	728	-	712.7
B <sub>2g</sub>	741		754	759	755	716.6
A <sub>1g</sub>	773		778	778	777	809.0

<b>A<sub>2g</sub></b>	-		800	805	801	813.5
<b>A<sub>1g</sub></b>	875		884	884	881	845.3

### 4.1.3 - X-ray Photoelectron Spectroscopy

**Figure 6** displays the experimental and deconvoluted spectra of the core energy levels of the Ag 3*d* and W 4*f* peaks. The two component peaks at 367 and 374.6 eV can be attributed to the Ag<sup>0</sup> and Ag<sup>+</sup> states, respectively, while the peaks at 34.8 and 37.8 eV are satellites associated with the presence of the W<sup>6+</sup> and W<sup>5+</sup> states, respectively.[21]

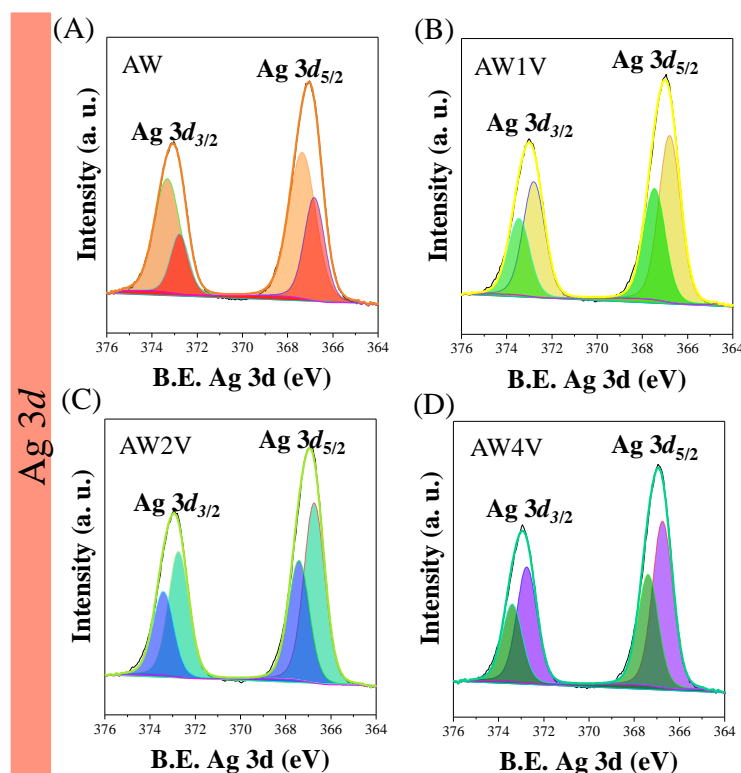
In the XPS spectra of O 1*s*, the identification of peaks attributed to oxygen atoms bonded to water and those bonded to the crystal lattice was performed by deconvolution of the O 1*s* spectrum into different Gaussian peaks (as illustrated in **Figure 7a-d**). The electronic density around the oxygen atoms not bonded to the crystal lattice is higher compared to those in the crystal lattice. As a result, the charge distribution on the oxygen atoms not bonded to the lattice is shifted towards these atoms, resulting in a lower nuclear potential and consequently a lower binding energy for these electrons.

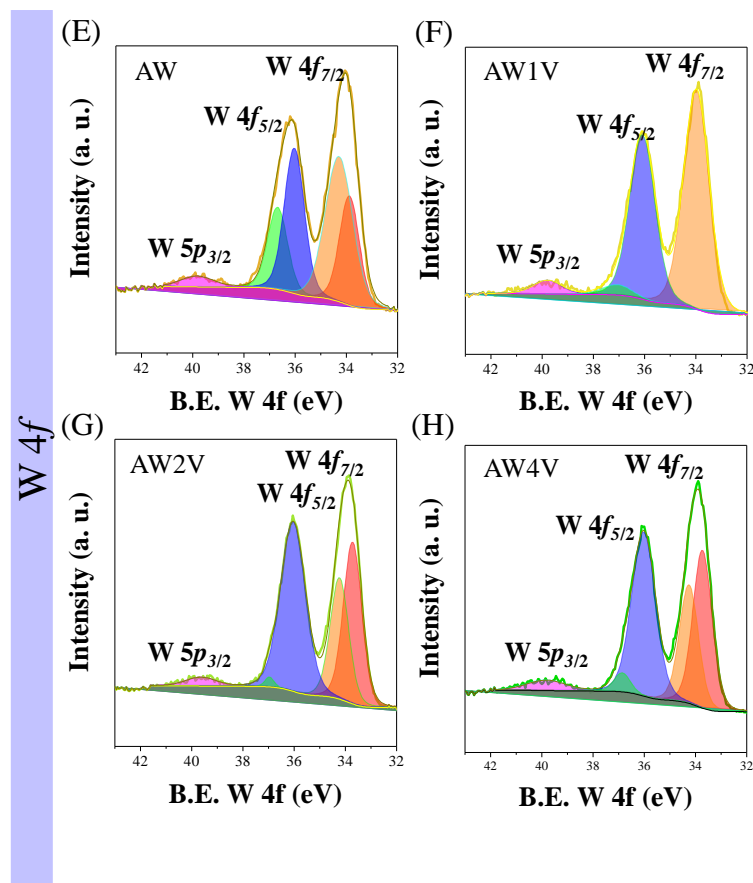
As a result, we can attribute the high-binding-energy peak at 532.07 eV and the low-binding-energy peak at 530.19 eV in the O 1*s* spectrum to different types of oxygen. The first peak, at 532.07 eV, represents oxygen atoms that are chemically bonded to the crystal structure (O<sub>L</sub>), while the second peak, at 530.19 eV, corresponds to oxygen atoms that are not directly bonded to the crystal structure. [21] More specifically, the peak at 532.07 eV in the O 1*s* spectrum encompasses various oxygen species, such as W–O, Ag–O, V–O, and O–OH bonds, with the latter associated with

water-adsorbed oxygens ( $O_W$ ). On the other hand, the peak at 530.19 eV is related to the W–O–W bond in the crystal structure ( $O_L$ ).

The O 1s peak in the 532.07 eV region may also include the contribution of oxygen vacancies ( $O_V$ ), suggesting that the binding energy of O 1s resulting from this bond is comparable to that of other oxygen atoms not directly bonded to the crystal lattice. This implies that both the oxygen atoms composing the vacancies and those not bonded to the crystal structure can contribute to this peak. Additionally, it is noteworthy that in the samples with the V-doped, a new component appears around 531 eV ( $O_{V-O}$ ). The deconvolution percentage varies between 8.73, 3.8, and 12.8%. Although the number of peaks does not increase with the doping concentration of V, this component indicates the existence of connections that may occur with V–O outside the crystal matrix, suggesting a substantial interaction between vanadium and oxygen in the structure.[69]

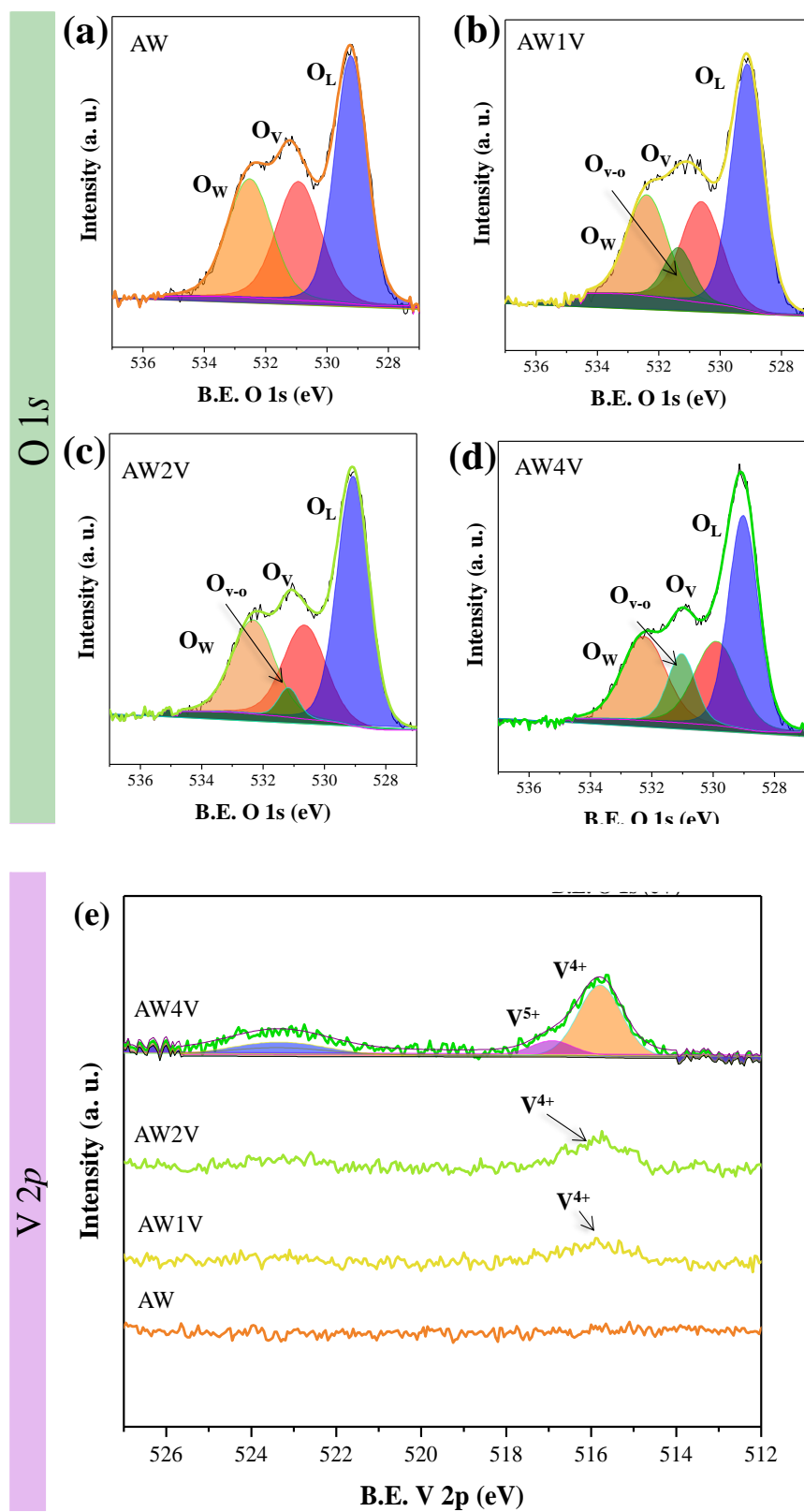
T



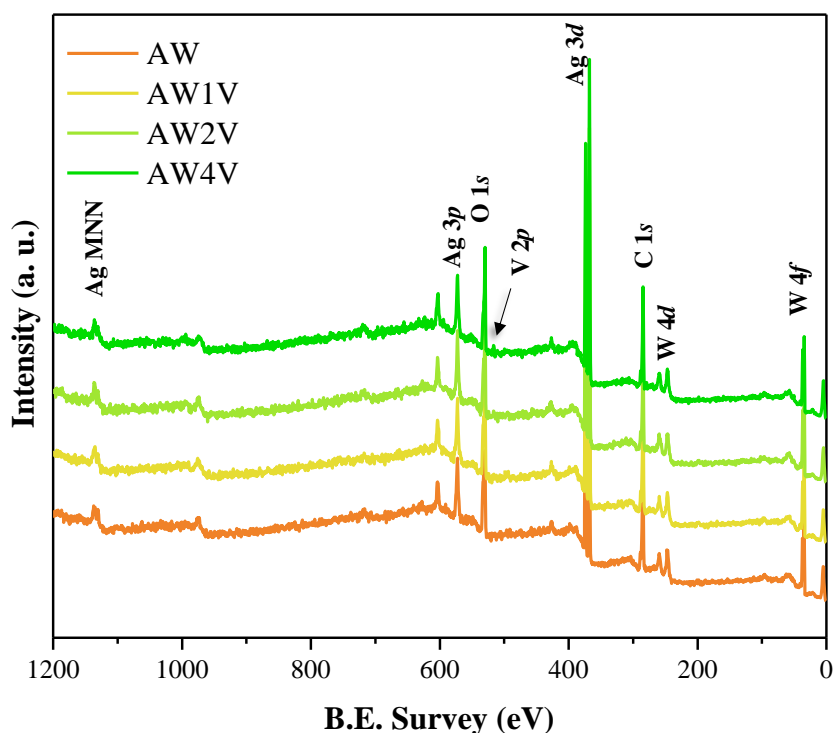


**Figure 6** - Core level XPS spectra of Ag 3d (a-d) and W 4f for the samples (e-h).

The XPS technique is widely used in investigating the surface of solid materials, becoming a valuable tool for exploring modifications resulting from doping. In this context, a high-resolution analysis was conducted at the V  $2p$  energy level (depicted in **Figure 7e**). The peaks observed around 516 and 518 eV were attributed to the  $V^{4+}$  and  $V^{5+}$  states, respectively. The presence of vanadium ions in the samples was confirmed by the increased peak in the XPS survey spectrum (**Figure 8**), which is expected to increase with doping concentration, as seen in Figure 7e in the V  $2p$  deconvolution. Furthermore, this doping may promote modifications in the oxianion network, facilitating the formation of bonds such as W–O– $V^{4+}$ . [70]



**Figure 7 - (a-d)** Core-level XPS spectra of O 1s and (e) V 2p for the samples.

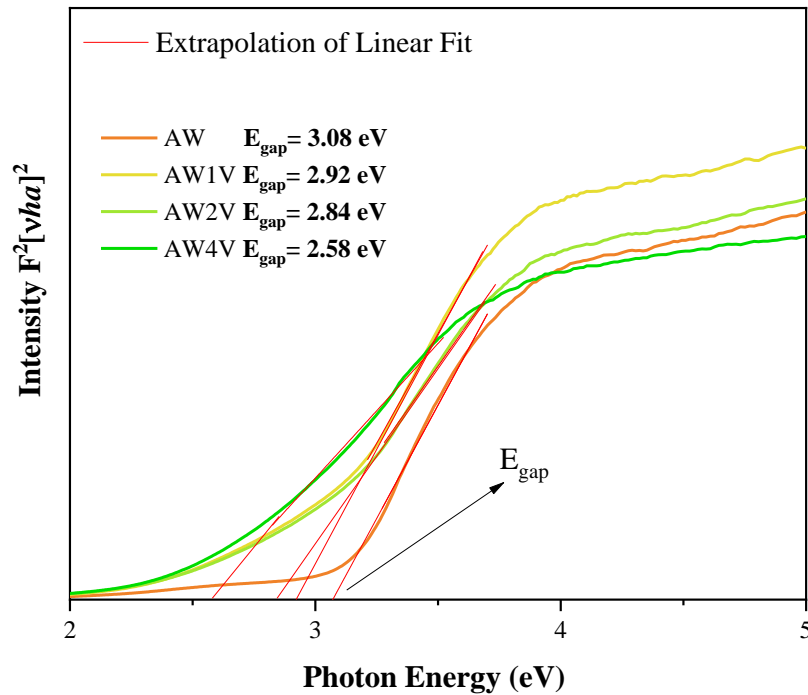


**Figure 8** - Survey XPS of the samples.

#### 4.1.4 - DRS

The energy band gap ( $E_{\text{gap}}$ ) values were determined from the UV-vis absorption spectra of DRS using the Wood-Tauc [6] and Kubelka-Munk [71] equations. In the AW sample, an absorption spectrum influenced by direct electronic transitions is observed, which arise when electrons return from minimum energy states in the conduction band to maximum energy states in the valence band at different points in the Brillouin zone (**Figure 9**). [72,73] Previous studies conducted by our group, employing the same synthesis method, indicated that the  $E_{\text{gap}}$  values for the AW were in the range of 3.08-3.18 eV [20,43,65], consistent with the value obtained in this work for the AW sample (3.08 eV). A reduction in the  $E_{\text{gap}}$  values was observed for the V-doped samples, with values of 2.92 (AW1V), 2.84 (AW2V), and

2.58 eV (AW4V). The analysis of the results suggests that as the concentration of  $[\text{VO}_4]$  clusters in the crystalline lattice of AW increases, there is a decrease in the  $E_{\text{gap}}$  values, due to the increase of excited electrons migrating from the valence band to the forbidden band of the semiconductor band gap.



**Figure 9** - Diffuse Reflectance Spectroscopy of the pure and V-doped sample.

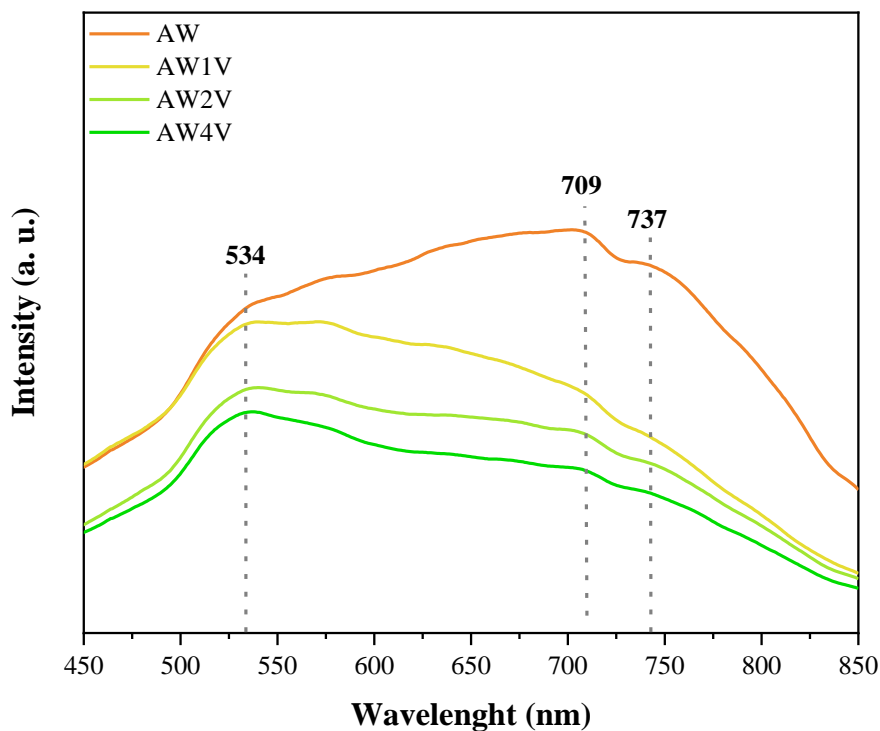
#### 4.1.5 - PL

Photoluminescence (PL) spectroscopy is a technique used to study the optical and electronic properties of materials. In this context, PL was employed to investigate how the substitution of  $[\text{WO}_6]$  clusters by  $[\text{VO}_4]$  affects the structure and electronic properties of the material. The AW sample exhibited a broad-band emission profile. This type of emission results from



a multipolar process, meaning that several intermediate states within the material's band gap are involved. [60,74] The observed emission is associated with structural defects in the material matrix.

This emission typically appears in the blue-green region of the spectrum, suggesting it is related to charge transfer in the  $[\text{WO}_6]$  clusters.[75] On the other hand, PL emissions in the red region of the spectrum indicate extrinsic defects, such as structural disorder and interfaces. Specifically, these defects are related to  $[\text{AgO}_x]$  clusters, where  $x$  can be 2, 4, 6, or 7. [42,65] The extrinsic defects induce a symmetry-breaking process in the material's crystalline structure. This breaking can lead to polarization due to charge transfer between ordered and disordered clusters, forming electron-hole pairs ( $e^-h^+$ ).



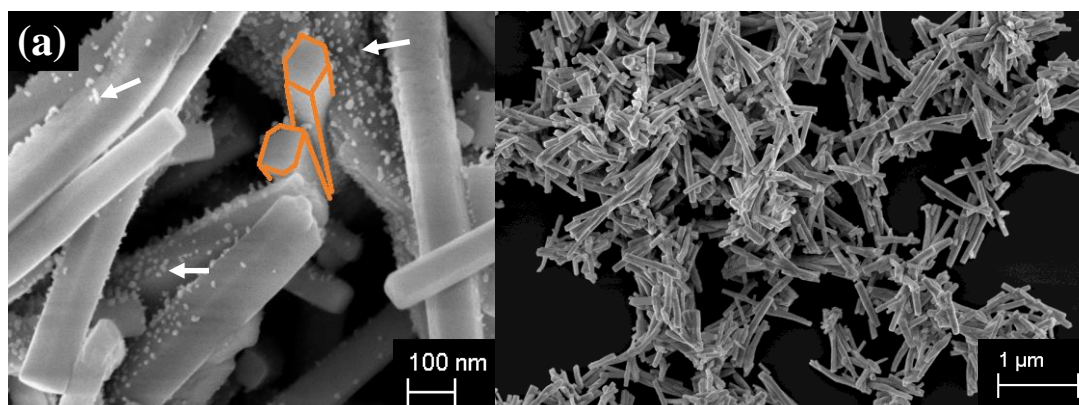
**Figure 10** - PL spectrum of the pure and V-doped sample.

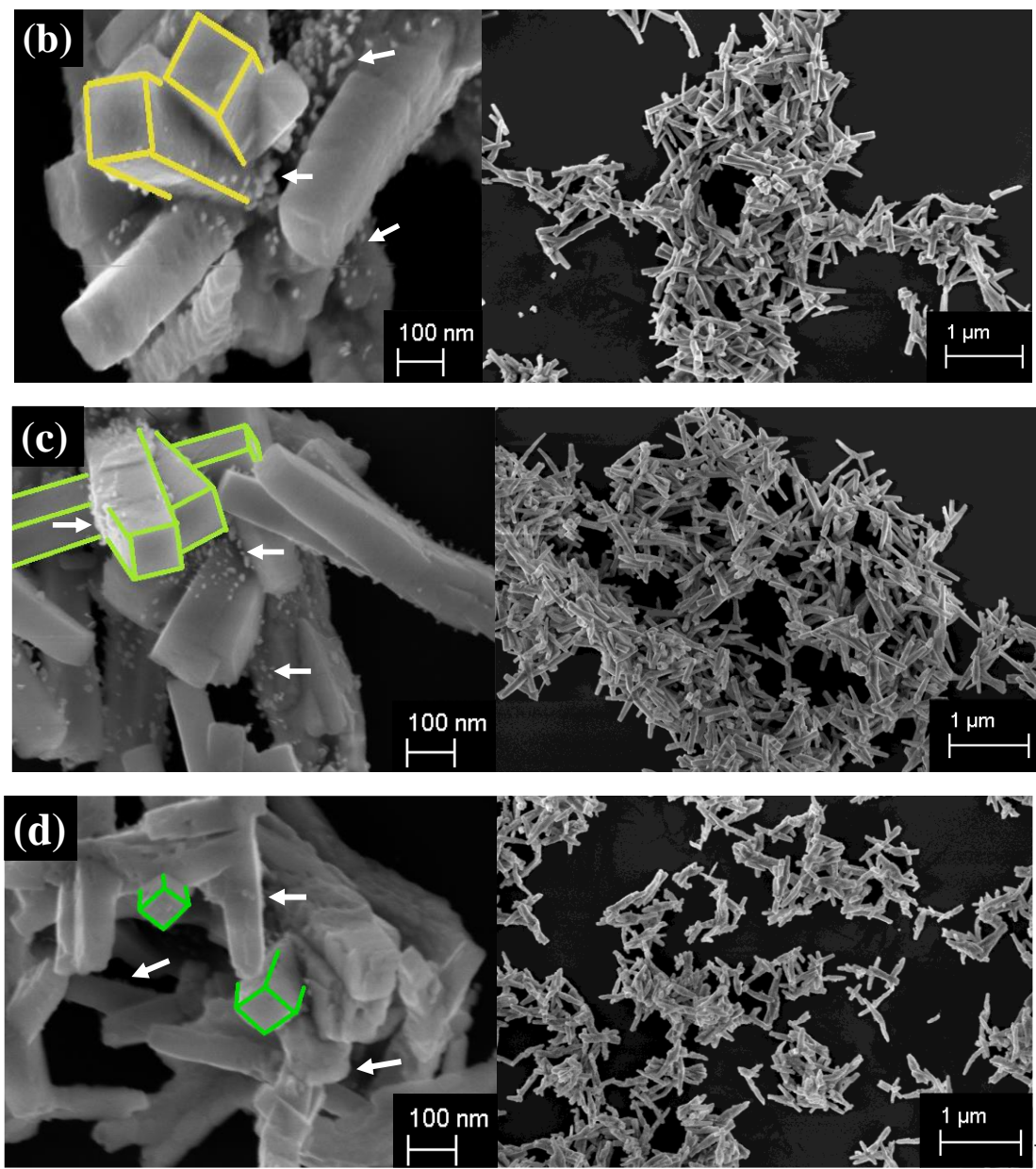
The **Figure 10** depicts the PL spectra of the samples conducted at room temperature with laser excitation of 355 nm, showing a broad band

profile between 500 and 750 nm. In the AW sample, a maximum PL emission peak is observed in the red region, at 709 nm, and a less intense shoulder in the blue-green region, at 534 nm. It is noticeable that, with the substitution of  $[\text{WO}_6]$  clusters by  $[\text{VO}_4]$ , there is a decrease in the intensity of PL emission across the broad band, especially in the red region. In contrast, in the blue-green region, the emission becomes more defined. This behavior can be associated with the results obtained in the XRD analyses, Raman spectroscopy, and DRS.

#### 4.1.6 - FE-SEM

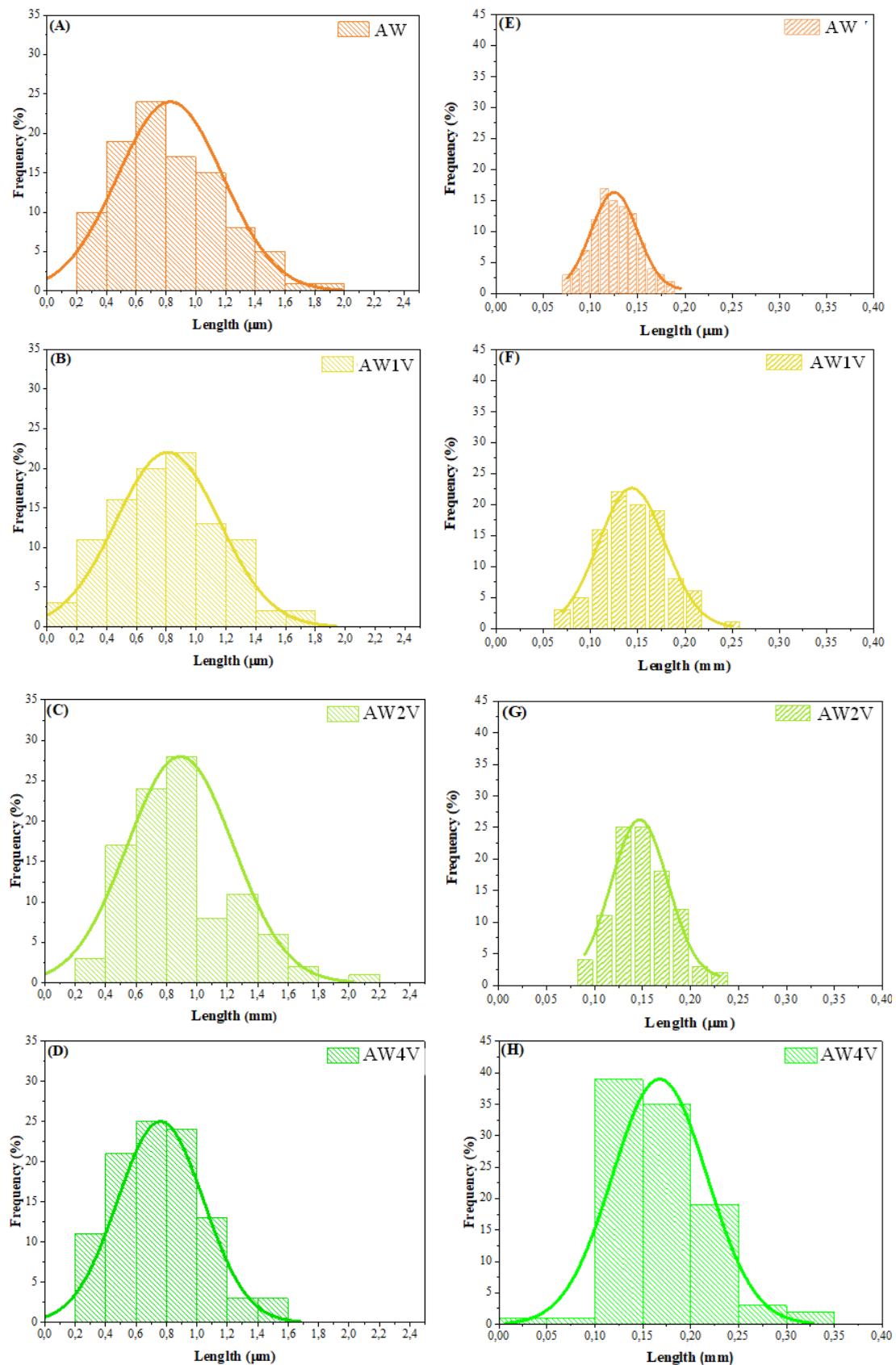
Through the analysis of FE-SEM images, it was possible to observe the morphologies and sizes of the samples. **Figure 11a** reveals that the pure AW sample presents elongated hexagonal rod morphology, with preferential growth along the (010) direction, as reported in previous research [8]. However, when doping with V occurs, a change in morphology to a parallelepiped shape is noted (**Figures 11b-d**).





**Figure 11** - FE-SEM images for (a) AW, (b) AW1V, (c) AW2V, and (d) AW4V.

This behavior may be related to structural distortions and charge density redistributions induced by the dopant, resulting in the exposure of different surfaces in the morphology [43]. The presence of  $[\text{VO}_4]$  clusters also impedes the growth of Ag nanoparticles on the surface of AW, increasing the samples' resistance to electron beam irradiation. The average length and width distribution of the samples were also analyzed, and the histograms are presented in **Figure 12**.



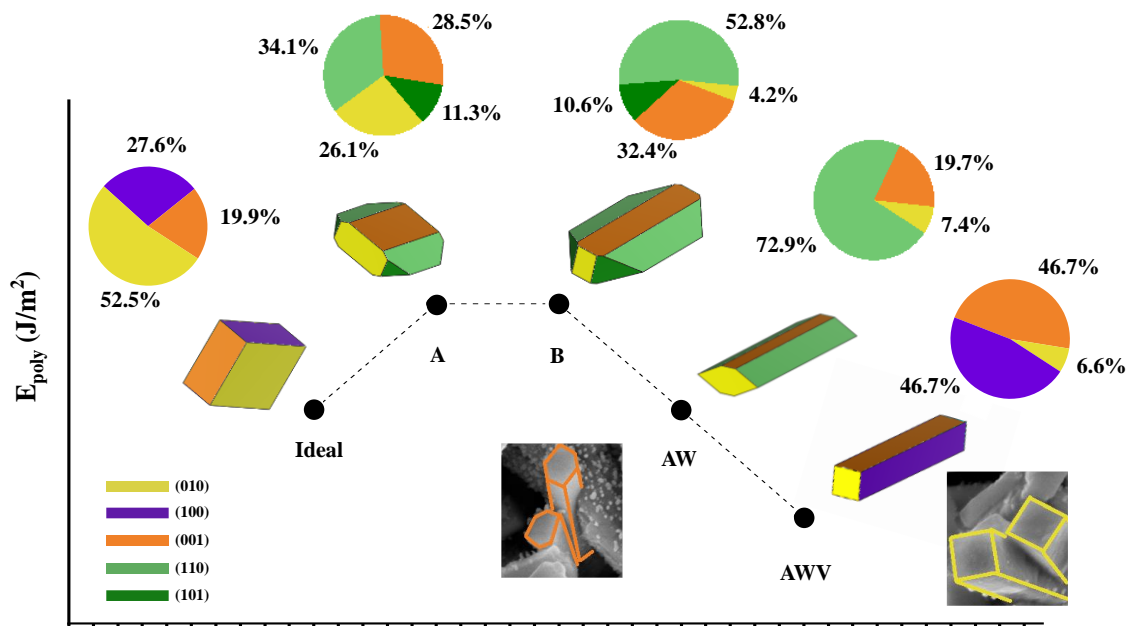
**Figure 12** - Average height (a-d) and width (e-h) distribution of AW and AWV samples.

In **Figure 12**, the average values of length and width were 0.82 and 0.12  $\mu\text{m}$ , 0.80 and 0.14  $\mu\text{m}$ , 0.79 and 0.15  $\mu\text{m}$ , and 0.76 and 0.16  $\mu\text{m}$  for the AW, AW1V, AW2V, and AW4V samples, respectively. It is observed that, besides the surface changes caused by V-doping, there is a reduction in length and an increase in the average width of the samples.

#### *4.1.7 - Theoretical Morphology*

To further understand the relationship between morphology and catalytic activity, it is important to investigate the active sites on the exposed surfaces at the atomic and molecular levels. In pursuit of this goal, we have published several works that combine experimental findings with first-principles calculations to gain deeper insights into the electronic, structural, and energetic properties that control the final morphology of as-synthesized materials.

This approach has allowed us to develop a 3D platform for morphology modulation, enabling rational design of new materials, from metals to metal oxides, for technological applications such as photocatalysts and antimicrobial materials. [56, 76-78] By building a reaction path along the synthesis progress and calculating the values of the polyhedron energy ( $E_{\text{poly}}$ ), we were able to identify the (010), (100), and (110) surfaces as the main components of AW morphology (**Figure 13**). This strategy not only helps to unravel the measured catalytic activity but also sheds light on the relationship between morphology and catalysis.



**Figure 13** - Schematic representation of the energy profile to obtain the as synthesized morphologies. The experimental morphologies are inserted for comparison purpose.

As can be seen in **Figure 13**, to achieve the experimental FE-SEM morphology (hexagonal rod) displayed by pure AW from the ideal morphology, we need to first increase the values of  $E_{\text{surf}}$  of the (010), (100), and (110) surfaces, and also decrease the value of  $E_{\text{surf}}$  of the (001) and (101) surfaces to reach morphology A. Next, to reach morphology B from A, we need to increase the values of  $E_{\text{surf}}$  for the (010) and (110) surfaces. To connect morphology B with the experimental morphology obtained for V-doped samples, an increase in the values of the  $E_{\text{surf}}$  of the (010) and (110) surfaces, with a concomitant decrease in the values of  $E_{\text{surf}}$  of the (101) surface is needed. The hexagonal rod of AW is mainly composed of the surface (100) with a contribution of 72.9%, while the (001) and (010) surfaces have contributions of 19.7% and 7.4%, respectively. When AW is



doped with V, changes in the experimental morphology are observed, resulting in a cobblestone with the (100) and (001) surfaces exposed in equal proportion (46.7% each), while the (010) surface displays a lower proportion (6.6%).

Thus, the presence of  $[\text{VO}_4]$  clusters promotes the stabilization of the (100) surface and the destabilization of the (101) surface. This morphology has a lower  $E_{\text{poly}}$  than the ideal AW morphology (**Table 4**), revealing that the high activity of the V-doped catalysts is based on the presence of the (100) surface.

**Table 4** - Comparison between the values of Surface energy ( $E_{\text{surf}}$ , eV), contribution of surface area by total area ( $C_i$ , %) and Polyhedron energy ( $E_{\text{polyhedron}}$ , eV) for each AW and AWV morphology.

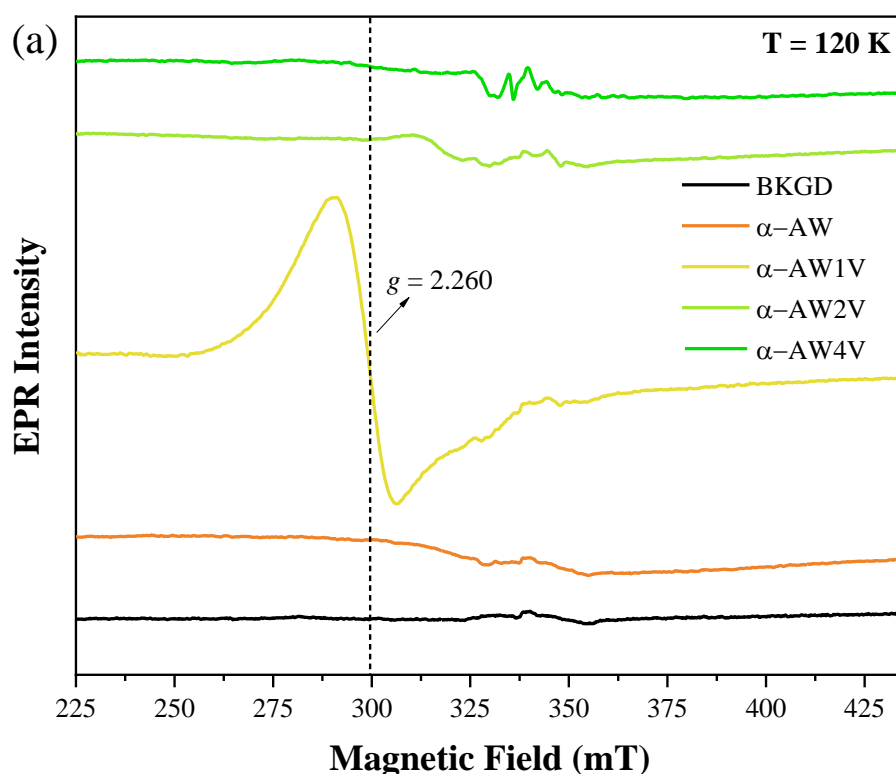
Surface	AW Ideal	A	B	AW rod-like	AW cobblestone-like
[010]	0.20(52.5)	0.60(16.4)	1.11(4.23)	1.41(7.35)	1.41(6.62)
[100]	0.38(27.6)	0.70(0.00)	0.70(0.00)	0.70(0.00)	0.20(46.7)
[001]	0.53(19.9)	0.20(37.6)	0.20(32.4)	0.20(19.7)	0.20(46.7)
[110]	0.65(0.00)	0.73(4.91)	0.85(10.6)	2.00(0.00)	2.00(0.00)
[101]	0.68(0.00)	0.33(41.1)	0.27(52.7)	0.23(72.9)	0.40(0.00)
[011]	0.83(0.00)	0.83(0.00)	0.83(0.00)	0.83(0.00)	0.83(0.00)
$E_{\text{polyhedron}}$	<b>0.31</b>	<b>0.34</b>	<b>0.34</b>	<b>0.31</b>	<b>0.28</b>

#### 4.1.8 - EPR

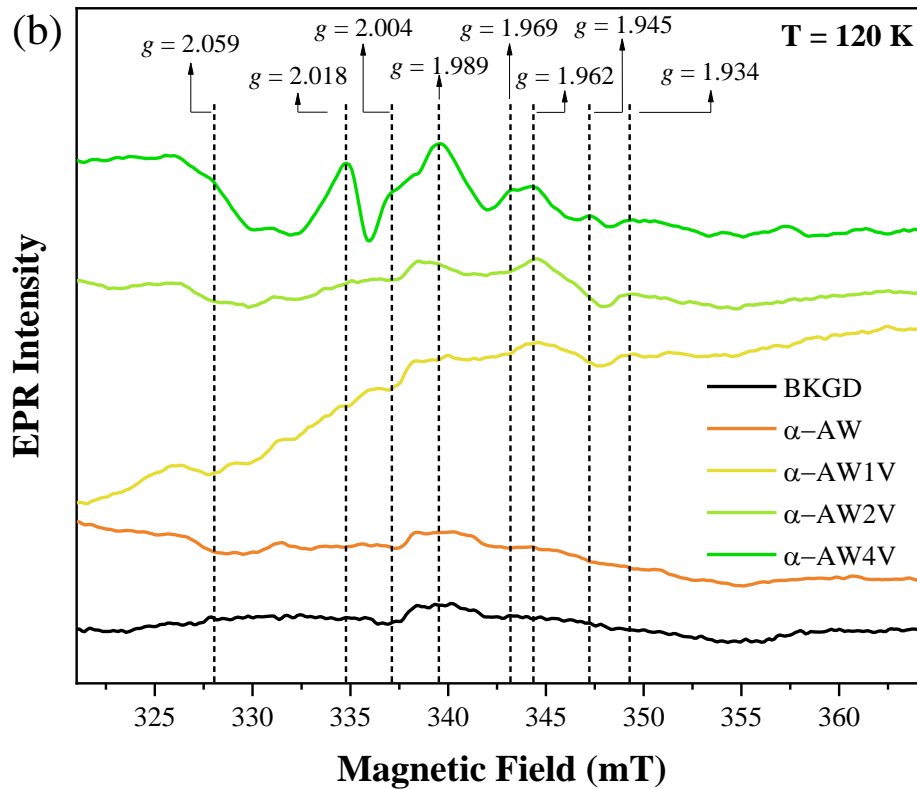
EPR spectroscopy was performed to assess the presence of paramagnetic species in the samples. Chemically pure and stoichiometric V-doped AW is not expected to exhibit any EPR signal, as  $\text{Ag}^+$  ( $[\text{Kr}] 3d^{10}$ ),  $\text{W}^{6+}$  ( $[\text{Xe}] 4f^{14}$ ), and  $\text{V}^{5+}$  ( $[\text{Ar}]$ ) cations do not have unpaired electrons and are therefore EPR silent. However, as previously discussed, the incorporation of V into the lattice of AW microcrystals generates intrinsic defects, local

distortions, and redistribution of charge densities, which may favor the formation of EPR-detectable paramagnetic centers, such as oxygen vacancies,  $W^{5+}$  ( $[\text{Xe}] 4f^{14} 5d^1$ ), and  $V^{4+}$  ( $[\text{Ar}] 3d^1$ ) cations, among other species.

**Figure 14** shows the EPR spectra of undoped and V-doped AW catalysts. Interestingly, a sharp signal is observed at  $g = 2.260$  for the AW1V sample but is absent for more highly doped or undoped samples (**Figure 14a**). Furthermore, a group of signals with  $g$  values ranging from 2.059 to 1.934 is distinctly detected for the AW4V sample, partially detected for both AW2V and AW1V samples, and undetected for the undoped AW sample (**Figure 14b**).



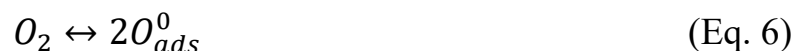




**Figure 14** - X-band EPR spectra of the undoped (AW) and V-doped (AW1V, AW2V, and AW4V) samples recorded at 120 K. (a) Magnetic field swept from 225 to 435 mT. (b) Magnetic field swept from 320 to 365 mT. The background spectrum (BKGD) was obtained by measuring an empty samples tube.

It is well-known that superficial oxygen vacancies and intrinsic defects are ubiquitous in semiconductor metal oxides. [79] When the oxygen concentration in the environment is lower than the equilibrium concentration, lattice oxygen atoms can desorb to form  $O_2$ . The electrical conductivity of semiconductors presents a power-law dependence on the partial pressure of environmental gases. Previous works indicate that oxygen exchange involves different species, but it occurs through neutral oxygen. Wolkenstein's theory of chemisorption describes the semiconductors' electrical response within the ionosorption framework, in which oxygen is adsorbed/desorbed neutrally and can always be ionosorbed as doubly

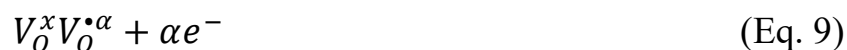
charged. [80] When the oxygen concentration in the environment is lower than the equilibrium concentration, lattice oxygen atoms can desorb to form  $O_2$ . [81] Wolkenstein's theory of chemisorption can describe the electrical response of semiconductors within the ionosorption species framework according to the following reaction:



Certainly, the oxygen exchange equilibrium between  $O_{ads}^0$  on AW surface and vacancies the gas phase is regularly written as [74]



where  $V_O^x$  is a neutral oxygen vacancy in equilibrium with  $V_O^\bullet$  or  $V_O^{\bullet\bullet}$  having one or two electrons ( $a = 1$  or  $2$  respectively), that ionizes according to:



yielding a cationic oxygen vacancy ( $V_O^{\bullet\alpha}$  in the Kröger-Vink notation), which is paramagnetic, and an electron that is typically transferred to the conduction band of the semiconductor. [75] The nature of defects in AW has already been studied by our research group. [76,77] According to both experimental and theoretical studies, the formation of oxygen vacancies is favored in either undoped or V-doped AW samples. Considering the reactions introduced above and, given that the lowest energetic level of the conduction band of V-doped AW microcrystals are V  $3d$  orbitals, electrons could transfer from  $V_O^x$  into EPR-silent  $V^{5+}$  cations yielding paramagnetic

$V^{4+}$  and  $V_O^\bullet$  species. In addition to oxygen vacancies, anionic silver vacancies ( $V_{Ag}^\ominus$  in the Kröger-Vink notation) are also favored in AW. In fact, the defect profile of AW microcrystals consists mainly of Ag—O vacancy complexes ( $V_{Ag-O}$ ), which are formed by two cationic oxygen vacancies surrounding one anionic silver vacancy. [76,77]

In light of the above discussion, the observed EPR signals can be assigned to specific paramagnetic species. It is worth mentioning that trapped electrons in cationic oxygen vacancies ( $V_O^\bullet$ ) exhibit an EPR response similar to that of free electrons [78]. Therefore,  $V_O^\bullet$  are characterized by a pronounced resonance at *ca.*  $g = 2.003$ , as it has been widely described in the scientific literature for different semiconductor metal oxides. [75, 78-80]

However, it has also been reported that oxygen vacancies in  $WO_{(3-x)}$  can resonate at much higher  $g$  values. QIAN et al. [81] and Shen et al. [82] measured a sharp EPR signal at  $g = 2.28$  in a set of  $WO_{(3-x)}$  samples. The authors reported that the intensity of the signal increases as  $x$  becomes higher, i.e., as the concentration of oxygen vacancies increases. Furthermore, the signal was not observed in a stoichiometric  $WO_3$  sample, and hence the authors ascribed it to the oxygen vacancies present in  $WO_{(3-x)}$ . DI VALENTIN AND PACCHIONI [83] demonstrated by theoretical calculations that most of the electronic density due to excess electrons from an oxygen vacancy is located at the  $V_O$  void in  $WO_{(3-x)}$ .

It is worth stressing that  $V_O$  is a neutral oxygen vacancy, which means that the two electrons that belonged to the missing  $O^{2-}$  anion remain in the defect void and are not transferred into the conduction band of the semiconductor. QIAN et al. claimed that the shift in the  $g$  value from *ca.* 2.003 to 2.28 is due to the presence of these two charge centers (unpaired electrons) trapped in neutral oxygen vacancies. The EPR signal found at  $g = 2.260$  for the AW1V microcrystals is similar in both shape and  $g$  value to the

signal ascribed to oxygen vacancies in  $\text{WO}_{(3-x)}$ . As it was previously mentioned, the most common defect in AW microcrystals is Ag—O vacancy complexes ( $V_{\text{Ag-O}}$ ), which are formed by two cationic oxygen vacancies surrounding one anionic silver vacancy. In this case, more than one unpaired electron, i.e., negatively charged centers are present in the defect complex.

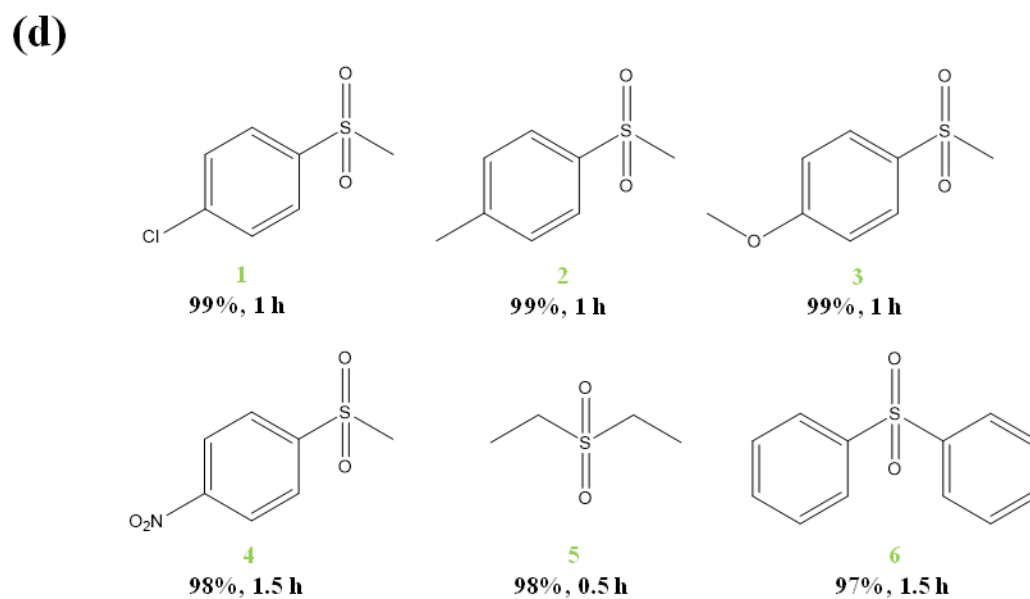
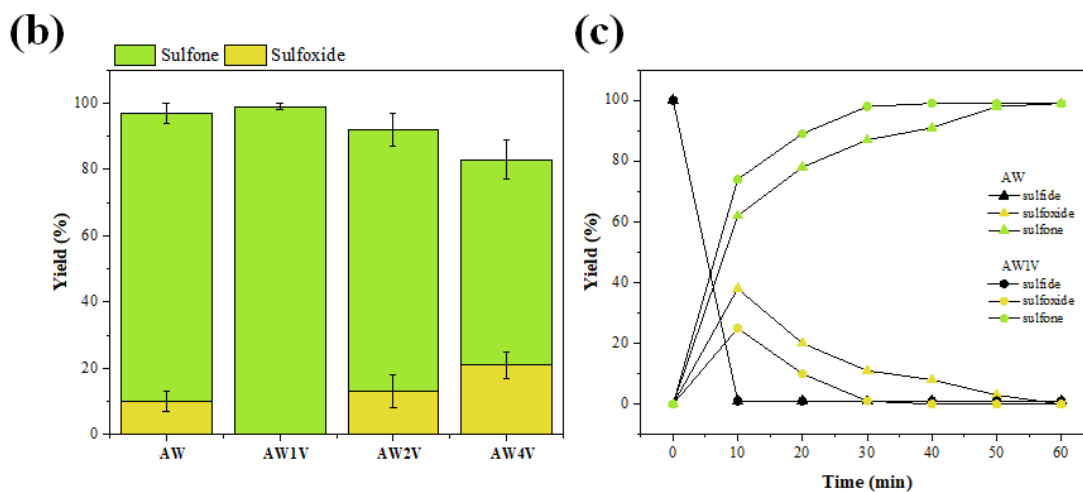
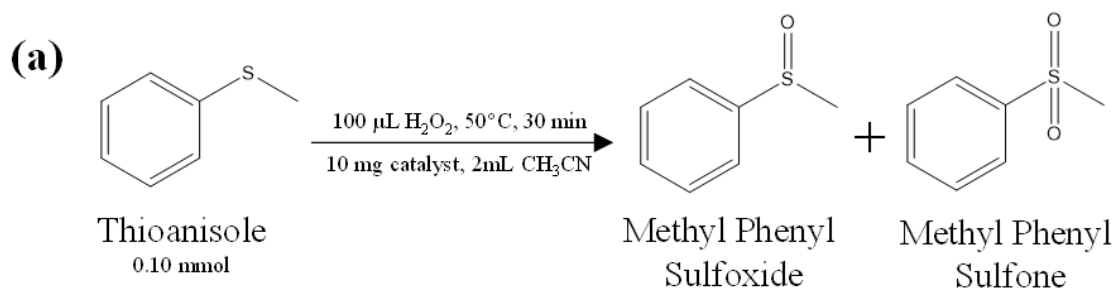
Therefore, the EPR signal observed at  $g = 2.260$  for the AW1V sample could be assigned reasonably to Ag—O vacancy complexes. Nevertheless, the question about why such a signal is not observed for more doped or undoped samples naturally arises. Interestingly, the change in the morphology of the AW samples as the V content increases might shed light on this question. For the AW sample, the surfaces (010), (001), and (110) are stabilized, while for the AW1V sample, surfaces (010), (001), and (100) are stabilized. Surfaces (010) and (001) are common for both morphologies, the crucial difference being found in surfaces (110) and (100). According to MACEDO et al. [20], surface (100) ends in undercoordinated clusters  $[\text{AgO}_5.2\text{V}_\text{O}]$  and  $[\text{WO}_4.2\text{V}_\text{O}]$ , while surface (110) ends in undercoordinated clusters  $[\text{AgO}_3.4\text{V}_\text{O}]$ ,  $[\text{AgO}_2.2\text{V}_\text{O}]$ , and  $[\text{WO}_4.2\text{V}_\text{O}]$ . Therefore, the EPR signal observed at  $g = 2.260$  might be most likely due to  $[\text{AgO}_5.2\text{V}_\text{O}]$  clusters, which are only predominant in the AW1V sample.

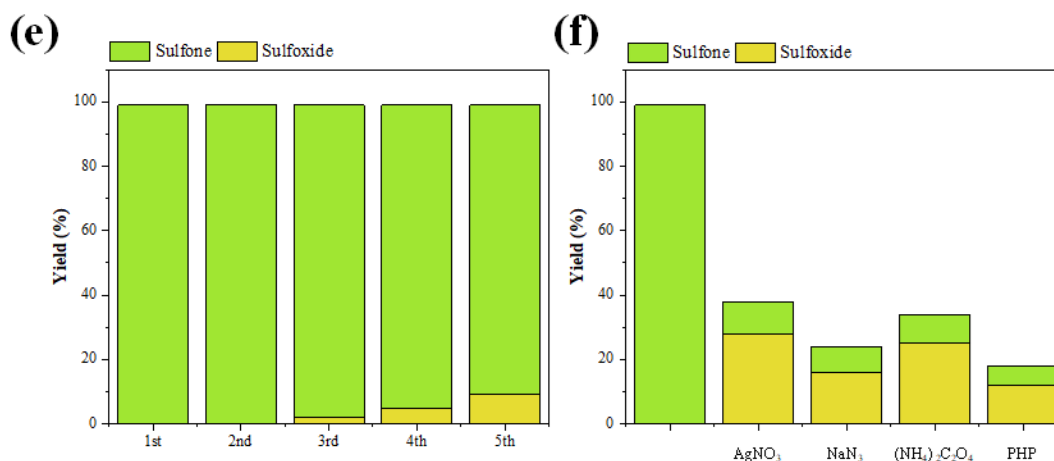
The  $g$  values in the range of values from 1.934 to 2.059, different of those observed for the AW4V sample, are characteristic of  $\text{V}^{4+}$  ( $[\text{Ar}] 3d^1$ ,  $S = 1/2$ ,  $I = 7/2$ ) species. [84, 85] These signals arise due to the coupling of the  $\text{V}^{4+} 3d^1$  single electron ( $S = 1/2$ ) with its nucleus ( $I = 7/2$ ). According to the micro-Raman and PL measurements, the substitution of  $[\text{WO}_6]$  for  $[\text{VO}_4]$  clusters provoke a short-range structural ordering that manifests as a change from cationic oxygen vacancies into doubly-ionized oxygen vacancies ( $V_\text{O}^\bullet \rightarrow V_\text{O}^{\bullet\bullet}$ ). In V-doped AW samples, the formation of a doubly-ionized oxygen vacancy implies the transfer of the unpaired electron from a cationic oxygen vacancy into V  $3d$  orbitals (bottom of the conduction

band). Double-ionized oxygen vacancies are EPR-silent, which explains the absence in the AW2V and AW4V samples of the signal ascribed to cationic oxygen vacancies ( $g = 2.260$ ). However, paramagnetic  $V^{4+}$  species are indeed detected. Thus, the increase in the intensity of the  $V^{4+}$  signals as the doping level increases (**Figure 14b**) is in excellent agreement with the hypothesis that short-range structural ordering takes place in the V-doped samples.

#### *4.1.9 - Catalytic*

The changes observed in the structural, morphological, and electronic properties of V-doped AW samples were analyzed for the oxidation of thioanisole, which served as the reaction model (**Figure 15a**). The intermediate and final products of the reaction are methyl phenyl sulfoxide and methyl phenyl sulfone, respectively. For the reaction to occur, various oxidizing agents have been used, including tert-butyl hydroperoxide, cumene hydroperoxide, and iodosobenzene. [86, 87] However, in this work, a more environmentally friendly oxidant,  $H_2O_2$ , was chosen. First, the solvent conditions, including the amount of oxidant, temperature, time, and catalyst mass, were optimized.





**Figure 15** - (a) Thionisole oxidation reaction scheme; (b) conversion and selectivity of different catalysts to thioanisole oxidation; (c) thionisole oxidation kinetics for AW and AW1V samples; (d) catalytic scope using AW1V catalyst; (e) 10-fold scaled catalytic recycle for the oxidation reaction using AW1V catalyst; (f) scavenger tests in the oxidation reaction using AW1V catalyst.

**Figure 15b** shows the results of the optimized conditions for the synthesized samples using acetonitrile as a solvent (2 mL), with 10 mg of catalyst, 100  $\mu$ L of H<sub>2</sub>O<sub>2</sub>, 50°C, and 30 min. It can be observed that the AW samples had a conversion of >99%, with 87% selectivity for the sulfone. On the other hand, the AW1V sample showed a conversion of >99% with total selectivity for the sulfone. However, samples AW2V and AW4V showed a drop in conversion rates to values of 93% and 85%, with selectivity of 79% and 62% for sulfones, respectively. Therefore, it is observed that low concentrations of V-doping in the crystal lattice of AW increase the conversion and selectivity to the final product in shorter times. Samples with lower concentrations of V doping (0.5 and 0.25% mol %) were also synthesized, but the AW1V sample still showed the best conversion and selectivity results.

As observed by RADKO et al. [37], the doping process with small concentrations of V generates new oxidation sites on the catalyst

surface, enhancing its efficiency. The alteration in morphology and, consequently, in stabilized surfaces modifies the active sites for the reaction to occur. As discussed in the EPR results, the (100) surface, with undercoordinated clusters [AgO<sub>5</sub>.2VO], is stabilized in the AW1V sample. Therefore, it can be inferred that the [AgO<sub>5</sub>.2VO] clusters most likely represent the highly active sites responsible for the observed increase in oxidation processes on the catalyst surface.

A kinetic analysis of thioanisole oxidation products was performed for samples AW and AW1V (**Figure 15c**). As mentioned in the literature, the first oxidation step for sulfoxide formation is easier, while the second step for sulfone formation is more challenging. Within the first 10 minutes of reaction, the AW catalyst achieved a conversion of >99%, with a selectivity of 62% for the sulfone, while the AW1V catalyst achieved the same conversion with a selectivity of 74% for the sulfone. After 30 minutes of reaction, the AW catalyst demonstrated a selectivity of 87% for the sulfone, while the AW1V catalyst reached a selectivity of >99% for the sulfone.

Furthermore, a catalytic scope analysis was conducted (**Figure 15d**), revealing high chemoselectivity for the formation of sulfones in all cases. Diethyl sulfide was rapidly converted into its sulfone in just 0.5 hours, while diphenyl sulfide required three times longer, approximately 1.5 hours. For all *p*-substituted thioanisoles (-Cl, -CH<sub>3</sub>, -OCH<sub>3</sub>, and -NO<sub>2</sub>), conversion to the respective sulfones was achieved in less than one hour, indicating the catalyst's ability to oxidize a variety of substrates based on different sulfides. Following the substrate scope analysis, a study on catalyst recycling was conducted (**Figure 15e**). The AW1V catalyst maintained its high catalytic activity even after three cycles of use, achieving a 100% conversion rate in each cycle. In the fourth and fifth cycles, the conversion to the corresponding product was 95% and 91%, respectively.



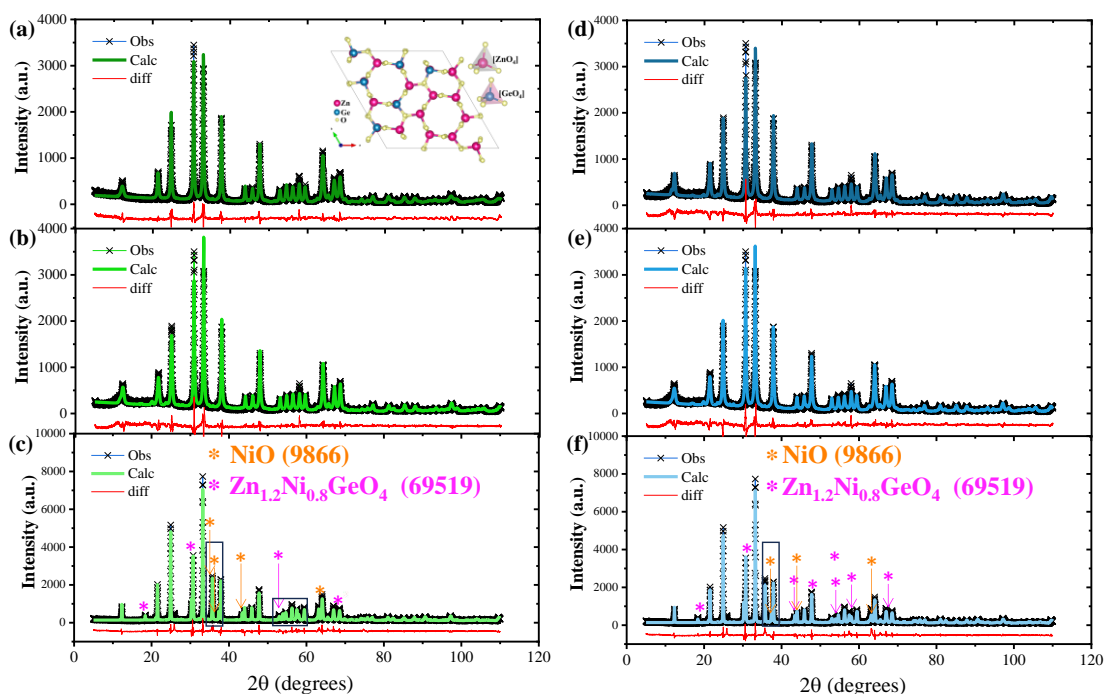
The activity of the ionic species ( $\text{Ag}^+$ ), ( $\text{VO}_4^{3-}$ ), and ( $\text{WO}_4^{2-}$ ) in the oxidation of sulfides was analyzed, and results similar to those of pure  $\text{H}_2\text{O}_2$  were obtained (total conversion <30%), showing that even if these species leach into the solution, they are not active in this reaction. The oxidation mechanism was studied by adding equimolar amounts of scavengers for  $e^-$ ,  $h^+$ ,  $\bullet\text{OH}$  radicals, and  $^1\text{O}_2$  to the reaction (**Figure 15f**). A significant reduction in catalytic efficiency was observed for all scavengers, indicating that these species are directly involved in the oxidation process.

Therefore, the  $e^-h^+$  pairs generated by thermo-excitation interact with  $\text{O}_2$  and  $\text{H}_2\text{O}_2$  in the reaction medium, producing the  $\bullet\text{OH}$  radical and  $^1\text{O}_2$ . [89,90] These species act as extremely potent oxidants, capable of easily oxidizing sulfides to sulfones by creating reaction pathways with lower activation barriers. [91] These results indicate the occurrence of electron transfer reactions from short-lived species and show similarities with the photoinduced reactions of the special photocatalytic pair, suggesting that this state can serve as a reference system for studying excited-state structures and investigating catalytic reactions.

## 4.2 - Ni-doped ZGO

### 4.2.1 - XRD and Rietveld

XRD patterns of ZGO and ZGO1 powders (with and without temperature treatment) are shown in **Figure 16**. All Bragg peaks are indexed to a rhombohedral structure with the R-3 space group, card number 68382 in the Inorganic Crystal Structure Database (ICSD) reveals the lattice parameters as  $a=b=14.2841 \text{ \AA}$  and  $c=9.5471 \text{ \AA}$ . Notably, no secondary phase was detected, confirming the high purity of the samples.



**Figure 16** - XRD and Rietveld refinements of the samples. (a) ZGO; (b) ZGO1; (c) ZGO16; (d) ZGO-1000; (e) ZGO1-1000, and (f) ZGO16-1000.

The crystalline structure of ZGO comprises corner-sharing tetrahedral  $[\text{ZnO}_4]$  and  $[\text{GeO}_4]$  clusters, bridged by oxygen anions, arranged in a pattern parallel to the  $c$ -axis. [97,98,99, 118] Conversely, the ZGO16

samples are composed of three different phases: the rhombohedral structure of ZGO, NiO with a cubic structure and Fm-3m space group (ICSD 9866), and the  $Zn_{1.2}Ni_{0.8}GeO_4$  with a cubic structure and Fd-3m space group (ICSD 69519). Notably, a lower range of  $x=0.16\%$   $Ni^{2+}$ -doping was synthesized, and the blue color was maintained.

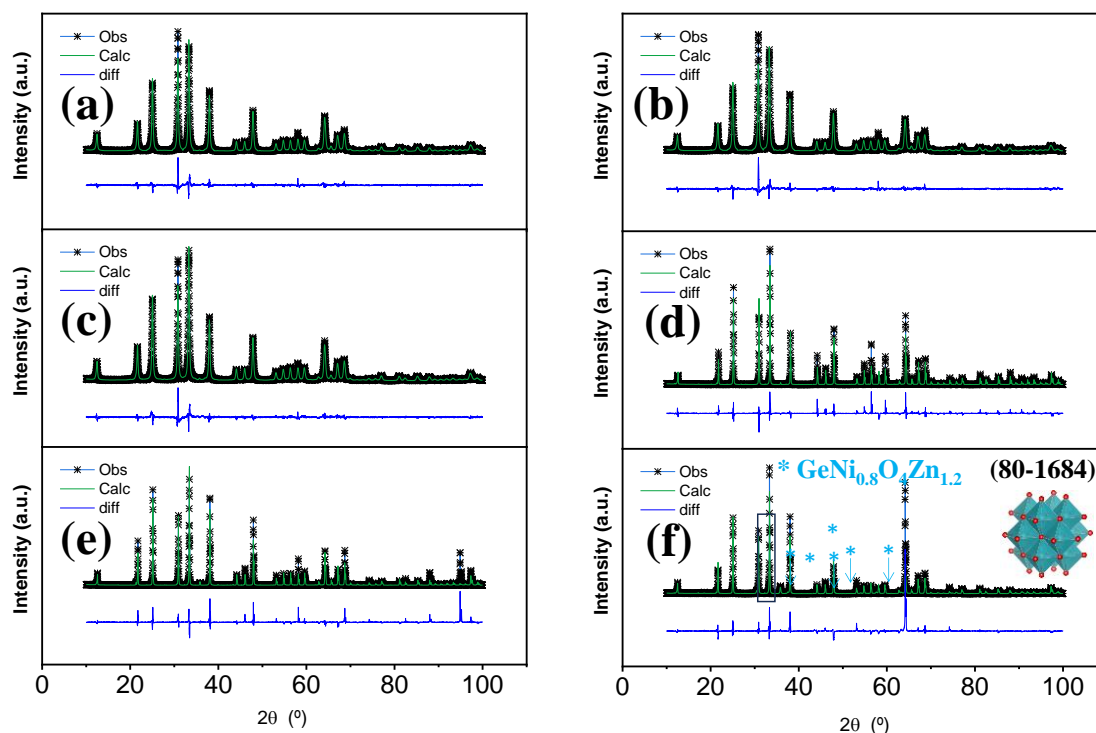
Analyzing the most intense peak (410) of the  $Zn_2GeO_4$  phase in all samples, a shift to higher  $2\theta$  values is observed, indicating a contraction of the material's crystal lattice when doped with  $Ni^{2+}$ . There is also a variation in the peak's total width values at half maximum (FWHM) (410). The FWHM values for the samples without thermal treatment are  $0.434^\circ$ ,  $0.432^\circ$ , and  $0.374^\circ$  for ZGO, ZGO1, and ZGO16, respectively. This reduction in FWHM values suggests an increase in long-range structural ordering. However, when compared to the thermally treated samples, it is observed that the FWHM values are  $0.143^\circ$ ,  $0.149^\circ$ , and  $0.180^\circ$  for ZGO-1000, ZGO1-1000, and ZGO16-1000, respectively. Therefore,  $Ni^{2+}$  doping increases long-range structural ordering at low temperatures, but at high temperatures, this process results in a more disordered system with the appearance of new defects.

Rietveld refinements of the samples were conducted to understand better the structural modifications provoked by the  $Ni^{2+}$  doping process and thermal treatment (**Table 5**). For all samples, the refinement quality, as indicated by the  $\chi^2$  values, suggests that  $Ni^{2+}$  substitution occurs at the  $Zn^{2+}$  sites. For samples without thermal treatment,  $Ni^{2+}$  doping reduces the lattice parameters and, consequently, decreases the volume of the crystal unit cell of ZGO. In contrast, the opposite effect is observed for thermally treated samples. These results are consistent with the peak shift (410) observed in the XRD analysis. The compositional analysis of ZGO16 renders the pure ZGO (~89%), NiO (~3%), and  $Zn_{1.2}Ni_{0.8}GeO_4$  (~8%).

**Table 5** - Structural results obtained from Rietveld refinements and theoretical simulations.

Samples		Lattice parameters (Å)		Cell Volume (Å <sup>3</sup> )	$\chi^2$	Phase Fraction%
		a=b	c			
ZGO Theo	Zn <sub>2</sub> GeO <sub>4</sub>	14.401	9.631	1729.645		
ZGO	Zn <sub>2</sub> GeO <sub>4</sub>	14.285	9.571	1691.587	3.64	100
ZGO-1	Zn <sub>2</sub> GeO <sub>4</sub>	14.242	9.540	1675.985	3.80	100
ZGO-16	Zn <sub>2</sub> GeO <sub>4</sub>	14.255	9.543	1679.678		88.6
	NiO	4.168	4.168	72.434	4.44	3.10
ZGO-1000	Zn <sub>2</sub> GeO <sub>4</sub>	8.330	8.330	578.130		8.30
	Zn <sub>2</sub> GeO <sub>4</sub>	14.273	9.560	1686.846	3.69	100
ZGO-1-1000	Zn <sub>2</sub> GeO <sub>4</sub>	14.280	9.555	1687.459		100
ZGO-16-1000	Zn <sub>2</sub> GeO <sub>4</sub>	14.256	9.544	1680.000		89.0
	NiO	4.167	4.167	72.394	4.47	2.40
	Zn <sub>0.2</sub> Ni <sub>0.8</sub> GeO <sub>4</sub>	8.332	8.332	578.458		8.60

Both the diffractograms and the compositional analysis by Rietveld of Ni-doped ZGO samples with intermediate compositions of 2, 4, and 8% are shown in **Figure 17** and **Table 6**.



**Figure 17** - XRD and Rietveld refinements of the samples. (a) ZGO2; (b) ZGO2-1000; (c) ZGO 4; (d) ZGO4-1000; (e) ZGO8; and ZGO8-1000.

In **Table 6** for untreated samples, it is not observed the formation of secondary phases, in contrast to thermally treated samples, which only show secondary phase at 8% ( $\text{Zn}_{1.2}\text{Ni}_{0.8}\text{GeO}_4$ ). Moreover, the ZGO structure was optimized, and the calculated equilibrium lattice parameters agree with the experimental values, as reported in **Table 5**.

**Table 6** - Structural results obtained from Rietveld refinements.

Samples	Lattice parameters (Å)		Cell Volume (Å <sup>3</sup> )	$\chi^2$	Phase Fraction%	
	a=b	c				
ZGO Theo	$\text{Zn}_2\text{GeO}_4$	14.401	9.631	1729.645		
ZGO – 2	$\text{Zn}_2\text{GeO}_4$	14.238	9.533	1673.890	2.23	100
ZGO – 4	$\text{Zn}_2\text{GeO}_4$	14.243	9.534	1675.317	2.39	100
ZGO – 8	$\text{Zn}_2\text{GeO}_4$	14.246	9.535	1675.908	2.23	100
ZGO-2-1000	$\text{Zn}_2\text{GeO}_4$	14.227	9.525	1669.876	5.16	100
ZGO-4-1000	$\text{Zn}_2\text{GeO}_4$	14.229	9.524	1670.279	5.23	100
ZGO-8-1000	$\text{Zn}_2\text{GeO}_4$	14.230	9.525	1670.469	4.12	95.65
	$\text{Zn}_{0.2}\text{Ni}_{0.8}\text{GeO}_4$	8.322	8.322	576.368		4.35

The DFT values differ by less than 1% from the experimental values (0.8% and 0.6% for the a and c lattice parameters, respectively). For comparison purposes, the values of the previously calculated lattice parameters in the literature are reported in **Table 7**, and more minor deviations of 1% are observed.[36–39] **Table 8** presents the calculated values of bond distances and angles of ZGO and Ni-ZGO. The Zn–O and Ge–O bonds of  $[\text{ZnO}_4]$  and  $[\text{GeO}_4]$  neighbor clusters increased slightly, 2.2% and 1.2%, respectively, while the Ni–O bond distances decreased by 8.9% and 6.2% for the O bond shared with Zn and Ge atoms, respectively. Moreover, the bond angles in the O–Zn–O and O–Ge–O decreases by 3.9% and 1.6%, respectively, while the O–Ni–O bond angles increase by +18.6%.

**Table 7** - Comparison between the theoretical lattice parameters obtained in this work with previous data reported in the literature.

Reference	Lattice parameters (Å)	
	a=b	c
<b>This work</b>	14.401	9.631
<b>Xie et al.[1]</b>	14.284	9.547
<b>Dolado et al.[2]</b>	14.270	9.530
<b>Huang et al.[3]</b>	14.231	9.530
<b>Breternitz et al.[4]</b>	14.482	9.665
<b>Liu et al.[5]</b>	14.486	9.656
<b>Balhara et al.[6]</b>	14.099	9.439

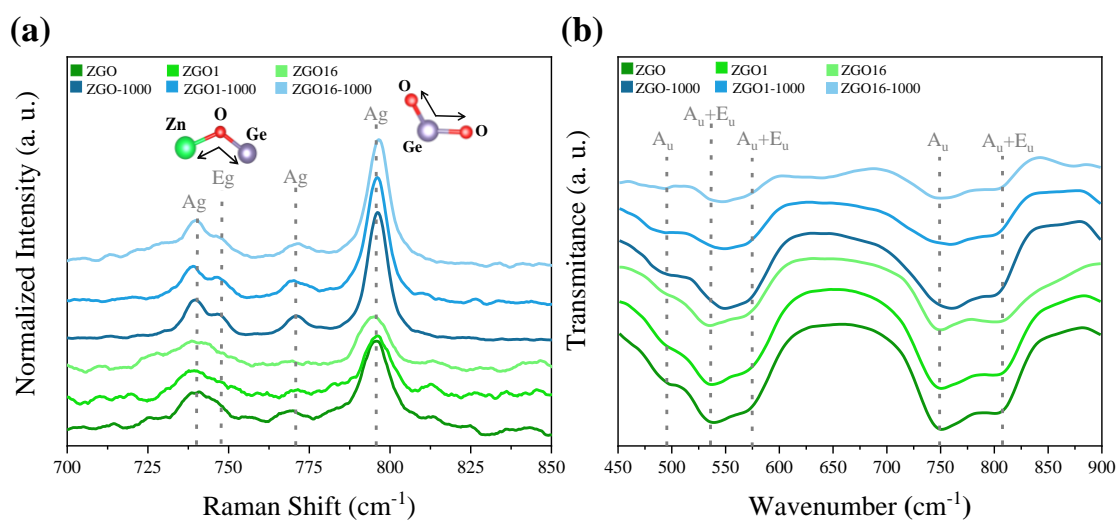
**Table 8** - Bond lengths and angles at [ZnO<sub>4</sub>], [GeO<sub>4</sub>], and [NiO<sub>4</sub>] clusters in the ZGO and Ni-ZGO models.

Model	Bond lengths (Å)			
	Zn-O*	Ge-O*	Zn-O	Ni-O
<b>ZGO</b>	1.960 (O3)	1.769 (O1)	1.981 (O2)	–
	1.969 (O4)	1.767 (O4)	1.960 (O3)	–
	1.981 (O2')	1.776 (O2')	1.969 (O4)	–
	1.996 (O2)	1.777 (O3)	1.996 (O2'')	–
<b>Ni-ZGO</b>	1.948 (O3)	1.762 (O1)	–	1.833 (O2)
	1.960 (O4)	1.764 (O4)	–	1.845 (O3)
	1.990 (O2')	1.782 (O2')	–	1.965 (O4)
	2.040 (O2)	1.799 (O3)	–	2.177 (O2'')
Model	Bond angles (Å)			
	(O2)–Zn– (O2')*	(O3)–Ge– (O2')*	(O2)–Zn–(O3)	(O2)–Ni– (O3)
<b>ZGO</b>	108.60	108.85	116.69	–
<b>Ni-ZGO</b>	104.56	107.08	–	143.38

\*Neighbor

#### 4.2.2 - Raman and FTIR

Raman and FTIR spectroscopies are crucial tools for analyzing the effects of short-range order and disorder in crystalline solids, complementing XRD analysis (**Figure 18**). For all samples, Raman modes in the range of 700 to 850  $\text{cm}^{-1}$  were identified (**Figure 18a**).[123] For the ZGO sample, 4 active Raman modes were observed, namely: 740  $\text{cm}^{-1}$  ( $A_g$ ), 747  $\text{cm}^{-1}$  ( $E_g$ ), 769  $\text{cm}^{-1}$  ( $E_g$ ), and 796  $\text{cm}^{-1}$  ( $A_g$ ), related to the stretching of Zn–O and Ge–O bonds and bending modes of Ge–O–Zn of the  $[\text{ZnO}_4]$  and  $[\text{GeO}_4]$  clusters [95,124,125] For sample ZGO1, these active Raman modes were observed with slight modifications. In sample ZGO16, the absence of the 770  $\text{cm}^{-1}$  mode was noted. After thermal treatment, an increase in the intensity and definition of Raman modes is observed, which can be associated with the increased crystallinity achieved through the thermal treatment.



**Figure 18** - (a) Raman spectra and (b) FTIR spectra of the samples.

**Table 9** presents the obtained values and previously reported literature on the active Raman modes of the rhombohedral ZGO structure. A comparison shows that the difference is less than 1%. [98,125]

**Table 9** - Comparison between the experimental and theoretical Raman modes obtained in this work with previous reported experimental values.

Mode	This work			Previous Experimental Values		
	Experimental ZGO	Experimental ZGO1000	Theo. ZGO	Hidalgo et al.[7]	Dolado et al.[8]	Balhara et al.[6]
$A_g$	740	740	730	745	745	744
$E_g$	747	747	-	753	751	762
$E_g$	769	771	776	777	777	776
$A_g$	796	796	796	802	802	801

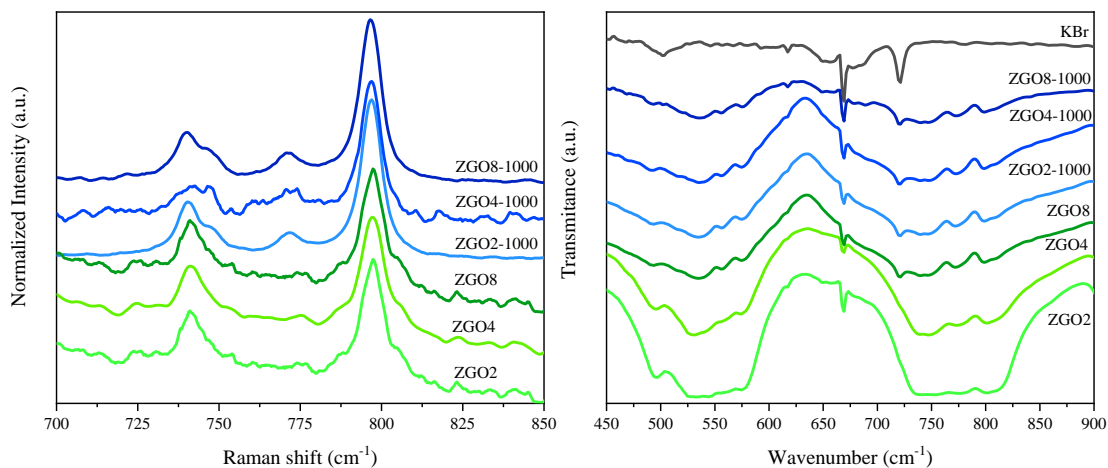
To better understand the changes in intensity and the loss of definition in the Raman modes of the samples, an analysis of the FWHM of the highest-intensity mode, located at  $\sim 796 \text{ cm}^{-1}$ , was conducted. The results obtained for the ZGO, ZGO1, and ZGO16 samples were 10.4, 10.4, and 12.2  $\text{cm}^{-1}$ , respectively. The calculation of the FWHM for this same mode in samples subjected to thermal treatment resulted in values of 7.6, 8.2, and 8.2  $\text{cm}^{-1}$  for the ZGO-1000, ZGO1-1000, and ZGO16-1000 samples, respectively. This difference observed in the FWHM values could be attributed to an increase in the order at short-range caused by the increase of  $\text{Ni}^{2+}$ .

The FTIR analysis was conducted, focusing on the region between 400 and 900  $\text{cm}^{-1}$ , as this range allows the identification of vibrations related to metal-oxygen bonds (**Figure 18b**). For  $\text{Zn}_2\text{GeO}_4$ , nine active vibrational modes ( $A_u$  and  $E_u$ ) can be identified in the infrared spectrum, where  $A_u$  modes exhibit polarization along the crystallographic z-axis. In contrast,  $E_u$  modes degenerate in the rhombohedral xy plane.[126].

It is possible to observe five bands in this region for the samples synthesized in this work. Between 400 and 600  $\text{cm}^{-1}$ , the modes associated with the symmetric stretching of the O-Zn-O bonds can be observed, with peaks at 493 ( $A_u$ ), 536 ( $A_u+E_u$ ), and 576  $\text{cm}^{-1}$  ( $A_u+E_u$ ). In the region between 600 and 900  $\text{cm}^{-1}$ , modes corresponding to the asymmetric stretching of the



O–Ge–O bonds are found, with peaks at  $748\text{ cm}^{-1}$  ( $A_u$ ) and  $808\text{ cm}^{-1}$  ( $A_u+E_u$ ). [44–48] As FTIR is not an analysis sensitive to local symmetry like Raman, significant changes are not observed between the samples. For samples with intermediate concentrations (2, 4, and 8%), the same trend is observed in both Raman spectroscopy and FTIR spectra (see **Figure 19**).

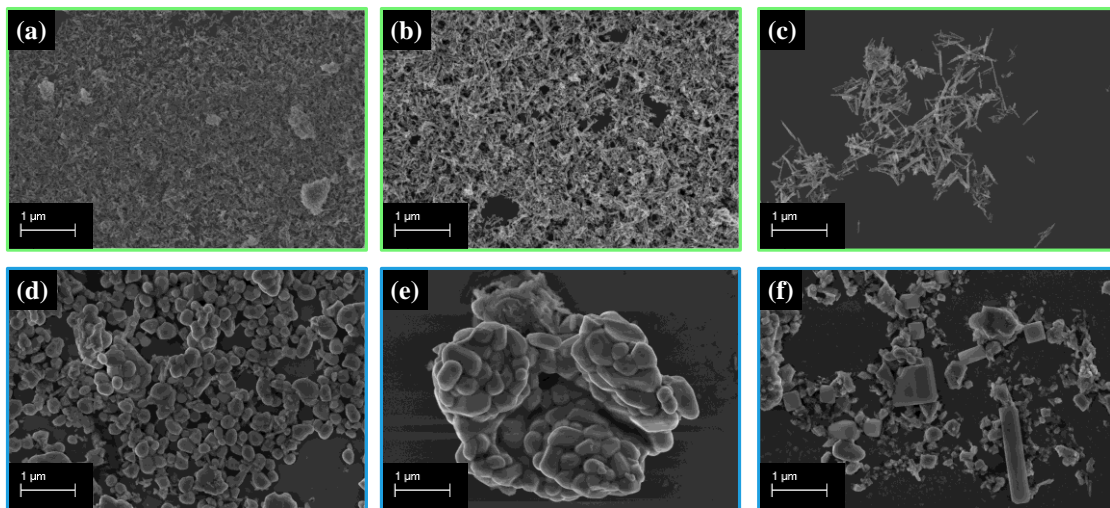


**Figure 19** - Raman spectroscopy (a) and FTIR (b) spectra for samples with intermediate concentrations (2, 4, and 8% Ni).

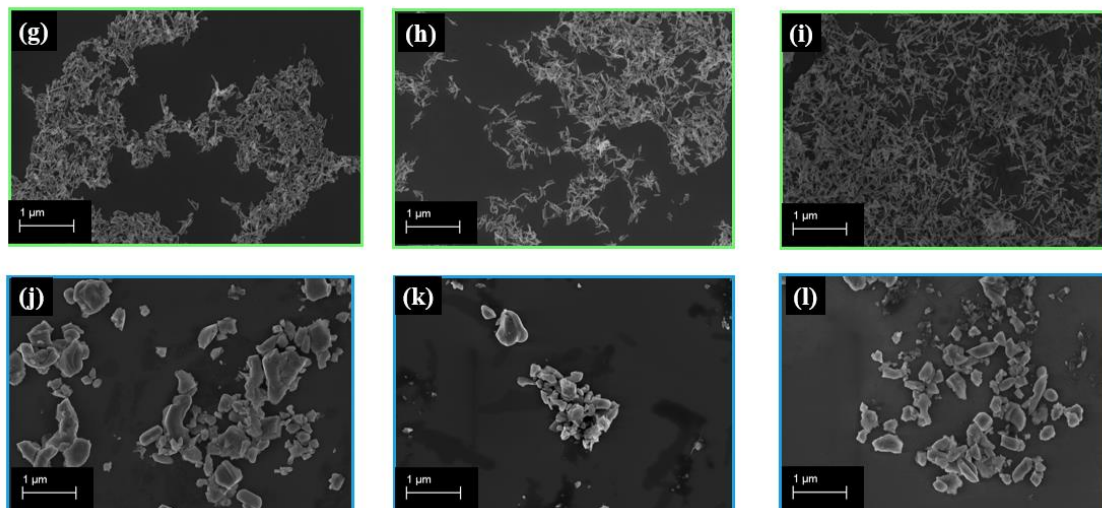
#### 4.2.3 - FE-SEM

The impact on the morphology of the as-synthesized samples was analyzed by FE-SEM (**Figure 20**). For the samples without thermal treatment, it is observed that all are formed by nanorods, according to previous results in other studies. [104, 132] The ZGO, ZGO1, and ZGO16 samples have average widths and lengths of 47.00 nm and 195.46, 54.47 nm and 195.39, and 62.61 nm and 175.44, respectively, noting that the increase in  $\text{Ni}^{2+}$  concentration induces an increase in nanorod width. After thermal treatment, the particles undergo a quasi-sintering process, significantly increasing their grain size and changing from nanorods to forming irregular polyhedrons, as reported in another study. [128] For the ZGO16-1000

sample, the formation of micro rods and cubes, likely induced by secondary phases, can be observed. ZGO-1000 and ZGO1-1000 samples present irregular polyhedrons with an average size of 645.43 nm and 491.73 nm, respectively. On the other hand, the ZGO16-1000 sample displays distinct morphologies due to different phases, where smaller structures have an average size of 139.92 nm, and rod-shaped particles have average widths and lengths of 51.16 nm and 256.12 nm. The thermal treatment induces a decrease in particle size and more pronounced morphological changes as the amount of increase in  $\text{Ni}^{2+}$  is increased. The SEM images related to the intermediate samples (2, 4, and 8%) are shown in **Figure 21** and follow the same trend observed previously.



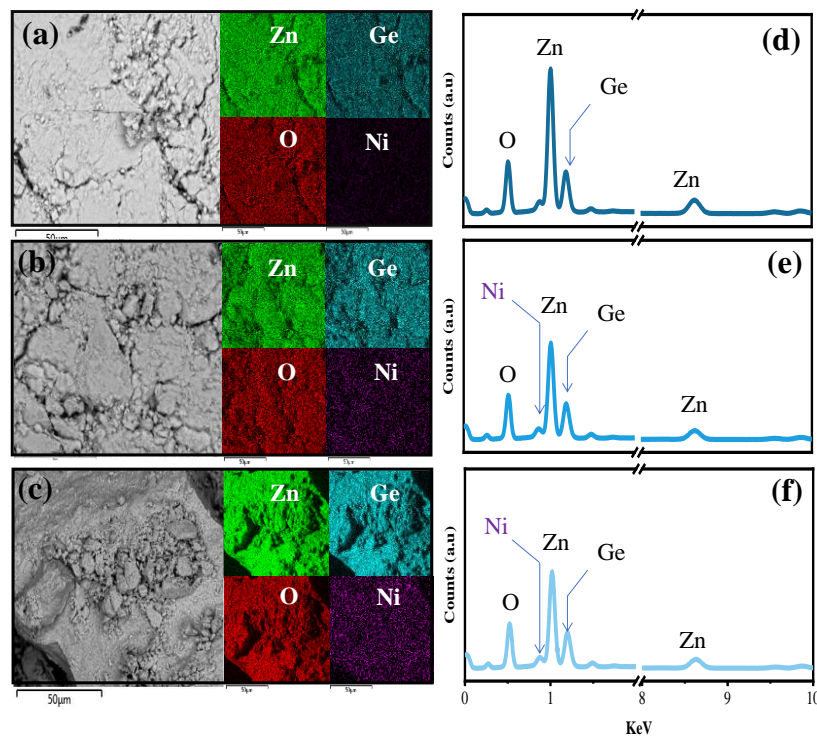
**Figure 20** - FE-SEM images of the samples (a) ZGO, (b) ZGO1, (c) ZGO16, (d) ZGO-1000, (e) ZGO1-1000, and ZGO16-1000.



**Figure 21** - FE-SEM images of the samples with intermediate concentrations: (g) ZGO2, (h) ZGO4, (i) ZGO8, (j) ZGO2-1000, (k) ZGO4-1000, and (l) ZGO8-1000.

#### 4.2.4 - EDS

The elemental surface mapping of the samples by EDS was performed after thermal treatment, as shown in **Figure 22**. As these samples were obtained from samples without thermal treatment, the Ni content in both is equal. Zn, Ge, and O were identified in all samples, with Ni observed only in the doped samples. Although EDS analysis is partially quantitative, and its interpretation depends on the material's surface characteristics, the uniform detection of Ni throughout the sample and its quantification close to nominal ( $x = 0.01$  and  $0.16\%$ ) reinforce that all the Ni added during synthesis is present in the sample.



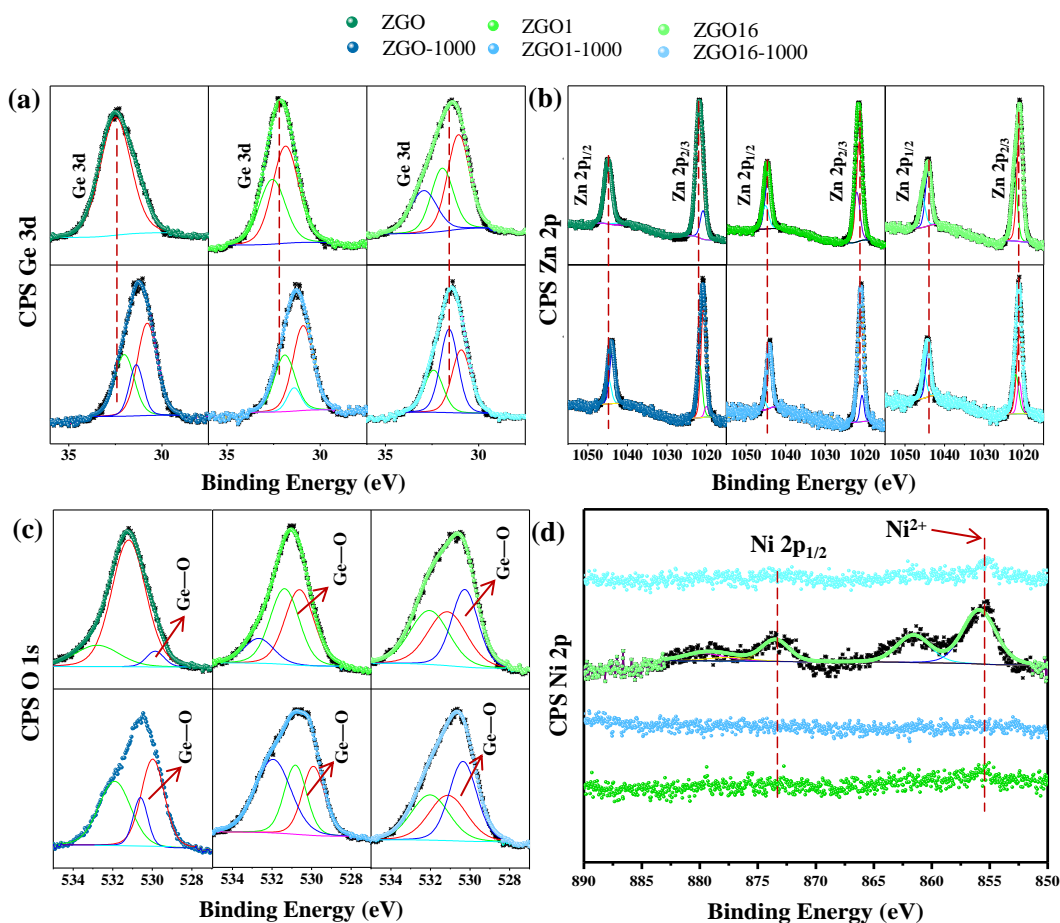
**Figure 22** - EDS Spectrum of samples after heat-treatment (a) ZGO-1000 undoped, (b) ZGO1-1000, and (c) ZGO16-1000.

#### 4.2.5 - XPS

XPS was employed to perform a detailed surface evaluation to examine the effects of  $\text{Ni}^{2+}$  doping and heat treatment on the ZGO samples. **Figure 23** presents the XPS spectra for Ge 3d, Zn 2p, O 1s, and Ni 2p, respectively. These high-resolution spectra confirm the existence of elements constituting the  $\text{Zn}_2\text{GeO}_4$  structure, providing evidence for the successful formation of the material.

In **Figure 23a**, the Ge 3d peaks reveal binding energies centered around 31 eV, indicative of the presence of  $\text{Ge}^{2+}$  state oxidation, while around 32 and 33 eV bonds are associated with the tetravalent form of  $\text{Ge}^{4+}$ . [133-135] One insight from XPS about Ge 3d is that the thermal treatment applied to the ZGO-1000 and ZGO1-1000 samples influenced the binding energy of

the Ge 3d orbital. The shift towards lower energy values implies the potential development of stronger bonds between Ge and O within the crystal lattice. This observation underscores the substantial influence of heat treatment on structural alterations, as supported by the FWHM of the (410) peak in the XRD results, indicating a reduction in values for the heat-treated ZGO samples. While the diminishing FWHM suggests a long-range structural order, it is noteworthy that the ZGO16-1000 sample does not exhibit changes in the Ge 3d binding energy. This discrepancy can be attributed to the doping-induced, more significant long-range structural disorder and the appearance of new phases, preventing a shift towards lower binding energy in this specific case.



**Figure 22** - Ge 3d XPS spectra of the ZGO samples (a) Zn 2p XPS spectra of the ZGO samples (b) O 1s XPS spectra of the ZGO samples (c) Ni 2p XPS spectra of Ni<sup>2+</sup>-doped ZGO samples.

In **Figure 23b**, high-resolution XPS spectra reveal binding energy peaks at 1045 and 1022 eV, corresponding to the Zn 2p<sub>3/2</sub> and Zn 2p<sub>1/2</sub> states, respectively. These peaks demonstrate the oxidation state of Zn<sup>2+</sup>. [136] Fitted high-resolution XPS spectra of the O 1s region (**Figure 5c**) reveal a peak in the binding energy range between 529-530 eV, attributed to the crystal lattice oxygen (O<sup>2-</sup>) constituents of Ge–O bonds. [50,54] Furthermore, peaks in the 531 eV and 532 eV are observed, associated with the presence of oxygen hydroxyl groups and the surface adsorption of water molecules.

Due to the lower doping concentration, the Ni<sup>2+</sup> peaks are notably absent in ZGO1 and ZGO1-1000 materials, as illustrated in **Figure 23d**. [138] In contrast, for the ZGO16 and ZGO16-1000 samples, Ni 2p<sub>3/2</sub> and Ni 2p<sub>1/2</sub> peaks become evident at binding energies of 856.3 eV and 872.5 eV, respectively. These peaks correspond to the presence of Ni<sup>2+</sup> cations within the material. An interesting fact for the heat-treated samples: apparently, there is a migration of Ni<sup>2+</sup> from the surface to the bulk. This is known because the same sample was used for both processes, and the elemental distribution revealed by EDS mapping shows a homogeneous distribution, with quantitative analysis close to nominal values. In this way, the surface composition of ZGO can likely be altered through heat treatment, making it an intriguing process for the design of new ZGO-based materials.

#### *4.2.6 - Energy of band gap*

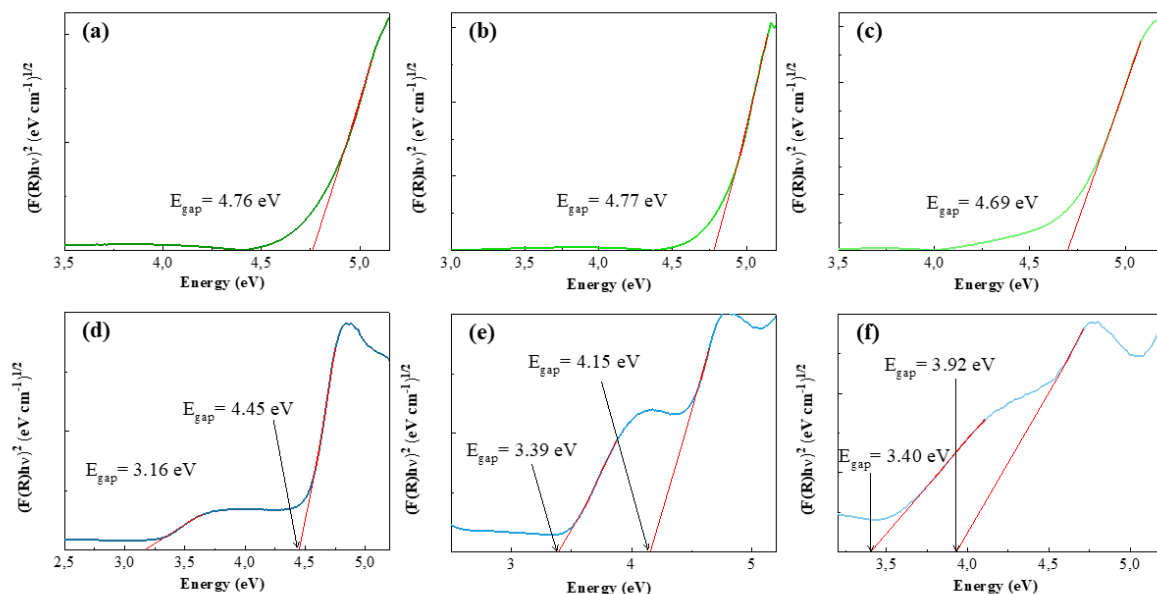
The changes in electronic properties caused by Ni<sup>2+</sup> doping in the samples, both before and after thermal treatment, were analyzed by DRS. Reflectance spectra were used to calculate the optical band gap energies

( $E_{\text{gap}}$ ) using the Wood-Tauc and Kubelka-Munk equations [139]. Previous studies indicate that  $\text{Zn}_2\text{GeO}_4$  exhibits a band gap with direct transitions.[96,104,140] In **Figures 24a-c**, representing the samples without thermal treatment, an  $E_{\text{gap}}$  of 4.76 eV is observed for ZGO, while ZGO1 and ZGO16 show  $E_{\text{gap}}$  values of 4.77 and 4.69 eV, respectively, with no significant changes.

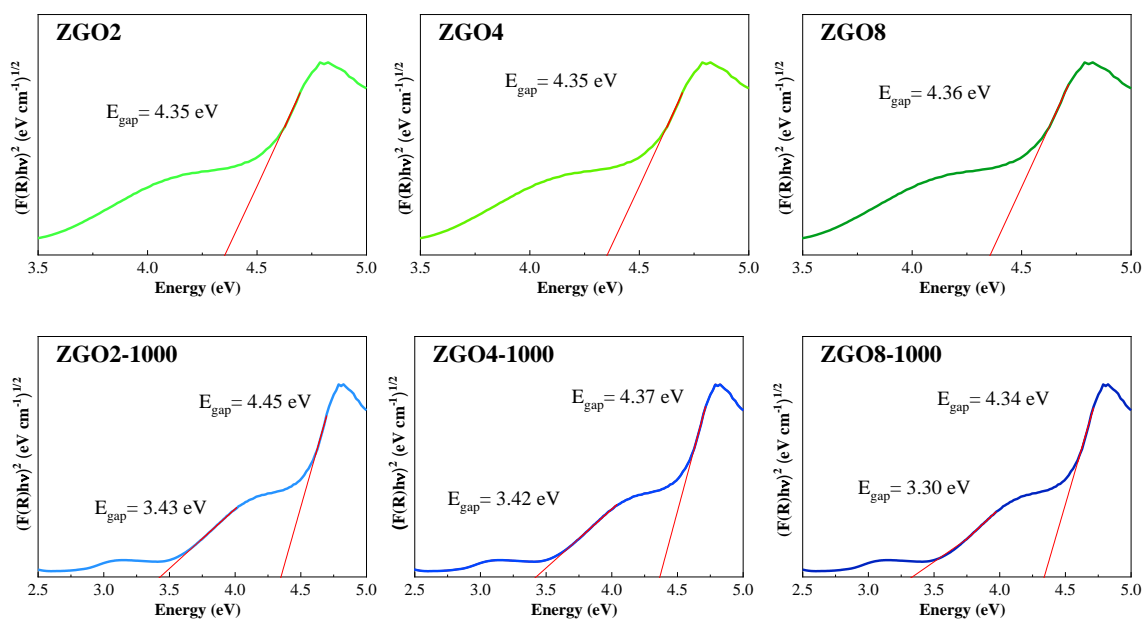
In **Figures 24d-f**, representing the samples after thermal treatment, the appearance of the additional band gaps is observed, in agreement with previous literature [141]. The  $E_{\text{gaps}}$  for the ZGO-1000 sample were 3.16 eV and 4.45 eV, for ZGO1-1000 were 3.40 eV and 4.08 eV, and for ZGO16-1000 were 3.40 eV and 3.92 eV. The  $E_{\text{gap}}$  values of the intermediate samples follow the trend observed for the samples with and without thermal treatment, and are shown in **Figure 25**.

From these values, we can draw two conclusions: (1) thermal treatment induces the appearance of new, well-defined electronic transitions due to changes in short- and long-range order in the materials, and (2)  $\text{Ni}^{2+}$  doping in a highly structurally organized crystal lattice (due to thermal treatment) also induces the creation of intermediate levels in the forbidden region due to the generation of new local defects caused by  $\text{Ni}^{2+}$ -doping and the acquisition of new phases.





**Figure 23** - Energy of band gap ( $E_{\text{gap}}$ ) of the samples. (a) ZGO; (b) ZGO1; (c) ZGO16; (d) ZGO-1000; (e) ZGO1-1000, and (f) ZGO16-1000.



**Figure 24** - Energy of band gap ( $E_{\text{gap}}$ ) of the samples with intermediate concentrations (2, 4, and 8% Ni).

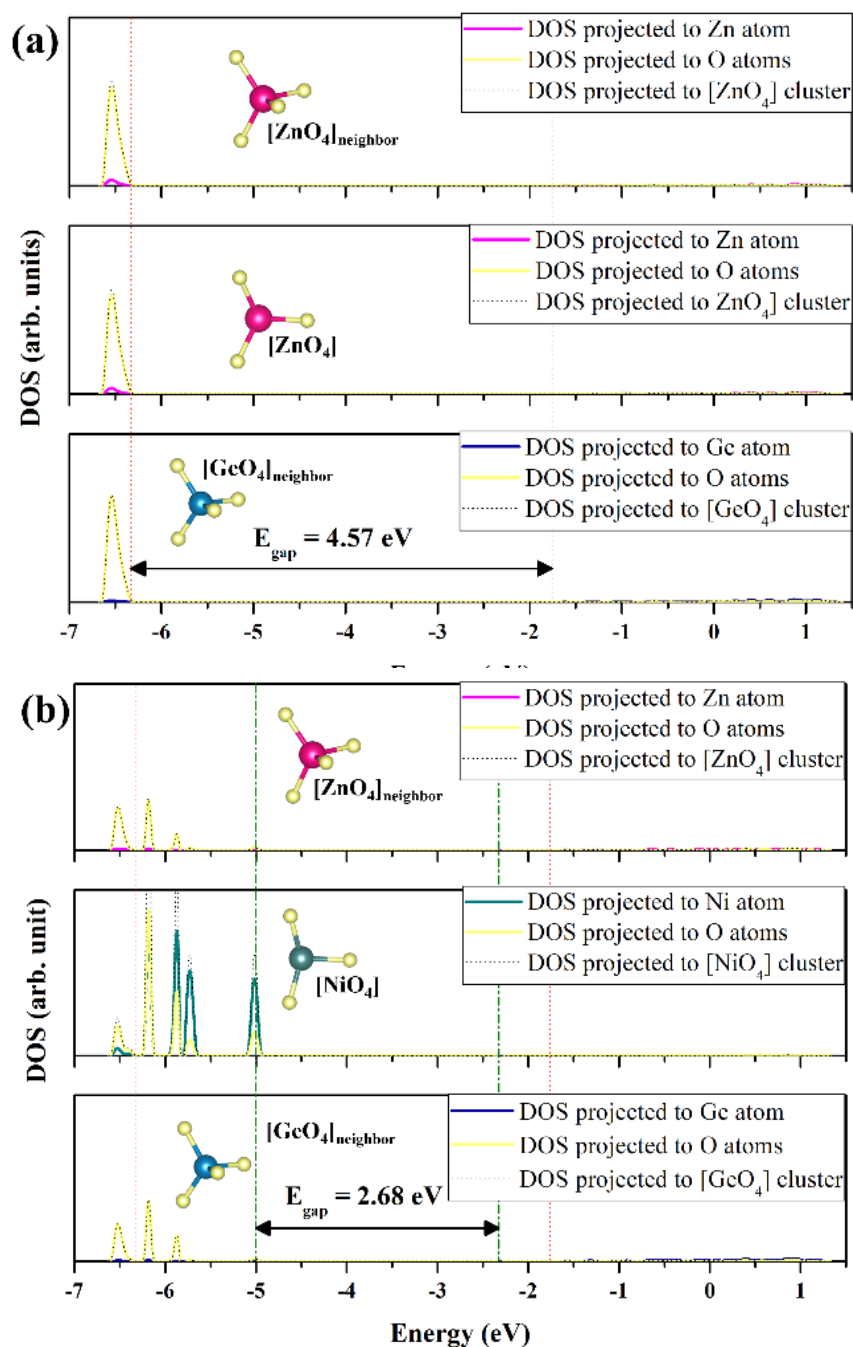


#### 4.2.7 - DOS

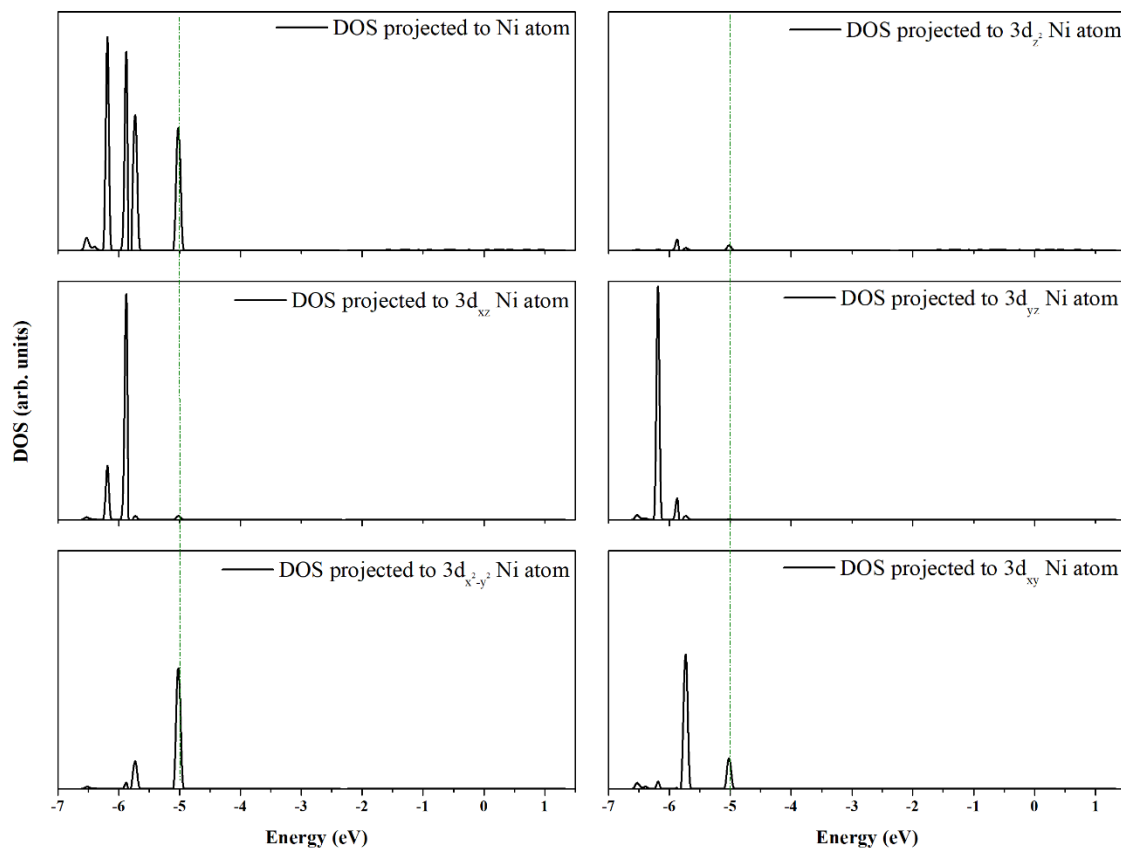
The DOS plot for ZGO is displayed in **Figure 26a**. An analysis of the results renders that the valence band maximum (VBM) is mainly composed of Zn (d) and O (p) orbitals. In contrast, the conduction band minimum (CBM) is dominated by a hybridization of Zn(s), Ge(s), and O(p) orbitals. The electronic transition between the VBM and CBM presents an  $E_{\text{gap}}$  value of 4.57 eV. It is a direct transition at the  $\Gamma$ -point in the Brillouin zone, in agreement with the experimental value.

To understand how the  $\text{Ni}^{2+}$ -doping process modulates the electronic structure of ZGO, the DOS of the Ni-ZGO was further analyzed, as illustrated in **Figure 26b**. The top of the VBM is now mainly composed of 3d Ni orbitals and 2p O orbitals, and a strong hybridization between them, with a minor contribution from the Zn and Ge orbitals, and a decrease of the band gap value is observed ( $E_{\text{gap}} = 2.68$  eV). On the other hand, a detailed analysis of DOS projected at the 3d orbitals of Ni was performed.

As can be seen at **Figure 27**, the 3d  $\text{Ni}^{2+}$  orbitals are non-degenerated, and the top of the VB is constituted by the  $3d_{x^2-y^2}$  followed by  $3d_{xy}$  with a smaller contribution of  $3d_{z^2}$ . This fact results in shallow traps and improved carrier separation.



**Figure 25** - (a) DOS projected onto the atoms within the  $[\text{ZnO}_4]_{\text{neighbor}}$ ,  $[\text{ZnO}_4]$  that was replaced by  $\text{Ni}^{2+}$  cation, and  $[\text{GeO}_4]_{\text{neighbor}}$  clusters at the ZGO model. (b) DOS projected onto the atoms within the  $[\text{ZnO}_4]_{\text{neighbor}}$ ,  $[\text{NiO}_4]$ , and  $[\text{GeO}_4]_{\text{neighbor}}$  clusters at the Ni-ZGO model.



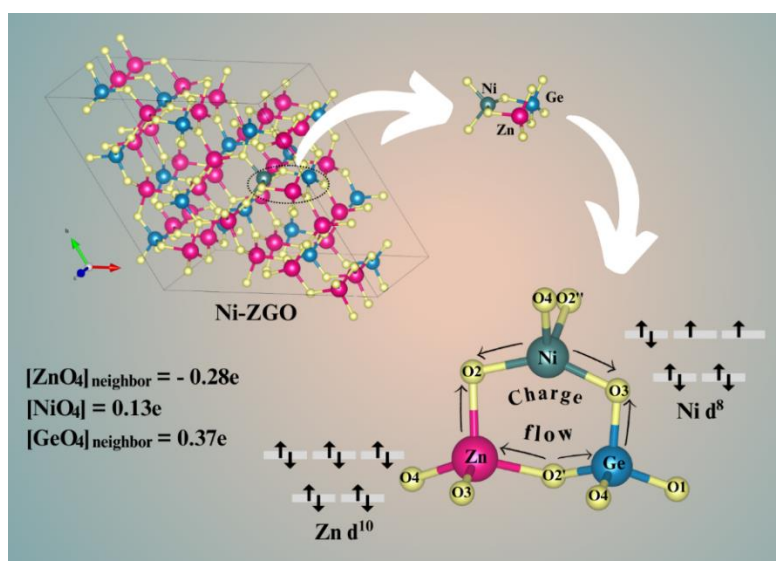
**Figure 26** - DOS projected to 3d orbitals from Ni atom at Ni-ZGO model.

The values of Mulliken atomic charges values are listed in **Table 10**. An analysis and comparison of ZGO and Ni-ZGO models show that the presence of  $\text{Ni}^{2+}$  cations induce an increase in the negative charge of O anions belonging to the  $[\text{NiO}_4]$  cluster. There is a decrease of the positive charge of a neighbor  $[\text{GeO}_4]$  cluster, from  $0.46e$  to  $0.37e$ , while the substituted site at  $[\text{ZnO}_4]$  cluster, with a negative charge of  $-0.23e$ , increases its positive charge to  $0.13e$  when is replaced by  $[\text{NiO}_4]$  cluster in the doping process. Therefore,  $[\text{NiO}_4]$  and neighbor  $[\text{GeO}_4]$  and  $[\text{ZnO}_4]$  clusters are the sites where positive and negative charges, respectively, are accumulated after the  $\text{Ni}^{2+}$  doping process. Therefore, we suggest that the true driving force to facilitate this charge separation and electronic flow from the  $[\text{NiO}_4]$  and neighbor  $[\text{GeO}_4]_{\text{neighbor}}$  and  $[\text{ZnO}_4]_{\text{neighbor}}$  clusters to shared oxygen anions

behavior is responsible for the appearance of blue color as it is depicted in **Figure 28**.

**Table 10** - Calculated Mulliken charges of Zn, O, Ge, and Ni atoms and  $[\text{ZnO}_4]_{\text{neighbor}}$ ,  $[\text{GeO}_4]_{\text{neighbor}}$ ,  $[\text{ZnO}_4]$  that was replaced by  $\text{Ni}^{2+}$  cation, and  $[\text{NiO}_4]$  clusters.

	$\text{Zn}_{\text{neighbor}}$	O	$\text{Ge}_{\text{neighbor}}$	O	Zn	Ni	O
<b>ZGO</b>	1.03	- 0.95 (O3)	1.72	- 0.95 (O1)	1.03	-	- 0.94 (O2)
		- 0.94(O4)		- 0.94 (O4)			- 0.95 (O3)
		- 0.94 (O2')		- 0.94 (O2')			- 0.95 (O4)
		- 0.94 (O2)		- 0.95 (O3)			- 0.94 (O2'')
<b>Ni-ZGO</b>	1.00	- 0.95 (O3)	1.66	- 0.94 (O1)	-	1.49	- 1.04 (O2)
		- 0.94 (O4)		- 0.93 (O4)			- 1.04 (O3)
		- 0.94 (O2')		- 0.94 (O2')			- 0.99 (O4)
		- 1.04 (O2)		- 1.04 (O3)			- 1.00 (O2'')
	$[\text{ZnO}_4]_{\text{neighbor}}$		$[\text{GeO}_4]_{\text{neighbor}}$		$[\text{ZnO}_4]$		$[\text{NiO}_4]$
<b>ZGO</b>		- 0.23		0.46		- 0.23	-
<b>Ni-ZGO</b>		- 0.28		0.37		-	0.13



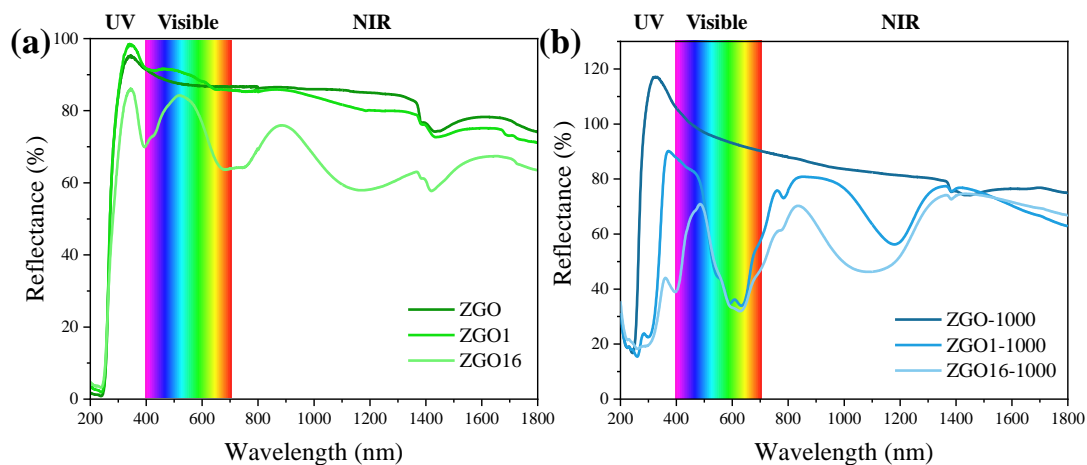
**Figure 27** - Schematic representation of the  $[\text{NO}_4]$ , neighbor  $[\text{ZnO}_4]$  (at the six-membered rings composed only by  $\text{Zn}_2$  sites) and  $[\text{GeO}_4]$  (at the six-membered rings composed by  $\text{Z}_1$  sites and Ge). Values of the Mulliken charges and the respective metal electronic configuration induced by the  $\text{Ni}^{2+}$ -doping process.

#### 4.2.8 - DRS

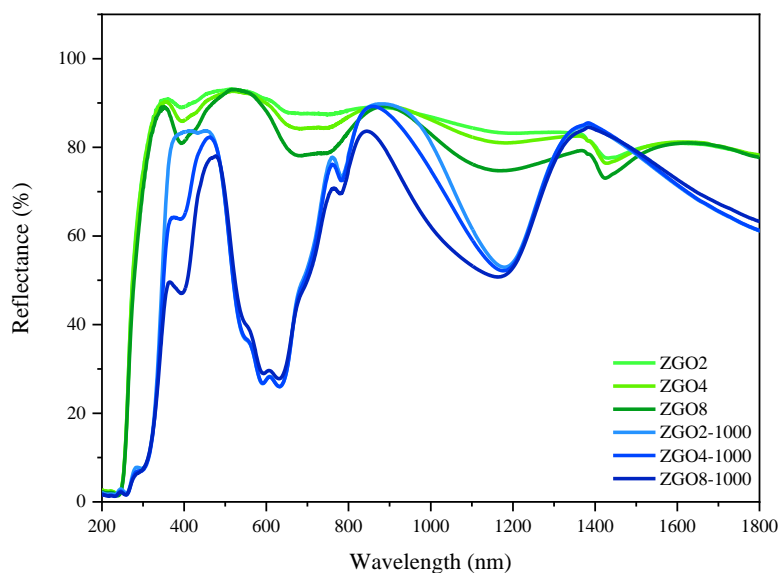
The DRS of the samples in the ultraviolet-visible region (between 200 and 800  $\text{cm}^{-1}$ ) and near-infrared (NIR, 800-1800  $\text{cm}^{-1}$ ) are shown in **Figure 28**. For the samples without thermal treatment (**Figure 28a**), it is observed that the ZGO and ZGO1 samples do not exhibit any absorption in the visible range, resulting in no coloration. In sample ZGO16, it is possible to identify two distinct bands: a prominent band located between 350 and 500  $\text{cm}^{-1}$  and a broader band spanning the range of 500 to 800  $\text{cm}^{-1}$ . For the samples after thermal treatment (**Figure 28b**), it is noted that the ZGO-1000 sample does not show any absorption, imparting the expected white color. However, for the ZGO1-1000 and ZGO16-1000 samples, absorptions in the visible range are observed. The same behavior is observed for the samples with intermediate concentrations of 2, 4, and 8% (**Figure 29**). In the ZGO16, ZGO1-1000, and ZGO16-1000, two overlapping bands are observed in the range of 500-670 nm. The d-d transitions associated with the permitted configurations of the  $\text{Ni}^{2+}$  ion coordinated tetrahedrally include the states  $^3A_2$  ( $^3P$ ),  $^3E$  ( $^3P$ ),  $^1T_2$  ( $^1G$ ),  $^1A_1$  ( $^1G$ ), and  $^1T_1$  ( $^1G$ ). [108]

Additionally, a weak broadband in the range of 600-800 nm is observed, corresponding to the allowed spin transitions  $\nu_2$  ( $^3A_{2g} \rightarrow ^3T_{1g}$  (F)) of the  $\text{Ni}^{2+}$  ion coordinated octahedrally. [142,143] With the increase in  $\text{Ni}^{2+}$  concentration, a prominent band emerges in the spectral range of 380 nm to approximately 400 nm, indicating charge transfer between oxygen (O), zinc (Zn), and nickel (Ni) atoms. [142]. Specifically, the prominent band at 400 nm is observed in the sample with 16%  $\text{Ni}^{2+}$ , where the  $\text{Ni}^{2+}$  ion is coordinated octahedrally ( $^3A_2 \rightarrow ^3T(F)$ ). Additionally, it is noteworthy the presence of two weak bands between 710-780 nm in the samples with 1% and 16%  $\text{Ni}^{2+}$ . At 710 nm, the transition  $^3T_{1g}$  ( $^3F$ ) occurs with the  $\text{Ni}^{2+}$  ion

coordinated octahedrally, while at 780 nm, the transitions  ${}^1E$  ( ${}^1D$ ) and  ${}^1T_2$  ( ${}^1D$ ) occur with the  $Ni^{2+}$  ion coordinated tetrahedrally.[108] In the NIR region, two broad and overlapping bands in the 850-1300 nm range are also observed for the  $Ni^{2+}$ -doped samples, attributed to allowed spin transitions  ${}^3A_{2g} \rightarrow {}^3T_{2g}$  (F). This absorption in the NIR can be of interest in developing NIR reflective pigments.



**Figure 28** - Spectra of absorption in the UV-Vis and NIR regions for the samples (a) untreated and (b) thermally treated.

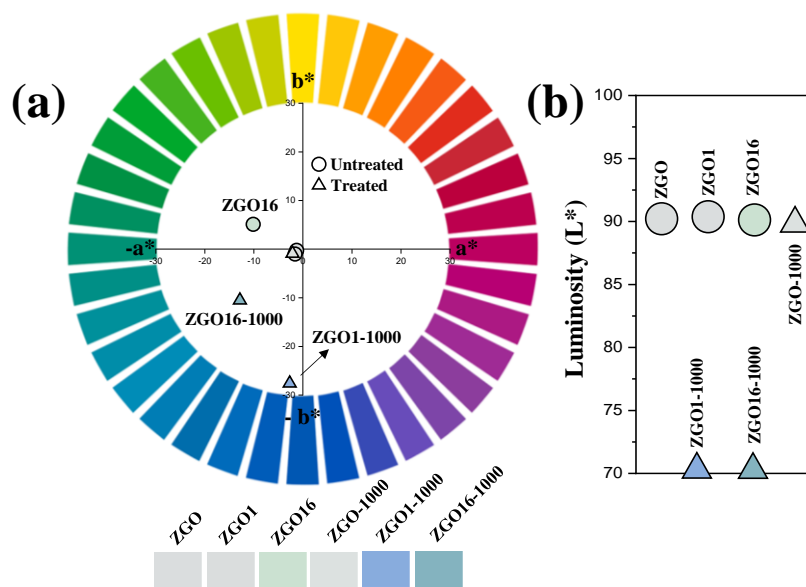


**Figure 29** - Spectra of absorption in the UV-Vis and NIR regions for the samples with intermediate concentrations (2, 4, and 8% Ni).

#### 4.2.9 - Colorimetric




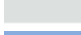


The color of the samples was determined using the CIELab colorimetric method. The photos of the powders obtained in this work are shown in **Figure 32**. This CIELab color space, standardized by the Commission Internationale d'Eclairage, identifies colors in a 3D model composed of coordinates.[144] The coordinates  $a^*$  and  $b^*$  are related to colors such as yellow ( $-b^*$ ), blue ( $b^*$ ), green ( $-a^*$ ), and red ( $a^*$ ). In contrast, the  $L^*$  coordinate indicates the brightness of the color, ranging from 0, representing a material towards black, to 100 for lighter materials close to white.

Analyzing **Figure 30a** and the data in **Table 11**, it can be observed that the ZGO, ZGO1, and ZGO-1000 pigments showed slight differences in the values of the  $-a^*$  and  $-b^*$  coordinates, indicating a subtle change in the color of the pure pigment and when doped with low amounts of  $\text{Ni}^{2+}$  without thermal treatment. The ZGO16 sample appears with a light green hue, with  $a^*$  and  $b^*$  coordinates of  $-10.07 \pm 0.011$  and  $5.30 \pm 0.024$ , respectively. Upon calcination of the samples at  $1000^\circ\text{C}$ , ZGO1-1000 and ZGO16-1000 undergo significant variations in hue. The ZGO1-1000 sample appears as a purer blue pigment, with  $a^*$  and  $b^*$  coordinates of  $2.73 \pm 0.087$  and  $-28.00 \pm 1.050$ , while the increased concentration of  $\text{Ni}^{2+}$  in the ZGO16-1000 sample results in obtaining a pigment with a greenish blue color, with  $a^*$  and  $b^*$  coordinates of  $-13.61 \pm 0.009$  and  $-11.58 \pm 0.089$ . It is important to note that intermediate concentrations between 16% and 1% were tested, which do not show changes in their hues compared to the ZGO1-1000 sample (see **Figure 31** and **Table 12**). Additionally, a decrease in the brightness of the thermally treated pigments is noticeable as they are doped (**Figure 30b**).



**Figure 30** - (a)  $a^*$  (green and red),  $b^*$  (yellow and blue) and (b) and  $L^*$  (lightness, with 100 representing white and 0 representing black) CIE Lab coordinates for the samples.

**Table 11** - The samples' colorimetric parameters ( $L^*$ ,  $a^*$ ,  $b^*$ , color).

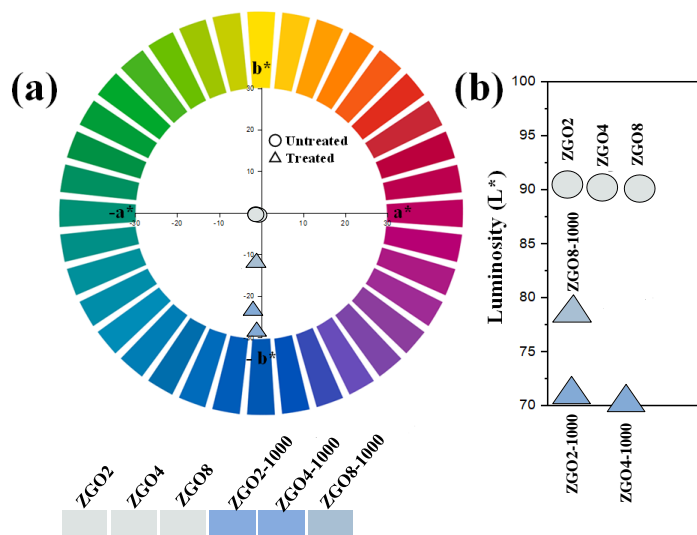
Sample	$a^*$	$b^*$	L	Color
ZGO	$-0.86 \pm 0.019$	$-0.73 \pm 0.004$	$89.43 \pm 0.077$	
ZGO-1	$-1.90 \pm 0.030$	$-0.12 \pm 0.063$	$90.60 \pm 0.016$	
ZGO-16	$-10.07 \pm 0.011$	$5.30 \pm 0.024$	$88.89 \pm 0.044$	
ZGO-1000	$-1.25 \pm 0.003$	$-0.30 \pm 0.030$	$89.53 \pm 0.063$	
ZGO-1-1000	$-2.73 \pm 0.087$	$-28.00 \pm 1.050$	$71.47 \pm 1.344$	
ZGO-16-1000	$-13.61 \pm 0.009$	$-11.58 \pm 0.089$	$71.19 \pm 0.063$	

Ahmed et al. conducted a study on blue pigments, where the doping of  $Ni^{2+}$  in  $MgAl_2O_4$  resulted in a reduction in the brightness of the doped samples as the concentration of  $Ni^{2+}$  increased. [145] Additionally, the increase in temperature also led to changes in the values of  $a^*$  and  $b^*$ , with an increase towards the depth of the green-blue color. Blue pigments based on  $Ca_{1-x}La_xAl_{12-x}Ni_xO_{19}$  were obtained by coupled substitution ( $Ca^{2+} + Al^{3+}$ )  $\rightarrow$  ( $La^{3+} + Ni^{2+}$ ) in the hibonite structure by IANOS et al.[108]  $Ni^{2+}$ -doped









samples exhibited negative values of  $a^*$  and  $b^*$ , indicating a bluish-green hue. Increasing the  $\text{Ni}^{2+}$  content intensified the blue color, as confirmed by the decrease in  $b^*$  and  $L^*$  values. Wang et al. obtained blue pigments based on  $\text{V-ZrSiO}_4$  calcined at  $1100^\circ\text{C}$  for 1 hour. [88] While the pure sample exhibited a white color, those containing vanadium showed a more intense blue hue, with reduced  $L^*$  and  $b^*$  values. Increasing the vanadium concentration resulted in a decrease in  $L^*$  and  $b^*$ . Notably, the sample with 2% vanadium exhibited the brightest blue color.

These findings suggest that controlled addition of vanadium can enhance the quality of the pigment for specific applications. In this work, the observed difference in coloration is attributed to two factors: (1) a more significant contribution of charge transfer between O, Zn, and Ni, as evidenced in the analysis of the DRS spectra, and (2) the difference in coordination of  $\text{Ni}^{2+}$  clusters, which are in octahedral sites in the  $\text{NiO}$  and  $\text{Zn}_{0.2}\text{Ni}_{0.8}\text{GeO}_4$  phases, and tetrahedral sites when acting as dopants in  $\text{Zn}_2\text{GeO}_4$  phase, corroborating with the obtained theoretical results.[142]

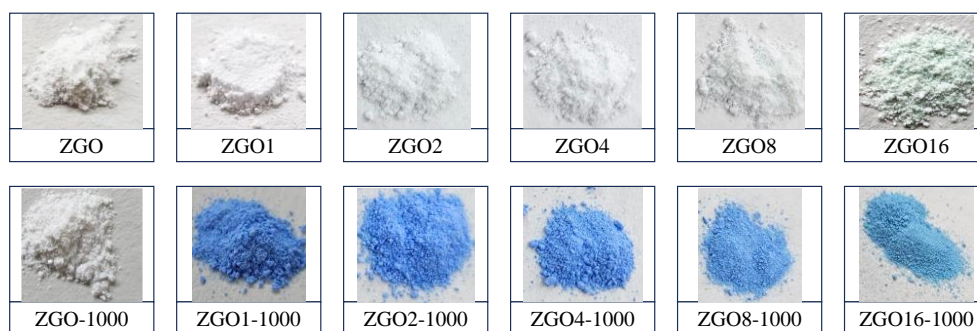


**Figure 31** - (a)  $a^*$  (green and red),  $b^*$  (yellow and blue), and (b) and  $L^*$  (lightness, with 100 representing white and 0 representing black) CIELab coordinates for the samples with intermediate concentrations (2, 4, and 8% Ni).

**Table 12** - Colorimetric parameters ( $L^*$ ,  $a^*$ ,  $b^*$ , color) of the samples (2, 4 e 8 % Ni) untreated and thermally treated.

Sample	$a^*$	$b^*$	L	Color
ZGO-2	$-2.44 \pm 0.027$	$-0.06 \pm 0.029$	$91.38 \pm 0.023$	
ZGO-4	$-3.15 \pm 0.030$	$-0.56 \pm 0.051$	$90.75 \pm 0.062$	
ZGO-8	$-5.74 \pm 0.016$	$-2.08 \pm 0.011$	$90.08 \pm 0.024$	
ZGO2-1000	$-2.39 \pm 0.040$	$-29.35 \pm 0.185$	$71.26 \pm 0.022$	
ZGO4-1000	$-4.84 \pm 0.014$	$-25.52 \pm 0.136$	$70.37 \pm 0.054$	
ZGO8-1000	$-4.83 \pm 0.005$	$-12.21 \pm 0.045$	$77.99 \pm 0.074$	

A previously mentioned, the d-d transitions of the  $Ni^{2+}$  cation in a tetrahedral symmetry play a crucial role in the origin of the observed blue coloration. Under the influence of crystal field theory, the five d orbitals of the  $Ni^{2+}$  cation experience an energy separation due to interaction with surrounding oxygen atoms in a tetrahedral environment. In this context, d-d transitions occur when electrons are excited between the energy levels of the orbitals [108] The Jahn-Teller effect, in turn, contributes to the system's complexity by promoting a geometric distortion that breaks the tetrahedral symmetry. [105] This distortion is particularly significant for  $Ni^{2+}$  cations in tetrahedral environments, influencing their spectral and magnetic properties. An analysis of the DOS renders that 3d orbitals of the  $Ni^{2+}$  cation is non-degenerate, been the  $3d_{x^2-y^2}$  orbital the most energetic at the top of VB. However, it is essential to note the limitations of the present strategy, which focuses on the local environment without considering the complexity of the entire system.



**Figure 32** - Images of pure and Ni-doped powders at various concentrations (0 to 16% Ni).

## 5 - Conclusions

### 5.1 - V-doped AW

Here, we present a protocol for synthesizing highly active and selective  $\alpha$ -Ag<sub>2</sub>WO<sub>4</sub> catalysts for the oxidation of sulfides to sulfones in the absence of light, based on the doping process of  $\alpha$ -Ag<sub>2</sub>WO<sub>4</sub> with vanadium. This is an effective approach to improve its performance for this transformation under mild conditions and selectively oxidizes various classes of sulfides. Furthermore, we show how changes in the exposed surfaces at the morphology can modulate the selectivity of the V-doped AW samples.

The main conclusions of this work can be summarized as follows: (i) the V-doped  $\alpha$ -Ag<sub>2</sub>WO<sub>4</sub> catalyst is more efficient for the oxidation of sulfides to sulfones than undoped AW, (ii) high yields and selectivity of different types of sulfones were obtained in a relatively short time. The kinetic study of the 0.01% V sample showed >99% selectivity for sulfones after 30 minutes of reaction, while the undoped sample presented 87%, and the catalyst exhibited good stability with a 9% loss of activity after the fifth recycle, (iii) based on the above results, we propose that by adjusting the morphology ((100) surface is the best), their catalytic activity can be maximized, (iv) from results of scavenger experiments, a mechanism is proposed for the efficient oxidation reaction based on the presence of electron-hole ( $e^-/h^+$ ) pairs, hydroxyl radical ( $\bullet$ OH) and singlet oxygen ( $^1$ O<sub>2</sub>), (v) EPR and XPS measurements pointed out the characteristic signal of V<sup>4+</sup> cation in the doped samples.

This study provides new insights into the design of high-performance  $\alpha$ -Ag<sub>2</sub>WO<sub>4</sub>-based catalysts for practical applications, based on

structure-activity relationships. Our work could broaden ideas and lay a foundation for the development of catalysts for the oxidation reaction of sulfides to sulfones in the absence of light. Present results are relevant to ongoing efforts to understand the catalytic activity induced by doping and provide potential for future work in this field.

## 5.2 - Ni-doped ZGO

The current investigation focuses on the potential use of Ni<sup>2+</sup>-doped Zn<sub>2</sub>GeO<sub>4</sub> (x = 0, 0.01, and 0.16 mol%) samples as a blue pigment. Doping with Ni<sup>2+</sup> at low concentrations (x = 0.01%) resulted in the pure rhombohedral phase of Zn<sub>2</sub>GeO<sub>4</sub>. However, at higher Ni<sup>2+</sup> concentrations (x = 0.16%), the coexistence of additional phases, NiO (~3%) and Zn<sub>1.2</sub>Ni<sub>0.8</sub>GeO<sub>4</sub> (~8%) was observed. XPS analysis revealed that thermal treatment can also alter the material surface. The substitution of Zn<sup>2+</sup> by Ni<sup>2+</sup> at x = 0.01% directionally regulates the electron transfer, likely occurring from [NiO<sub>4</sub>] to tetrahedral [ZnO<sub>4</sub>] and [GeO<sub>4</sub>] neighbor clusters, which is responsible for the observed blue color, as confirmed by colorimetric and spectroscopic analysis and density functional theory (DFT) calculations.

The substitution of Zn<sup>2+</sup> by Ni<sup>2+</sup> at x = 0.01% directionally regulates the electron transfer, likely occurring from [NiO<sub>4</sub>] and tetrahedral [ZnO<sub>4</sub>] and [GeO<sub>4</sub>] neighbor clusters to shared oxygen anions. These dominant features are responsible for the observed blue color, as confirmed by colorimetric and spectroscopic analysis and DFT calculations. Furthermore, adding Ni<sup>2+</sup> enables absorptions in the NIR region, which is particularly valuable for obtaining reflective pigments.

Based on the experimental data and accurate modeling at the DFT level, we conclude that the blue color is primarily linked to electron

redistribution. These findings provided a new idea for the design of novel Ni<sup>2+</sup>-doped ZGO to meet diverse application needs.

## 6 – References

### 6.1 – V-doped AW (1-83)

- [1] Foggi, C. C. *et al.* Synthesis and evaluation of  $\alpha$ -Ag<sub>2</sub>WO<sub>4</sub> as novel antifungal agent. *Chem. Phys. Lett.* **674**, 125–129 (2017).
- [2] Liang, C. *et al.* Boosting molecular oxygen activation ability in self-assembled plasmonic p-n semiconductor photocatalytic heterojunction of WO<sub>3</sub>/Ag@Ag<sub>2</sub>O. *Chem. Eng. J.* **372**, 12–25 (2019).
- [3] Haro Chávez, N. L. *et al.* Promising effects of silver tungstate microcrystals on fibroblast human cells and three dimensional collagen matrix models: A novel non-cytotoxic material to fight oral disease. *Colloids Surfaces B Biointerfaces* **170**, 505–513 (2018).
- [4] Pellissari, C. V. G. *et al.* In Vitro Toxic Effect of Biomaterials Coated with Silver Tungstate or Silver Molybdate Microcrystals. *J. Nanomater.* **2020**, (2020).
- [5] Guo, C. X., Yu, B., Xie, J. N. & He, L. N. Silver tungstate: A single-component bifunctional catalyst for carboxylation of terminal alkynes with CO<sub>2</sub> in ambient conditions. *Green Chem.* **17**, 474–479 (2015).
- [6] Longo, V. M. *et al.* Potentiated Electron Transference in  $\alpha$ -Ag<sub>2</sub>WO<sub>4</sub> Microcrystals with Ag Nanofilaments as Microbial Agent. *J. Phys. Chem. A* **118**, 5769–5778 (2014).
- [7] Nobre, F. X. *et al.* Antimicrobial properties of  $\alpha$ -Ag<sub>2</sub>WO<sub>4</sub> rod-like microcrystals synthesized by sonochemistry and sonochemistry followed by hydrothermal conventional method. *Ultrason. Sonochem.* **58**, 104620 (2019).
- [8] de Foggi, C. C. *et al.* Tuning the Morphological, Optical, and Antimicrobial Properties of  $\alpha$ -Ag<sub>2</sub>WO<sub>4</sub> Microcrystals Using Different Solvents. *Cryst. Growth Des.* **17**, 6239–6246 (2017).
- [9] Santos, C. J. *et al.* Ag<sub>2</sub>WO<sub>4</sub> nanoparticles radiolabeled with technetium-99m: a potential new tool for tumor identification and uptake. *J. Radioanal. Nucl. Chem.* **323**, 51–59 (2020).
- [10] da Silva, L. F. *et al.* Acetone gas sensor based on  $\alpha$ -Ag<sub>2</sub>WO<sub>4</sub> nanorods obtained via a microwave-assisted hydrothermal route. *J. Alloys Compd.* **683**, 186–190 (2016).
- [11] Da Silva, L. F. *et al.* A novel ozone gas sensor based on one-dimensional (1D)  $\alpha$ -Ag<sub>2</sub>WO<sub>4</sub> nanostructures. *Nanoscale* **6**, 4058–4062 (2014).
- [12] Gouveia, A. F. *et al.* Ag<sub>2</sub>WO<sub>4</sub> as a multifunctional material: Fundamentals and progress of an extraordinarily versatile semiconductor. *J. Mater. Res. Technol.* **21**, 4023–4051 (2022).

- [13] Andrade Neto, N. F., Oliveira, P. M., Bomio, M. R. D. & Motta, F. V. Effect of temperature on the morphology and optical properties of Ag<sub>2</sub>WO<sub>4</sub> obtained by the co-precipitation method: Photocatalytic activity. *Ceram. Int.* **45**, 15205–15212 (2019).
- [14] Macedo, N. G. *et al.* Surfactant-Mediated Morphology and Photocatalytic Activity of  $\alpha$ -Ag<sub>2</sub>WO<sub>4</sub> Material. *J. Phys. Chem. C* **122**, 8667–8679 (2018).
- [15] Ribeiro, L. K. *et al.* Tug-of-War Driven by the Structure of Carboxylic Acids: Tuning the Size, Morphology, and Photocatalytic Activity of  $\alpha$ -Ag<sub>2</sub>WO<sub>4</sub>. *Nanomaterials* **12**, (2022).
- [16] Song, Q. W. *et al.* Efficient chemical fixation of CO<sub>2</sub> promoted by a bifunctional Ag<sub>2</sub>WO<sub>4</sub>/Ph<sub>3</sub>P system. *Green Chem.* **16**, 1633–1638 (2014).
- [17] Borys, K. M., Korzyński, M. D. & Ochal, Z. Derivatives of phenyl tribromomethyl sulfone as novel compounds with potential pesticidal activity. *Beilstein J. Org. Chem.* **8**, 259–265 (2012).
- [18] Chen, X. *et al.* Sulfonyl Group-Containing Compounds in the Design of Potential Drugs for the Treatment of Diabetes and Its Complications. *Curr. Med. Chem.* **19**, 3578–3604 (2012).
- [19] Choi, J., Martín-Gago, P. & Fu, G. C. Stereoconvergent arylations and alkenylations of unactivated alkyl electrophiles: Catalytic enantioselective synthesis of secondary sulfonamides and sulfones. *J. Am. Chem. Soc.* **136**, 12161–12165 (2014).
- [20] Desrosiers, J. N. & Charette, A. B. Catalytic enantioselective reduction of  $\beta,\beta$ -disubstituted vinyl phenyl sulfones by using bisphosphine monoxide ligands. *Angew. Chemie - Int. Ed.* **46**, 5955–5957 (2007).
- [21] Kachaeva, M. V. *et al.* Design, synthesis and evaluation of novel sulfonamides as potential anticancer agents. *Comput. Biol. Chem.* **74**, 294–303 (2018).
- [22] Llamas, T., Arrayás, R. G. & Carretero, J. C. Catalytic asymmetric conjugate reduction of  $\beta,\beta$ -disubstituted  $\alpha,\beta$ -unsaturated sulfones. *Angew. Chemie - Int. Ed.* **46**, 3329–3332 (2007).
- [23] Mauleón, P. & Carretero, J. C. Rhodium-catalyzed enantioselective conjugate addition of organoboronic acids to  $\alpha,\beta$ -unsaturated sulfones. *Org. Lett.* **6**, 3195–3198 (2004).
- [24] Sugimoto, H., Nakamura, S., Watanabe, Y. & Toru, T. Enantioselective hydrogen atom transfer to  $\alpha$ -sulfonyl radicals controlled by selective coordination of a chiral Lewis acid to an enantiotopic sulfonyl oxygen. *Tetrahedron Asymmetry* **14**, 3043–3055 (2003).
- [25] Zhu, Y. I. & Stiller, M. J. Dapsone and sulfones in dermatology: Overview and update. *J. Am. Acad. Dermatol.* **45**, 420–434 (2001).



- [26] Radko, M. *et al.* Catalytic oxidation of organic sulfides by H<sub>2</sub>O<sub>2</sub> in the presence of titanosilicate zeolites. *Microporous Mesoporous Mater.* **302**, (2020).
- [27] Muñoz, M., Mendoza-Herrera, L. J., Romanelli, G. P., Gazzoli, D. & Cabello, C. I. Catalytic behavior of the WO<sub>x</sub>-ZrO<sub>2</sub> system in the clean selective oxidation of diphenyl sulfide (DPS). *Catal. Today* **372**, 146–153 (2021).
- [28] Sheldon, R. A. Metrics of Green Chemistry and Sustainability: Past, Present, and Future. *ACS Sustain. Chem. Eng.* **6**, 32–48 (2018).
- [29] Assis, M. *et al.* Towards an efficient selective oxidation of sulfides to sulfones by NiWO<sub>4</sub> and  $\alpha$ -Ag<sub>2</sub>WO<sub>4</sub>. *Appl. Catal. A Gen.* 119038 (2023) doi:<https://doi.org/10.1016/j.apcata.2023.119038>.
- [30] Libero, L. O. *et al.* Introducing Structural Diversity: Fe<sub>2</sub>(MoO<sub>4</sub>)<sub>3</sub> Immobilized in Chitosan Films as an Efficient Catalyst for the Selective Oxidation of Sulfides to Sulfones. *ChemCatChem* **n/a**, e202300421 (2023).
- [31] Radko, M. *et al.* Titanium dioxide doped with vanadium as effective catalyst for selective oxidation of diphenyl sulfide to diphenyl sulfonate. *J. Therm. Anal. Calorim.* **132**, 1471–1480 (2018).
- [32] Pereira, W. D. S. *et al.* Effects of chemical substitution on the structural and optical properties of  $\alpha$ -Ag<sub>2</sub>-2xNi<sub>x</sub>WO<sub>4</sub> ( $0 \leq x \leq 0.08$ ) solid solutions. *Phys. Chem. Chem. Phys.* **18**, 21966–21975 (2016).
- [33] Pereira, P. F. S. *et al.*  $\alpha$ -Ag<sub>2-2x</sub>Zn<sub>x</sub>WO<sub>4</sub> ( $0 \leq x \leq 0.25$ ) Solid Solutions: Structure, Morphology, and Optical Properties. *Inorg. Chem.* **56**, 7360–7372 (2017).
- [34] R.S. of Chemistry, Uses and properties - Vanadium, (n.d.). <https://www.rsc.org/periodic-table/element/23/vanadium> (accessed August 10, 2024).
- [35] T.A. Abogabal, F.M. Radwan, N.Y. Mostafa, S.A. Shata, N. Abdel Aal, Effect of vanadium doping on magnetic properties and photocatalytic activity of magnesium ferrite: Role of surface charge and dyes adsorption, *J. Magn. Magn. Mater.* **602** (2024) 172198. <https://doi.org/10.1016/j.jmmm.2024.172198>.
- [36] E. Weidner, B. Kurc, B. Samojeden, M. Pigłowska, A. Kolodziejczak-Radzimska, T. Jesionowski, F. Ciesielczyk, Exploiting the multifunctionality of a designed vanadium-doped ZnO hybrid for selective catalytic reduction of NO<sub>x</sub> and electrochemical applications, *J. Environ. Chem. Eng.* **10** (2022). <https://doi.org/10.1016/j.jece.2022.108780>.
- [37] I. Stanciu, L. Predoana, C. Anastasescu, D.C. Culita, S. Preda, J. Pandele Cusu, C. Munteanu, A. Rusu, I. Balint, M. Zaharescu, Structure and properties of vanadium doped TiO<sub>2</sub> powders prepared

- by sol-gel method, *Rev. Roum. Chim.* **59** (2014) 919–929.
- [38] Tello, A. C. M. *et al.* Microwave-Driven Hexagonal-to-Monoclinic Transition in BiPO<sub>4</sub>: An In-Depth Experimental Investigation and First-Principles Study. *Inorg. Chem.* **59**, 7453–7468 (2020).
- [39] Assis, M. *et al.* Surface-dependent photocatalytic and biological activities of Ag<sub>2</sub>CrO<sub>4</sub>: Integration of experiment and simulation. *Appl. Surf. Sci.* **545**, 148964 (2021).
- [40] Yin, C., Ye, T., Yu, Y., Li, W. & Ren, Q. Detection of hydroxyl radicals in sonoelectrochemical system. *Microchem. J.* **144**, 369–376 (2019).
- [41] Harbour, J. R. & Issler, S. L. Involvement of the azide radical in the quenching of singlet oxygen by azide anion in water. *J. Am. Chem. Soc.* **104**, 903–905 (1982).
- [42] Penha, M. D. *et al.* Structure, optical properties, and photocatalytic activity of  $\alpha$ -Ag<sub>2</sub>W<sub>0.75</sub>Mo<sub>0.25</sub>O<sub>4</sub>. *Mater. Res. Bull.* **132**, 111011 (2020).
- [43] Dovesi, R. *et al.* CRYSTAL14: A program for the ab initio investigation of crystalline solids. *Int. J. Quantum Chem.* **114**, 1287–1317 (2014).
- [44] Dovesi, R. *et al.* CRYSTAL14 User's Manual. *Theoretical Chemistry Group, University of Turin: Italy* 211 (2014).
- [45] Becke, A. D. Density-functional thermochemistry. III. The role of exact exchange. *J. Chem. Phys.* **98**, 5648–5652 (1993).
- [46] Lee, C.; Yang, W.; Parr, R. G. Development of the Colic-Salvetti correlation-energy formula into a functional of the electron density. *Phys. Rev. B: Condens. Matter Mater. Phys.* vol. 37 785–789 (1988).
- [47] Crystal.
- [48] Hay, P. J. & Wadt, W. R. Ab initio effective core potentials for molecular calculations. Potentials for the transition metal atoms Sc to Hg. *J. Chem. Phys.* **82**, 270–283 (1985).
- [49] Assis, M. *et al.* Ag Nanoparticles/ $\alpha$ -Ag<sub>2</sub>WO<sub>4</sub> Composite Formed by Electron Beam and Femtosecond Irradiation as Potent Antifungal and Antitumor Agents. *Sci. Rep.* **9**, 9927 (2019).
- [50] Cavalcante, L. S. *et al.* Cluster coordination and photoluminescence properties of  $\alpha$ -Ag<sub>2</sub>WO<sub>4</sub> microcrystals. *Inorg. Chem.* **51**, 10675–10687 (2012).
- [51] Turkovič, A., Fox, D. L., Scott, J. F., Geller, S. & Ruse, G. F. High temperature Raman spectroscopy of silver tetratungstate, Ag<sub>8</sub>W<sub>4</sub>O<sub>16</sub>. *Mater. Res. Bull.* **12**, 189–195 (1977).
- [52] Gupta, S. K., Sudarshan, K., Ghosh, P. S., Mukherjee, S. & Kadam, R. M. Doping-Induced Room Temperature Stabilization of Metastable  $\beta$ -Ag<sub>2</sub>WO<sub>4</sub> and Origin of Visible Emission in  $\alpha$ - And  $\beta$ -

- Ag<sub>2</sub>WO<sub>4</sub>: Low Temperature Photoluminescence Studies. *J. Phys. Chem. C* **120**, 7265–7276 (2016).
- [53] Lin, Z. *et al.* Electronic Reconstruction of  $\alpha$ -Ag<sub>2</sub>WO<sub>4</sub> Nanorods for Visible-Light Photocatalysis. *ACS Nano* **9**, 7256–7265 (2015).
- [54] Pinatti, I. M., Ireland, T. G., Fern, G. R., Rosa, I. L. V & Silver, J. Low temperature micro Raman and laser induced upconversion and downconversion spectra of europium doped silver tungstate Ag<sub>2</sub>–3xEu<sub>x</sub>WO<sub>4</sub> nanorods. *J. Mater. Sci. Mater. Electron.* **28**, 7029–7035 (2017).
- [55] Pinatti, I. M. *et al.* Structural and photoluminescence properties of Eu<sup>3+</sup> doped  $\alpha$ -Ag<sub>2</sub>WO<sub>4</sub> synthesized by the green coprecipitation methodology. *Dalt. Trans.* **44**, 17673–17685 (2015).
- [56] Premchand, Y. D. & Suthanthiraraj, S. A. Structural investigation of (CuI)<sub>0.45</sub>–(Ag<sub>2</sub>WO<sub>4</sub>)<sub>0.55</sub> solid electrolyte using X-ray photoelectron and laser Raman spectroscopies. *Electrochem. commun.* **6**, 1266–1269 (2004).
- [57] Muthukumar, P. *et al.* F and rare V<sup>4+</sup> doped cobalt hydroxide hybrid nanostructures: excellent OER activity with ultralow overpotential. *Dalt. Trans.* **52**, 4606–4615 (2023).
- [58] Wood, D. L. & Tauc, J. Weak Absorption Tails in Amorphous Semiconductors. *Phys. Rev. B* **5**, 3144–3151 (1972).
- [59] Kubelka, P. & Munk, F. Ein Beitrag Zur Optik Der Farbanstriche. *Zeitschrift für Tech. Phys.* **12**, 593–601 (1931).
- [60] Roca, R. A. *et al.* Facet-dependent photocatalytic and antibacterial properties of  $\alpha$ -Ag<sub>2</sub>WO<sub>4</sub> crystals: combining experimental data and theoretical insights. *Catal. Sci. Technol.* **5**, 4091–4107 (2015).
- [61] Barnard, A. S. & Zapol, P. A model for the phase stability of arbitrary nanoparticles as a function of size and shape. *J. Chem. Phys.* **121**, 4276–4283 (2004).
- [62] Longo, V. M. *et al.* Hierarchical assembly of CaMoO<sub>4</sub> nano-octahedrons and their photoluminescence properties. *J. Phys. Chem. C* **115**, 5207–5219 (2011).
- [63] Assis, M. *et al.* Unconventional Magnetization Generated from Electron Beam and Femtosecond Irradiation on  $\alpha$ -Ag<sub>2</sub>WO<sub>4</sub>: A Quantum Chemical Investigation. *ACS Omega* **5**, 10052–10067 (2020).
- [64] Barrios Trench, A. *et al.* Connecting structural, optical, and electronic properties and photocatalytic activity of Ag<sub>3</sub>PO<sub>4</sub>:Mo complemented by DFT calculations. *Appl. Catal. B Environ.* **238**, (2018).
- [65] Gouveia, A. F., Gracia, L., Longo, E., San-Miguel, M. A. & Andrés, J. Modulating the properties of multifunctional semiconductors by means of morphology: Theory meets experiments. *Comput. Mater.*

- Sci.* **188**, 110217 (2021).
- [66] De Foggi, C. C. *et al.* Unveiling the role of  $\beta$ -Ag<sub>2</sub>MoO<sub>4</sub> microcrystals to the improvement of antibacterial activity. *Mater. Sci. Eng. C* 110765 (2020)  
doi:<https://doi.org/10.1016/j.msec.2020.110765>.
- [67] Zhuang, G., Chen, Y., Zhuang, Z., Yu, Y. & Yu, J. Oxygen vacancies in metal oxides: recent progress towards advanced catalyst design. *Sci. China Mater.* **63**, 2089–2118 (2020).
- [68] Wolkenstein, T. *Electronic Processes on Semiconductor Surfaces during Chemisorption*. *Nucl. Phys.* vol. 13 (1959).
- [69] Mirabella, D. A. *et al.* Effects of donor density on power-law response in tin dioxide gas sensors. *Sensors Actuators B Chem.* **329**, 129253 (2021).
- [70] Maier, J. & Göpel, W. Investigations of the bulk defect chemistry of polycrystalline Tin(IV) oxide. *J. Solid State Chem.* **72**, 293–302 (1988).
- [71] Castro, M. S., Perissinotti, L. & Aldao, C. M. Cooling rate effects in ZnO varistors. *J. Mater. Sci. Mater. Electron.* **3**, 218–221 (1992).
- [72] Assis, M. *et al.* Disclosing the nature of defects in  $\alpha$ -Ag<sub>2</sub>WO<sub>4</sub>. Submitted manuscript (2022).
- [73] Assis, M. *et al.* Revealing the nature of defects in  $\alpha$ -Ag<sub>2</sub>WO<sub>4</sub> by positron annihilation lifetime spectroscopy: A joint experimental and theoretical study. *Cryst. Growth Des.* **21**, 1093–1102 (2021).
- [74] Jupille, J. & Thornton, G. *Defects at Oxide Surfaces*. *Defects at Oxide Surfaces* vol. 58 (Springer, 2015).
- [75] Nakamura, I. *et al.* Role of oxygen vacancy in the plasma-treated TiO<sub>2</sub> photocatalyst with visible light activity for NO removal. *J. Mol. Catal. A Chem.* **161**, 205–212 (2000).
- [76] Trabelsi, H. *et al.* Raman, EPR and ethanol sensing properties of oxygen-Vacancies SrTiO<sub>3- $\delta$</sub>  compounds. *Appl. Surf. Sci.* **426**, 386–390 (2017).
- [77] Qian, J. *et al.* Positive impedance humidity sensors via single-component materials. *Sci. Rep.* **6**, 25574 (2016).
- [78] Shen, Z. *et al.* Role of oxygen vacancies in the electrical properties of WO<sub>3-x</sub> nano/microrods with identical morphology. *J. Nanomater.* 7802589 (2018) doi:10.1155/2018/7802589.
- [79] Di Valentin, C. & Pacchioni, G. Spectroscopic properties of doped and defective semiconducting oxides from hybrid density functional calculations. *Acc. Chem. Res.* **47**, 3233–3241 (2014).
- [80] Luca, V., Thomson, S. & Howe, R. F. Spectroscopic investigation of vanadium speciation in vanadium-doped nanocrystalline anatase. *J. Chem. Soc. - Faraday Trans.* **93**, 2195–2202 (1997).
- [81] Songara, S. *et al.* Synthesis and studies on photochromic properties of

- vanadium doped TiO<sub>2</sub> nanoparticles. *J. Photochem. Photobiol. A Chem.* **209**, 68–73 (2010).
- [82] Kaczorowska, K., Kolarska, Z., Mitka, K. & Kowalski, P. Oxidation of sulfides to sulfoxides. Part 2: Oxidation by hydrogen peroxide. *Tetrahedron* **61**, 8315–8327 (2005).
- [83] Yu, B., Guo, C. X., Zhong, C. L., Diao, Z. F. & He, L. N. Metal-free chemoselective oxidation of sulfides by in situ generated Koser's reagent in aqueous media. *Tetrahedron Lett.* **55**, 1818–1821 (2014).
- [84] Liang, S., Hofman, K., Friedrich, M., Keller, J. & Manolikakes, G. Recent Progress and Emerging Technologies towards a Sustainable Synthesis of Sulfones. *ChemSusChem* **n/a**,.
- [85] Dulieu, F., Minissale, M. & Bockelée-Morvan, D. Production of O<sub>2</sub> through dismutation of H<sub>2</sub> O<sub>2</sub> during water ice desorption: A key to understanding comet O<sub>2</sub> abundances. *Astron. Astrophys.* **597**, 4–8 (2017).
- [86] Foustoukos, D. I., Houghton, J. L., Seyfried, W. E., Sievert, S. M. & Cody, G. D. Kinetics of H<sub>2</sub>–O<sub>2</sub>–H<sub>2</sub>O redox equilibria and formation of metastable H<sub>2</sub>O<sub>2</sub> under low temperature hydrothermal conditions. *Geochim. Cosmochim. Acta* **75**, 1594–1607 (2011).
- [87] Brame, J., Long, M., Li, Q. & Alvarez, P. Trading oxidation power for efficiency: Differential inhibition of photo-generated hydroxyl radicals versus singlet oxygen. *Water Res.* **60**, 259–266 (2014).

## 6.2 - Ni-doped ZGO (84-145)

- [84] M. Llusar, A. Forés, J.A. Badenes, J. Calbo, M.A. Tena, G. Monrós, Colour analysis of some cobalt-based blue pigments, *J. Eur. Ceram. Soc.* **21** (2001) 1121–1130. [https://doi.org/10.1016/S0955-2219\(00\)00295-8](https://doi.org/10.1016/S0955-2219(00)00295-8).
- [85] K. Zheng, F. Yang, Z. Huang, Y. Zhan, Z. Xiao, W. Li, W. Wang, C. Qin, Preparation of chitosan film-loaded palladium catalyst materials and their application in Suzuki coupling reactions, *J. Mater. Res. Technol.* **20** (2022) 3905–3917. <https://doi.org/10.1016/j.jmrt.2022.08.130>.
- [86] J. Jing, Y. Zhang, J. Sun, X. Zhao, D. Gao, Y. Zhang, A comparative study on different RE-doped (RE=Pr, Nd, Sm) SrCuSi<sub>4</sub>O<sub>10</sub> blue pigments with high near-infrared reflectance, *Dye. Pigment.* **150** (2018) 9–15. <https://doi.org/10.1016/j.dyepig.2017.10.045>.
- [87] A.E. Smith, H. Mizoguchi, K. Delaney, N.A. Spaldin, A.W. Sleight, M.A. Subramanian, Mn<sup>3+</sup> in Trigonal Bipyramidal Coordination: A New Blue Chromophore, *J. Am. Chem. Soc.* **131** (2009) 17084–17086. <https://doi.org/10.1021/ja9080666>.

- [88] T. Wang, J. Liu, W. Jiang, F. Jiang, G. Feng, L. Miao, Q. Zhang, Q. Wu, X. Lao, Fluorine-free synthesis and characterization of vanadium-zircon (V–ZrSiO<sub>4</sub>) turquoise ceramic pigment by a low temperature solid state reaction route, *Ceram. Int.* 48 (2022) 24044–24055. <https://doi.org/10.1016/j.ceramint.2022.05.083>.
- [89] E. Ozel, H. Yurdakul, S. Turan, M. Ardit, G. Cruciani, M. Dondi, Co-doped willemite ceramic pigments: Technological behaviour, crystal structure and optical properties, *J. Eur. Ceram. Soc.* 30 (2010) 3319–3329. <https://doi.org/10.1016/j.jeurceramsoc.2010.08.013>.
- [90] M. Benchikhi, R. Hattaf, A. Moutaabbid, R. El Ouatib, Structural, morphological, and optical properties of Co-substituted Zn<sub>2</sub>SiO<sub>4</sub> nanopowders prepared by a hydrothermal-assisted sol-gel process, *Mater. Chem. Phys.* 276 (2022) 125434. <https://doi.org/10.1016/j.matchemphys.2021.125434>.
- [91] J. Liang, J. Xu, J. Long, Z. Zhang, X. Wang, Self-assembled micro/nano-structured Zn<sub>2</sub>GeO<sub>4</sub> hollow spheres: direct synthesis and enhanced photocatalytic activity, *J. Mater. Chem. A.* 1 (2013) 10622–10625. <https://doi.org/10.1039/C3TA12183F>.
- [92] Y. Li, A. Zhao, C. Chen, C. Zhang, J. Zhang, G. Jia, Controllable synthesis and morphology-dependent photoluminescence properties of well-defined one-dimensional Zn<sub>2</sub>GeO<sub>4</sub>:Mn<sup>2+</sup> nanostructures, *Dye. Pigment.* 150 (2018) 267–274. <https://doi.org/10.1016/j.dyepig.2017.12.021>.
- [93] Lin, K., Ma, B., Su, W. & Liu, W., Improved photocatalytic hydrogen generation on Zn<sub>2</sub>GeO<sub>4</sub> nanorods with high crystallinity, *Appl. Surf. Sci.*, 286 (2013) 61–65. <https://doi.org/10.1016/j.apsusc.2013.09.014>.
- [94] Y. Zhao, S. Feng, H. Jiang, S. Ma, Z. Tao, W. Lu, Y. Fan, Catalyst-free growth of a Zn<sub>2</sub>GeO<sub>4</sub> nanowire network for high-performance transfer-free solar-blind deep UV detection, *Phys. E Low-Dimensional Syst. Nanostructures.* 107 (2019) 1–4. <https://doi.org/10.1016/j.physe.2018.11.015>.
- [95] V.B.R. Boppana, N.D. Hould, R.F. Lobo, Synthesis, characterization and photocatalytic properties of novel zinc germanate nano-materials, *J. Solid State Chem.* 184 (2011) 1054–1062. <https://doi.org/10.1016/j.jssc.2011.02.022>.
- [96] J.P.A. de Jesus, A.C.L. Santos, F.M. Pinto, C.A. Taft, F.A. La Porta, Review: theoretical and experimental investigation of the intrinsic properties of Zn<sub>2</sub>GeO<sub>4</sub> nanocrystals, *J. Mater. Sci.* 56 (2021) 4552–4568. <https://doi.org/10.1007/s10853-020-05549-8>.
- [97] J. Dolado, J. García-Fernández, P. Hidalgo, J. González-Calbet, J. Ramírez-Castellanos, B. Méndez, Intense cold-white emission due to native defects in Zn<sub>2</sub>GeO<sub>4</sub> nanocrystals, *J. Alloys Compd.* 898 (2022)

162993. <https://doi.org/10.1016/j.jallcom.2021.162993>.
- [98] J. Dolado, B. Rodríguez, R. Martínez-Casado, I. Piš, E. Magnano, P. Hidalgo, B. Méndez, Li-doping effects on the native defects and luminescence of  $\text{Zn}_2\text{GeO}_4$  microstructures: Negative thermal quenching, *Acta Mater.* 245 (2023). <https://doi.org/10.1016/j.actamat.2022.118606>.
- [99] S.K. Gupta, K. Sudarshan, B. Modak, R. Gupta, Interstitial Zinc Boosted Light Tunability, Afterglow, and Ultrabright White Emission in Zinc Germanate ( $\text{Zn}_2\text{GeO}_4$ ), *ACS Appl. Electron. Mater.* 5 (2023) 1286–1294. <https://doi.org/10.1021/acsaelm.2c01759>.
- [100] M.T.A. Balhara, S.K. Gupta, M. Abraham, B. Modak, S. Das, C. Nayak, H.V. Annadata, Trap engineering through chemical doping for ultralong X-ray persistent luminescence and anti-thermal quenching in  $\text{Zn}_2\text{GeO}_4$ , *J. Mater. Chem. C.* 12 (2024) 1718–1727. <https://doi.org/10.1039/D3TC03442A>.
- [101] F. Gao, Q. Pang, D. Gao, C. Jia, H. Xin, Y. Pan, Y. Wang, S. Yun,  $\text{Mn}^{2+}$ -Activated Photostimulable Persistent Nanophosphors by  $\text{Pr}^{3+}$  Codoping for Rewritable Information Storage, *ACS Appl. Nano Mater.* 6 (2023) 3054–3064. <https://doi.org/10.1021/acsanm.2c05552>.
- [102] B.B. Srivastava, S.K. Gupta, Y. Li, Y. Mao, Bright persistent green emitting water-dispersible  $\text{Zn}_2\text{GeO}_4:\text{Mn}$  nanorods, *Dalt. Trans.* 49 (2020) 7328–7340. <https://doi.org/10.1039/d0dt00361a>.
- [103] F. Chi, B. Jiang, Z. Zhao, Y. Chen, X. Wei, C. Duan, M. Yin, W. Xu, Multimodal temperature sensing using  $\text{Zn}_2\text{GeO}_4:\text{Mn}^{2+}$  phosphor as highly sensitive luminescent thermometer, *Sensors Actuators, B Chem.* 296 (2019) 1–8. <https://doi.org/10.1016/j.snb.2019.126640>.
- [104] N.M. Cao Hoang Phuong Lan, C.X. Thang, V.H. Pham, P. The Kien, V.T. Ngoc Minh, T.T. Hao Tam, Effects of Cr-doping on the morphology and optical properties in  $\text{Zn}_2\text{GeO}_4$  (ZGO) nanorods prepared by hydrothermal method, *Optik (Stuttg.)* 199 (2019) 163310. <https://doi.org/10.1016/j.ijleo.2019.163310>.
- [105] A.K.V. Raj, P.P. Rao, Intense Blue Chromophores in Cobalt Doped Phenacite-Type Zinc Germanate System through Jahn-Teller Distortion of Co Tetrahedron, *ChemistrySelect.* 6 (2021) 11344–11351. <https://doi.org/10.1002/slct.202102998>.
- [106] N. Gorodylova, V. Kosinová, Ž. Dohnalová, P. Bělina, P. Šulcová, New purple-blue ceramic pigments based on  $\text{CoZr}_4(\text{PO}_4)_6$ , *Dye. Pigment.* 98 (2013) 393–404. <https://doi.org/10.1016/j.dyepig.2013.03.004>.
- [107] S.H. Farjana, N. Huda, M.A.P. Mahmud, Life cycle assessment of cobalt extraction process, *J. Sustain. Min.* 18 (2019) 150–161. <https://doi.org/10.1016/j.jsm.2019.03.002>.
- [108] R. Ianoş, I. Rus, R. Lazău, C. Păcurariu, Near-infrared reflective Ni,

- La-doped hibonite pigments for cool blue coatings, *Ceram. Int.* 48 (2022) 34428–34436.  
<https://doi.org/10.1016/j.ceramint.2022.08.021>.
- [109] J. Chen, G. Feng, F. Jiang, L. Yin, Q. Zhao, S. Lan, X.J. Zhang, J. Liu, Q. Hu, W. Jiang, Synthesis and coloring properties of novel Ni-doped tialite pigments, *Ceram. Int.* 47 (2021) 33242–33251.  
<https://doi.org/10.1016/j.ceramint.2021.08.225>.
- [110] Y. Wang, P. Jiang, M.A. Subramanian, W. Cao, Synthesis, properties and applications of novel inorganic yellow pigments based on Ni-doped  $\text{Al}_2\text{TiO}_5$ , *Solid State Sci.* 135 (2023) 107088.  
<https://doi.org/10.1016/j.solidstatesciences.2022.107088>.
- [111] G. Costa, M.J. Ribeiro, W. Hajjaji, M.P. Seabra, J.A. Labrincha, M. Dondi, G. Cruciani, Ni-doped hibonite ( $\text{CaAl}_{12}\text{O}_{19}$ ): A new turquoise blue ceramic pigment, *J. Eur. Ceram. Soc.* 29 (2009) 2671–2678.  
<https://doi.org/10.1016/j.jeurceramsoc.2009.04.001>.
- [112] M. Khairy, N. Magdy, Z.A. Omran, Effect of Ni content, temperature on the electrical and colorimetric properties of nano  $\text{Ni}_x\text{Zn}_{(1-x)}\text{O}$  blue pigments, *Dig. J. Nanomater. Biostructures.* 17 (2022) 1111–1124.  
<https://doi.org/10.15251/DJNB.2022.173.1111>.
- [113] R. Dovesi, R. Orlando, A. Erba, C.M. Zicovich-Wilson, B. Civalleri, S. Casassa, L. Maschio, M. Ferrabone, M. De La Pierre, P. D'Arco, Y. Noël, M. Causà, M. Rérat, B. Kirtman, CRYSTAL14: A program for the ab initio investigation of crystalline solids, *Int. J. Quantum Chem.* 114 (2014) 1287–1317. <https://doi.org/10.1002/qua.24658>.
- [114] R. Dovesi, V.R. Saunders, C. Roetti, R. Orlando, C.M. Zicovich-Wilson, F. Pascale, B. Civalleri, K. Doll, N.M. Harrison, I.J. Bush, P. D'Arco, M. Llunel, M. Causà, Y. Noël, L. Maschio, A. Erba, M. Rérat, S. Casassa, CRYSTAL14 User's Manual, Theor. Chem. Group, Univ. Turin Italy. (2014) 211.
- [115] A.D. Becke, Density-functional thermochemistry. III. The role of exact exchange, *J. Chem. Phys.* 98 (1993) 5648–5652.  
<https://doi.org/10.1063/1.464913>.
- [116] R.G. Lee, C.; Yang, W.; Parr, Development of the Colic-Salvetti correlation-energy formula into a functional of the electron density, *Phys. Rev. B Condens. Matter Mater. Phys.* 37 (1988) 785–78
- [117] Crystal. [http://www.crystal.unito.it/Basis\\_Sets/Ptable.html](http://www.crystal.unito.it/Basis_Sets/Ptable.html).
- [118] J. Dolado, R. Martínez-Casado, P. Hidalgo, R. Gutierrez, A. Dianat, G. Cuniberti, F. Domínguez-Adame, E. Díaz, B. Méndez, Understanding the UV luminescence of zinc germanate: The role of native defects, *Acta Mater.* 196 (2020) 626–634.  
<https://doi.org/10.1016/j.actamat.2020.07.009>.
- [119] Z.Y. Xie, H.L. Lu, Y. Zhang, Q.Q. Sun, P. Zhou, S.J. Ding, D.W. Zhang, The electronic structures and optical properties of  $\text{Zn}_2\text{GeO}_4$



- with native defects, *J. Alloys Compd.* 619 (2015) 368–371.  
<https://doi.org/10.1016/j.jallcom.2014.09.003>.
- [120] J. Huang, K. Ding, Y. Hou, X. Wang, X. Fu, Synthesis and photocatalytic activity of  $\text{Zn}_2\text{GeO}_4$  nanorods for the degradation of organic pollutants in water., *ChemSusChem*. 1 (2008) 1011–1019.  
<https://doi.org/10.1002/cssc.200800166>.
- [121] J. Breternitz, D. Fritsch, A. Franz, S. Schorr, A thorough investigation of the crystal structure of willemite-type  $\text{Zn}_2\text{GeO}_4$ , *Zeitschrift Fur Anorg. Und Allg. Chemie.* 647 (2021) 2195–2200.  
<https://doi.org/10.1002/zaac.202100231>.
- [122] L. Liu, X. Zhao, H. Sun, C. Jia, W. Fan, Theoretical study of  $\text{H}_2\text{O}$  adsorption on  $\text{Zn}_2\text{GeO}_4$  surfaces: Effects of surface state and structure-activity relationships, *ACS Appl. Mater. Interfaces.* 5 (2013) 6893–6901. <https://doi.org/10.1021/am4015692>.
- [123] Y. Zhao, S. Yang, J. Zhu, G. Ji, F. Peng, The study of oxygen ion motion in  $\text{Zn}_2\text{GeO}_4$  by Raman spectroscopy, *Solid State Ionics.* 274 (2015) 12–16. <https://doi.org/10.1016/j.ssi.2015.02.015>.
- [124] D.K. Bharti, S. Badatya, P. Tanwar, J. Tawale, A.K. Srivastava, M.K. Gupta, Observation of anomalous phase transition and band gap shrinkage in zinc germanate nanorods, *Mater. Sci. Eng. B.* 259 (2020) 114602. <https://doi.org/10.1016/j.mseb.2020.114602>.
- [125] P. Hidalgo, A. López, B. Méndez, J. Piqueras, Synthesis and optical properties of  $\text{Zn}_2\text{GeO}_4$  microrods, *Acta Mater.* 104 (2016) 84–90.  
<https://doi.org/10.1016/j.actamat.2015.11.023>.
- [126] J.I. Viegas, R.L. Moreira, A. Dias, Optical-vibration and intrinsic dielectric properties of low-k high-Q  $\text{Zn}_2\text{GeO}_4$  ceramics, *J. Phys. Chem. Solids.* 148 (2021).  
<https://doi.org/10.1016/j.jpcs.2020.109693>.
- [127] J. Liu, G. Zhang, Template-free synthesis and high photocatalytic activity of hierarchical  $\text{Zn}_2\text{GeO}_4$  microspheres, *CrystEngComm.* 15 (2013) 382–389. <https://doi.org/10.1039/c2ce26316e>.
- [128] O. Yamaguchi, J. Hidaka, K. Hirota, Formation and characterization of alkoxy-derived  $\text{Zn}_2\text{GeO}_4$ , *J. Mater. Sci. Lett.* 10 (1991) 1471–1474. <https://doi.org/10.1007/BF00724409>.
- [129] S. Cui, Y. Jiao, J. Liu, Y. Pu, J.X. Wang, D. Wang, High-gravity-driven process intensified approach toward  $\text{Mn}^{2+}$  doped  $\text{Zn}_2\text{GeO}_4$  nanophosphors for deep-ultraviolet detecting, *Optik (Stuttg).* 235 (2021) 166644. <https://doi.org/10.1016/j.ijleo.2021.166644>.
- [130] T. Han, C. Li, W. Zhao, Y. She, J. Jiao, F. Liang, Z. Hu, Y. Wu, Investigations on the Synthesis, Crystal Structure, Linear- and Nonlinear-Optical Properties of the Zinc Germanate  $\text{Rb}_2\text{ZnGe}_2\text{O}_6$ , *Inorg. Chem.* 61 (2022) 706–712.  
<https://doi.org/10.1021/acs.inorgchem.1c03465>.

- [131] S. Wu, Q. Ma, Synthesis, characterization and microwave dielectric properties of  $\text{Zn}_2\text{GeO}_4$  ceramics, *J. Alloys Compd.* 567 (2013) 40–46. <https://doi.org/10.1016/j.jallcom.2013.03.052>.
- [132] H. He, Y. Zhang, Q. Pan, G. Wu, G. Dong, J. Qiu, Controllable synthesis of  $\text{Zn}_2\text{GeO}_4:\text{Eu}$  nanocrystals with multi-color emission for white light-emitting diodes, *J. Mater. Chem. C.* 3 (2015) 5419–5429. <https://doi.org/10.1039/c5tc00844a>.
- [133] C. Guo, S. Chen, J. Aslam, J. Li, L.P. Lv, W. Sun, W. Cao, Y. Wang, Microwave-Assisted Metal-Organic Frameworks Derived Synthesis of  $\text{Zn}_2\text{GeO}_4$  Nanowire Bundles for Lithium-Ion Batteries, *Nanomaterials.* 13 (2023). <https://doi.org/10.3390/nano13081432>.
- [134] F. Zou, X. Hu, L. Qie, Y. Jiang, X. Xiong, Y. Qiao, Y. Huang, Facile synthesis of sandwiched  $\text{Zn}_2\text{GeO}_4$ -graphene oxide nanocomposite as a stable and high-capacity anode for lithium-ion batteries, *Nanoscale.* 6 (2014) 924–930. <https://doi.org/10.1039/c3nr04917e>.
- [135] A. Ohta, H. Nakagawa, H. Murakami, S. Higashi, S. Miyazaki, Photoemission study of ultrathin  $\text{GeO}_2/\text{Ge}$  heterostructures formed by UV- $\text{O}_3$  oxidation, *E-Journal Surf. Sci. Nanotechnol.* 4 (2006) 174–179. <https://doi.org/10.1380/ejsnt.2006.174>.
- [136] Z. Ma, X. Liu, X. Wang, Z. Luo, W. Li, Y. Nie, L. Pei, Q. Mao, X. Wen, J. Zhong, Manipulating the d-band center enhances photoreduction of  $\text{CO}_2$  to  $\text{CO}$  in  $\text{Zn}_2\text{GeO}_4$  nanorods, *Chem. Eng. J.* 468 (2023) 143569. <https://doi.org/10.1016/j.cej.2023.143569>.
- [137] B. Kalita, S. Iraqui, X. Borgohain, M.H. Rashid, Ultrasonic irradiation-assisted  $\text{MnFe}_2\text{O}_4$  nanoparticles catalyzed solvent-free selective oxidation of benzyl alcohol to benzaldehyde at room temperature, *RSC Adv.* 13 (2023) 30855–30868. <https://doi.org/10.1039/d3ra03797e>.
- [138] X. Chen, X. Sha, Y. Zhang, D. Gao, L. Wang, Y. Zhang, T. Liu, X. Zhang, J. Zhang, Y. Cao, Y. Wang, X. Li, S. Xu, H. Yu, B. Chen, Multicolor-emitting  $\text{Er}^{3+}$  and  $\text{Er}^{3+}/\text{Yb}^{3+}$  doped  $\text{Zn}_2\text{GeO}_4$  phosphors combining static and dynamic identifications for advanced anti-counterfeiting application, *Spectrochim. Acta - Part A Mol. Biomol. Spectrosc.* 309 (2024) 123830. <https://doi.org/10.1016/j.saa.2023.123830>.
- [139] P. Kubelka, F. Munk, Ein Beitrag Zur Optik Der Farbanstriche, *Zeitschrift Für Tech. Phys.* 12 (1931) 593–601.
- [140] V.Y. Suzuki, N.H. de Paula, R. Gonçalves, M.S. Li, E.C. Pereira, E. Longo, F.A. La Porta, Exploring effects of microwave-assisted thermal annealing on optical properties of  $\text{Zn}_2\text{GeO}_4$  nanostructured films, *Mater. Sci. Eng. B.* 246 (2019) 7–12. <https://doi.org/10.1016/j.mseb.2019.05.023>.
- [141] J. Sato, H. Kobayashi, K. Ikarashi, N. Saito, H. Nishiyama, Y. Inoue,

- Photocatalytic Activity for Water Decomposition of RuO<sub>2</sub>-Dispersed Zn<sub>2</sub>GeO<sub>4</sub> with d10 Configuration, *J. Phys. Chem. B.* 108 (2004) 4369–4375. <https://doi.org/10.1021/jp0373189>.
- [142] M. Gaudon, L.C. Robertson, E. Lataste, M. Duttine, M. Ménétrier, A. Demourgues, Cobalt and nickel aluminate spinels: Blue and cyan pigments, *Ceram. Int.* 40 (2014) 5201–5207. <https://doi.org/10.1016/j.ceramint.2013.10.081>.
- [143] S. Zhang, Z. Pan, Y. Wang, Synthesis and characterization of (Ni, Sb)-co-doped rutile ceramic pigment via mechanical activation-assisted solid-state reaction, *Particuology.* 41 (2018) 20–29. <https://doi.org/10.1016/j.partic.2017.12.016>.
- [144] C. Arc, E. Lamps, *Encyclopedia of Color Science and Technology*, 2016. <https://doi.org/10.1007/978-1-4419-8071-7>.
- [145] I.S. Ahmed, H.A. Dessouki, A.A. Ali, Synthesis and characterization of Ni<sub>x</sub>Mg<sub>1-x</sub>Al<sub>2</sub>O<sub>4</sub> nano ceramic pigments via a combustion route, *Polyhedron.* 30 (2011) 584–591. <https://doi.org/10.1016/j.poly.2010.11.034>.